Plant biomagnetism and magnetic resonance with atomic magnetometry

DOCTORAL THESIS

A dissertation submitted for the degree
Doctor of Natural Sciences

Fachbereich Physik, Mathematik und Informatik
Johannes Gutenberg-Universität Mainz

Anne Mara Fabricant

Supervisor: Prof. Dr. Dmitry Budker

September 2024

Abstract

This thesis explores the unique intersection of two subjects, magnetic fields and living plants, using the tool of atomic magnetometry. The choice of tool, also known as optical magnetometry or optically pumped magnetometry, is motivated by the relatively weak (sub-picotesla) fields under study. Atomic magnetometers have emerged in recent years as the most sensitive human-made magnetic-field detectors, rivaling even superconducting-quantum-interference-device (SQUID) magnetometers. Because atomic magnetometers are noncryogenic, miniaturizable, and can be engineered for portability, they lend themselves to diverse practical applications and have so far been commercialized for biomedicine and geophysics. However, from existing technical literature it has not necessarily been straightforward to understand exactly how these devices fit into the wider landscape of magnetometry, as well as their various different operating principles. To this end, we begin with a tutorial on the physics of atomic magnetometry and review the state of the field.

Then, two different plant-based lines of research are described. The first experiment focuses on plant biomagnetism, i.e. magnetic fields produced by electrical activity in living plants. We detect the magnetic component of the action potential (AP) from the Venus flytrap, a beloved carnivorous plant, employing heat transfer from the thermal sensor to induce autonomous AP firing. This work opens the door to noninvasive studies of current distributions and long-distance electrical signaling in plants and fungal networks, not fully possible using traditional electrophysiological techniques.

The second experiment involves construction and testing of a zero-to-ultralow-field nuclear-magnetic-resonance (ZULF-NMR) spectrometer with a novel signal-enhancing detection scheme. This setup is applied to monitor water dynamics in intact tree leaves, tracking water content and proton-relaxation behavior as a function of dehydration and tree genus. Other applications of the setup are also briefly presented.

Spins don't lie.

Declaration of authorship

I, **Anne M. Fabricant**, hereby declare that the present thesis, entitled **“Plant biomagnetism and magnetic resonance with atomic magnetometry”**, and the work presented herein are my own. I confirm that:

- This work was conducted wholly or mainly while in candidature for a research degree at the Johannes Gutenberg University of Mainz.
- Where any part of the thesis was previously submitted for a degree at any institution, this is clearly stated.
- Where I have consulted the published work of others, this is always clearly attributed.
- Where I have quoted from the work of others, the source is always given. With the exception of such quotations, this thesis is entirely my own work.
- I have acknowledged all main sources of help.
- Where the thesis is based on work conducted jointly with others, I have made clear exactly what was done by others and what I contributed myself.

Mainz, **6 September 2024** Signature:

Contents

Preface and acknowledgments

When in the course of doctoral events, it becomes necessary to wear many different “hats”, one may find that some hats fit better than others—but the millinery experience is always educational. In my time at the University of Mainz and the Helmholtz Institute Mainz, these hats have transformed me, at various points, into precision spectroscopist, graphic designer, project manager, plant whisperer, instrumentalist, analyst, 3D-printer technician, politician, mentor... and the list goes on. All of these experiences are carried forward into the next scientific direction, which inevitably brings with it a unique set of challenges and opportunities, many of them shared with other travelers along the way.

I would like to thank my doctoral supervisor, Dmitry Budker, for always believing in my abilities and giving me the freedom and independence to explore wide-ranging interests. Dima’s ability to boil down complex topics to their intuitive core has served as an inspiration and example.

Special thanks to Geoffrey Iwata, Irina Novikova, and Piotr Put, without whose kindness, competence, and scientific integrity the work contained in this thesis would not have been possible.

Thank you to the magnetometry team at PTB Berlin as well as the broader atomic-magnetometry/vapor-cell community, who were always so welcoming and supportive of me from the very beginning, and to the plant-biology team at the University of Würzburg for their willingness to engage with strange physicists.

Thank you to the gym buddies for the shared gains, and to my bandmates past and present—in particular Peter Leyser, Shun Sato, and Erik Van Dyke, for keeping me grounded and enabling our musical creativity to take flight. Several individuals deserve near-total credit for my continued sanity, including Christina Schorge, dear friend and confidante, Till Lenz, “perfect” officemate, Florin Teleanu, collaborator extraordinaire, and Eleni Kapnisti, not your typical German teacher. I am sure that this list will only continue to grow. Thanks to my housemate, Davide Warm, for putting up with me for a number of years, and to my parents for frequently inquiring as to the status of this document (even composing a song about it). Finally, I wish to apologize to my garden and the plants therein, who, tragically and ironically, suffered terribly from neglect in the making of this thesis.

The illuminated letter M on the title page is courtesy of the Gutenberg Museum.

List of abbreviations

3D	three-dimensional	MEG	magnetoencephalography
ABS	acrylonitrile butadiene styrene	MEMS	microelectromechanical systems
AC	alternating current	MFI	magnetic-field imaging
AP	action potential	MMG	magnetomyography
BNC	Bayonet Neill–Concelman	MSR	magnetically shielded room
CGS	Centimeter-Gram-Second System of Units	MR	magnetoresistive
CPMG	Carr-Purcell-Meiboom-Gill	MRI	magnetic resonance imaging
CPT	coherent population trapping	NMOR	nonlinear magneto-optical rotation
DI	deionized	NMR	nuclear magnetic resonance
DAQ	data acquisition	NV	nitrogen vacancy
DC	direct current	OPM	optically pumped magnetometer
DFB	distributed feedback	PSD	power spectral density
DFT	discrete Fourier transform	RF	radiofrequency
DMC	dimethyl carbonate	RMS	root mean square
EC	ethylene carbonate	SERF	spin-exchange-relaxation-free
EIT	electromagnetically induced transparency	SI	International System of Units
EPR	electron paramagnetic resonance	SNR	signal-to-noise ratio
FFT	fast Fourier transform	SQUID	superconducting quantum-interference device
FID	free induction decay	SWaP	size, weight, and power
FT	Fourier transform	ULF	ultralow field
fMCG	fetal magnetocardiography	TD	time domain
FWHM	full width at half maximum	TTL	transistor-transistor logic
HWHM	half width at half maximum	VCSEL	vertical-cavity surface-emitting laser
$LiPF_6$	lithium hexafluorophosphate	ZULF	zero-to-ultralow field
MCG	magnetocardiography	ZFM	zero-field magnetometer

List of figures

List of tables

Previously published manuscripts

During the period of enrollment as a doctoral student at the University of Mainz, the following co-authored manuscripts, listed chronologically, were published. Publications 5–7 form the body of this thesis.

1. D. Antypas, A. Fabricant, L. Bougas, K. Tsigutkin & D. Budker, "Towards improved measurements of parity violation in atomic ytterbium", *Hyperfine Interact.* **238**, 1–11 (2017), DOI:10.1007/s10751-017-1396-8.
2. Dionysis Antypas, Anne Fabricant & Dmitry Budker, "Lineshape-asymmetry elimination in weak atomic transitions driven by an intense standing wave field", *Opt. Lett.* **43** (10), 2241–2243 (2018), DOI:10.1364/OL.43.002241.
3. D. Antypas, A. Fabricant, J. E. Stalnaker, K. Tsigutkin, V. V. Flambaum & D. Budker, "Isotopic variation of parity violation in atomic ytterbium", *Nat. Phys.* **15** 120–123 (2019), DOI:10.1038/s41567-018-0312-8.
4. D. Antypas, A. M. Fabricant, J. E. Stalnaker, K. Tsigutkin, V. V. Flambaum & D. Budker, "Isotopic variation of parity violation in atomic ytterbium: Description of the measurement method and analysis of systematic effects", *Phys. Rev. A* **100** 012503 (2019), DOI:10.1103/PhysRevA.100.012503.
5. Anne Fabricant, Geoffrey Z. Iwata, Sönke Scherzer, Lykourgos Bougas, Katharina Rolfs, Anna Jodko-Władińska, Jens Voigt, Rainer Hedrich & Dmitry Budker, "Action potentials induce biomagnetic fields in carnivorous Venus flytrap plants", *Sci. Rep.* **11**, 1438 (2021), DOI:10.1038/s41598-021-81114-w.
6. Anne Fabricant, Irina Novikova & Georg Bison, "How to build a magnetometer with thermal atomic vapor: A tutorial", *New J. of Phys.* **25**, 025001, Focus on Hot Atomic Vapors (2023), DOI:10.1088/1367-2630/acb840.
7. Anne M. Fabricant, Piotr Put & Danila A. Barskiy, "Proton relaxometry of tree leaves at hypogeomagnetic fields", *Front. Plant Sci.* **15**, 1352282 (2024), DOI:10.3389/fpls.2024.1352282.
8. Anne M. Fabricant, Román Picazo-Frutos, Florin Teleanu, Gregory J. Rees, Robert A. House, Peter G. Bruce, John Blanchard, James Eills, Kirill Sheberstov, Dmitry Budker, Danila A. Barskiy, Alexej Jerschow, "Ultralow-field nuclear magnetic resonance for direct nondestructive observation of electrolyte composition in batteries", *ChemRxiv* preprint (2024), DOI:10.26434/chemrxiv-2024-32xj9.

Chapter 1

Introduction

In this thesis, magnetic-sensing techniques find new application in the investigation of vital processes in plants. Experimental work encompasses noninvasive magnetic detection of biolectrical signaling *in vivo*, as well as the study of water dynamics in *ex vivo* samples via magnetic resonance—both enabled by atomic-magnetometer technology. This diverse toolbox at the intersection of physics, biology, and chemistry has relevance for research in ecology, agriculture, and even space exploration. Guided by the map in Fig. 1.1, we explore the multidisciplinary terrain through the lens of atomic physics. Thus, the main characters are electrons, nuclei, and electromagnetic fields.

As any successful discussion begins with a definition of terms, let us carefully define the

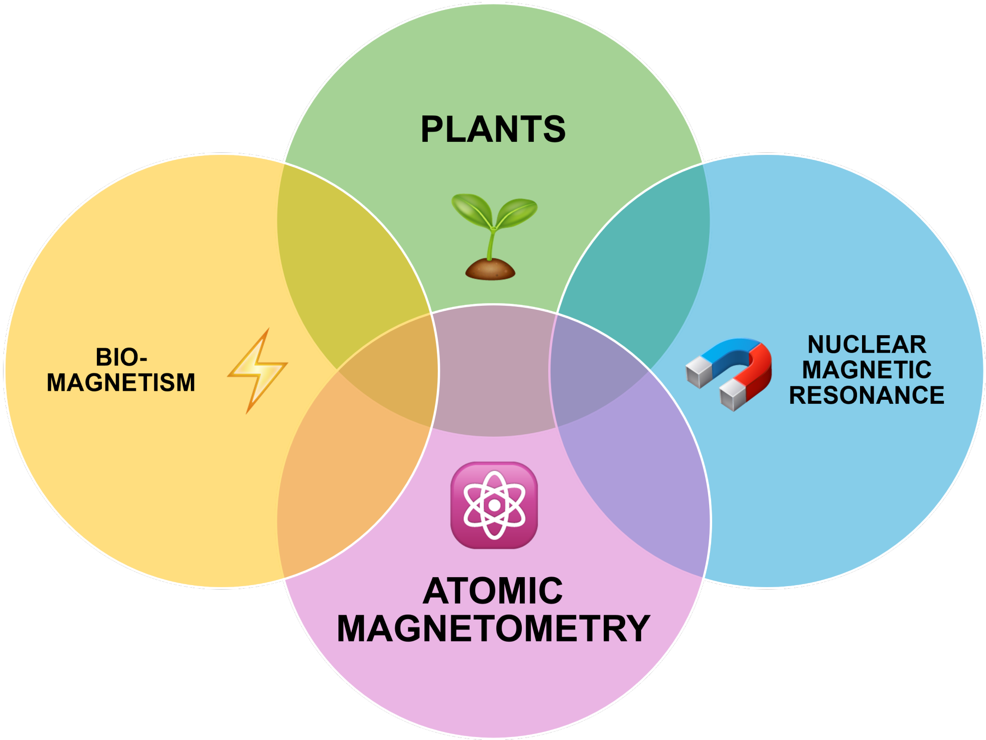

Figure 1.1: Visualization of the topics covered in this thesis and their interrelationships, helpfully illustrated with WhatsApp emojis (Emojipedia).

categories which appear in Fig. 1.1.

A **plant** is a eukaryotic organism, which means that it is comprised of cells with a nucleus and other membrane-bound organelles. What distinguishes plants from animals and fungi, their eukaryote compatriots, is the ability to photosynthesize. Using water, carbon dioxide, and a catalyst called chlorophyll contained inside chloroplasts, plants feed themselves by converting photon energy into chemical energy, releasing oxygen in the process. Of course, as is often the case, particularly in biology, reality does not fall cleanly into categories. There are photosynthesizing non-plant lifeforms, including cyanobacteria (prokaryotes) and algae (protists, yet another type of eukaryote)—which contribute alongside plants to the presence of oxygen in the atmosphere and hence our ability to breathe. Furthermore, some plants have lost their chlorophyll entirely, existing in symbiotic relationships with fungi or other plants. Ultimately, we arrive at a structural definition of a plant as a eukaryote which has roots, stem(s), and leaves. What we can say unequivocally is that plants form the primary food source for humans, and that a significant portion of our medicines are derived from plants.

Biomagnetism refers to the production of magnetic fields from living organisms, including plants. Although this concept may initially conjure up vague notions of 1970s parapsychology, we are really only restating the Ampère-Maxwell law, which tells us that currents and changing electric fields give rise to magnetic fields. Essentially all cellular lifeforms are electrically active due to the flow of ions across the cell membrane, often in response to changing environmental conditions. In multicellular organisms, such electrical signals may also propagate between cells in concerted "waves", triggering additional systemic processes—as we shall see in Ch. 3. For primarily historical reasons, plant electrophysiology is much better understood at the local cellular level than at the systemic level. Conventional wisdom used to hold that the absence of an animal nervous system meant the absence of systemic electric activity, a perception we now know to be false.

The salient difference between **electrophysiology** and **magnetophysiology** is the following. In the former, a circuit is formed with the measurement device in electrical contact with the system under study, and the voltage difference between live and ground electrodes is recorded as a function of time. In the latter, the measurement device is electrically isolated from the system under study, and recorded voltages are proportional to the magnetic field at the location of a magnetically sensitive volume. Both approaches have their unique advantages and can be considered complementary techniques. In general, electrophysiology instruments are technically simpler to implement and produce data which is more straighforward to interpret; they lend themselves to intracellular measurements of membrane potentials in *in vitro* and *ex vivo* samples, as well as surface measurements *in vivo*. Magnetophysiology instruments are less perturbing to the bioelectrical network and less affected by background material distorting signals from the pathway of interest; they are particularly well-suited to noninvasive *in vivo* measurements and source localization. Due to the intrinsic complexity of reconstructing source currents from magnetic-field data, sophisticated analysis techniques may be required. To sum up, one should speak more broadly of **bioelectromagnetism**, which is accessible via measurement of currents, magnetic fields, electric fields, or some combination thereof (we do not discuss electric-field sensors in this thesis). Since electro- and magnetophysiological recordings can give access to different physical information, an important task is to develop robust biomagnetic-sensing protocols. As explained in Chs. 2–3, while such work is well underway in the biomedical community, non-animal subjects are severely understudied.

Biomagnetism is not to be confused with the phenomenon of **magnetobiology**—the effect of the external magnetic-field environment on biological systems and processes—itself a fascinating topic which could fill an entire separate thesis.

However, we do make use of external magnetic fields in this work, in the context of **nuclear magnetic resonance** (NMR). Rather than arising from "natural" electrical activity within the sample, as in biomagnetism, signals in magnetic resonance are due to **spin polarization** prepared using some "artificial" means. For example, nuclear spins can be polarized using magnets or chemical processes, leading to bulk **magnetization** of the sample. This magnetization gives rise to resonances at frequencies defined by coupling to a measurement field as well as internal interactions within the spin system. We return in Ch. 2 to the concepts of spin polarization and magnetization, and the relationship between them.

Along with its sister disciplines, magnetic resonance imaging (MRI) and electron paramagnetic resonance (EPR), NMR is a gargantuan research area spanning nearly a century of history, multiple Noble Prizes, and established commercial devices. We confine ourselves to an untrodden corner of the NMR universe: the intersection of plants, **ultralow** measurement fields, and **relaxometry**. What makes a magnetic field "ultralow" will be more carefully defined in Ch. 4; for now, it suffices to say that such fields are much lower than those encountered in any conventional, commercially available NMR instrument, and can be lower than Earth's magnetic field or even zero. Relaxometry refers to the study of polarized spins relaxing to equilibrium, which gives information not only about the spin system but also about its physical and chemical environment. The laboratory devices employed in zero-to-ultralow-field (ZULF) NMR can be highly versatile, offering broad tuneability of experimental parameters and the ability to accommodate unusual sample geometries—such as plant organs.

Apart from plants, the unifying thread throughout this work is the technology enabling signal detection: **atomic magnetometry**. As the name suggests, atomic magnetometers are magnetic-field sensors whose sensing element consists of an ensemble of atoms, specifically atomic spins. Like in NMR, spins are polarized to create bulk magnetization, but this time the polarization occurs via laser light interacting with electrons. Changes in the external magnetic-field environment affect the atomic spin state and hence the magnetization, and these changes can be read out by interrogating the spin ensemble, also with laser light. Because atomic magnetometers are quantum devices whose fundamental sensitivity is limited only by the uncertainty principle (Ch. 2), they are well-suited to measurement of the subpicotesla signals encountered in biomagnetism and ZULF NMR of plant systems.

The thesis is structured as follows. In Ch. 2, we explore the world of atomic magnetometers, from operating principles to applications. Understanding how these devices work is essential to the design of successful experiments, and provides an excellent basis for understanding the interplay between spins and electromagnetic fields, as well as spin relaxation. Ch. 3 is dedicated to plant biomagnetism, presenting the design and execution of an experiment detecting the magnetic component of the Venus flytrap action potential. To the best of our knowledge, this not only the first demonstration of biomagnetism in this plant system, but also the first confirmation of biomagnetic activity from any plant using atomic magnetometry. In Ch. 4, we shift focus to magnetic resonance, describing a homemade ZULF-NMR spectrometer and applying it to a broad cross-species study of tree leaves. Combining ZULF-NMR with proton-relaxometry methods and a novel sensor geometry, we are able to detect even trace amounts of water protons in *ex vivo* leaves and track their evolution—addressing some surprisingly underexplored aspects of plants' interplay with water, the foundation of all life on Earth. Finally, we conclude in Ch. 5 with a preview of ongoing related follow-up work in both biomagnetism and magnetic resonance.

Chapter 2

How to build a magnetometer with thermal atomic vapor: A tutorial

> You should think about the consequence
> Of your magnetic field being a little too strong
>
> Taylor Swift

New Journal of Physics **25**, 025001, Focus on Hot Atomic Vapors (2023),
DOI:10.1088/1367-2630/acb840 [invited review].

Anne Fabricant[1,2], Irina Novikova[3], and Georg Bison[4]

[1] *Institute of Physics, Johannes Gutenberg University of Mainz, Germany*
[2] *Helmholtz Institute Mainz, GSI Helmholtzzentrum für Schwerionenforschung, Darmstadt, Germany*
[3] *Department of Physics, William & Mary, Williamsburg, Virginia, USA*
[4] *Paul Scherrer Institute, Villigen, Switzerland*

This article is designed as a step-by-step guide to optically pumped magnetometers based on alkali atomic vapor cells. We begin with a general introduction to atomic magneto-optical response, as well as expected magnetometer performance merits and how they are affected by main sources of noise. This is followed by a brief comparison of different magnetometer realizations and an overview of current research, with the aim of helping readers to identify the most suitable magnetometer type for specific applications. Next, we discuss some practical considerations for experimental implementations, using the case of an M_z magnetometer as an example of the design process. Finally, an interactive workbook with real magnetometer data is provided to illustrate magnetometer-performance analysis.

2.1 Why should you build an atomic magnetometer?

The purpose of this review is to introduce students and newcomers to the field of atomic magnetometry in a friendly and didactic manner. We aim to bridge the gap between the various excellent reviews already existing in literature [1–7] and the nitty-gritty of actually setting up and operating an atomic magnetometer in the lab, for either academic or industrial purposes.

The origins of magnetometry—the measurement of magnetic fields—most likely date back to the time of the dinosaurs 150 million years ago, when the first birds evolved. It is known that birds, not only those of the migratory variety, possess an innate magnetic compass for orientation along the geomagnetic field lines, which is activated by exposure to light [8, 9]. In fact, a wide range of animal species are blessed with built-in geomagnetic-field sensors, based on a variety of proposed biochemical mechanisms [10]. Humans, being less gifted by nature, had to develop their own navigational compasses—the earliest type of magnetometer—through arduous scientific work from the 12th century onward, enabling the formation of empires in Europe and Asia. After Gauss developed, in 1832, the first known absolute magnetometer able to directly measure the geomagnetic field, the 20th century saw an explosion of new magnetometer technologies based on both classical- and quantum-physics phenonema. This enabled the sensitive measurement of hypogeomagnetic fields (fields smaller than Earth field) from a diversity of sources (Table 2.1). Chances are that the reader is routinely carrying around a state-of-the-art magnetometer: most modern smartphones are outfitted with a tiny Hall-effect or magnetoresistive (MR) based compass, which can be integrated onto a chip with an accelerometer (to sense linear acceleration) and usually a gyroscope (to sense angular acceleration).

Atomic magnetometers are quantum devices making use of the fact that the electron spin of each atom in a gas reacts to its own magnetic-field environment. During magnetometer operation, atoms are first spin-polarized via optical pumping with laser light along a given direction (Sec. 2.2.1), then allowed to evolve under the influence of an external magnetic field (Sec. 2.2.3). Magnetic-field measurement is enabled by subsequent optical readout of the atomic spin state, which exploits magneto-optical effects—for example, shining linearly polarized off-resonant "probe" light on the atoms and measuring its polarization rotation via the Faraday effect, or measuring the change in absorption of resonant probe light (Sec. 2.2.5). Such atomic magnetometers may be called by different names, including optical(-atomic) magnetometers or optically pumped magnetometers (OPMs), although the magnetic-sensing volume itself consists of atoms.

Before designing and building a sensor in the lab, one should first ask an important question: *Is atomic magnetometry right for my application?* There exists a plethora of magnetometer technologies, many of which are commercially available, with each technology having its own pros and cons. In Table 2.1 and Fig. 2.1, we compare the performance figures of some common commercial magnetometers operating in the magnetic-field range up to Earth field.

Sensor type	**Birth year**	**Example(s)**	**Sensitivity** $\mathrm{pT}/\sqrt{\mathrm{Hz}}$	**Standoff distance** mm	**Smallest linear dimension** mm	**Bandwidth** kHz	**Approx. price range** USD	**Notes**
Fluxgate	1936 [11]	SENSYS, Bartington	6–10	14.5–16.5	23–26	3–4	3–5 000	better lab sensitivity achieved [12, 13]
Proton (incl. Overhauser)	1958 [14]	GEM, Geometrics	15–100	37.5–45	75–90	15-30	100 – 1 000	geophysical applications
Atomic	1962 [15]	QuSpin, Twinleaf	0.01–0.03 (0.09–0.13)	6.5	12.4	0.10–0.15 (0.5–1.1)	9–10 000	biomedical applications
SQUID	1964 [16]	Quantum Design, Magnicon	0.001	66	840	1	up to 1 000 000	cheaper partial systems available
Hall effect	1967 [17]	Metrolab	1000	2.5	1.2	1	4–10 000	useful for field mapping
Magnetoresistive	1982 [18]	TE Connectivity, Sensitec	3	0	N/A	10	2 000	only bare sensor sold commercially

Table 2.1: Performance comparison of commonly available commercial magnetometers. The choice of examples is intended to be representative and not exhaustive; quoted specs are approximate. Non-commercial laboratory magnetometers may surpass the quoted typical performance figures [19]. See Sec. 2.3 for definitions and discussion of the performance figures. Note that optically pumped magnetometers based on nitrogen-vacancy (NV) centers in diamond [20] are not included in this table, since commercial NV sensors at the time of writing are sold only as scanning-microscopy imaging systems. Atomic magnetometers based on parametric resonance in He-4 are currently undergoing commercialization by the company MAG4Health.

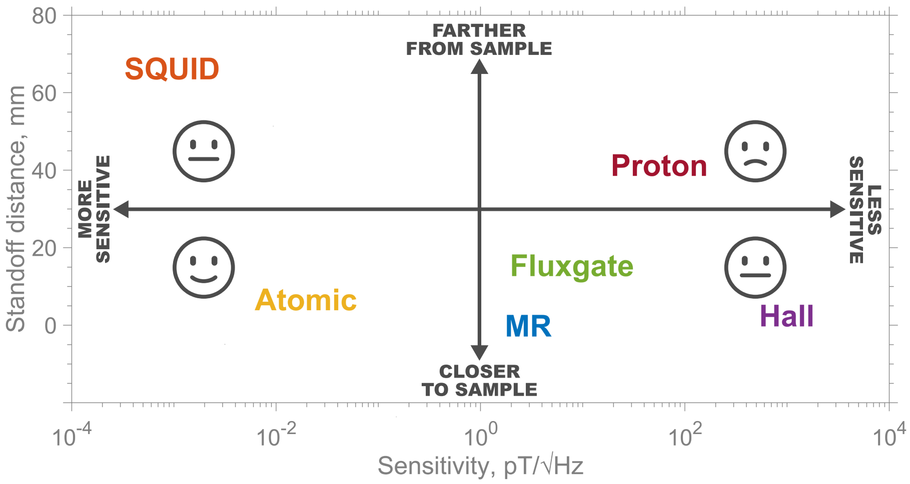

Figure 2.1: A silly pictorial representation of the information in Table 2.1.

Figure 2.1 illustrates that atomic magnetometers can offer the best overall performance for applications requiring both relatively high magnetic-field sensitivity and relatively small stand-off distance from the sample to be measured. Unlike superconducting-quantum-interference-device (SQUID) magnetometers, they are noncryogenic and can operate at ambient temperatures, while also offering greater portability. Although the leading commercial models are designed specifically for biomedical applications such as magnetoencephalography (MEG) [21] and fetal magnetocardiography (fMCG) [22], there is great flexibility in the design of laboratory atomic magnetometers. For example, the atomic sensing volume can be miniaturized or otherwise adapted to the particular sample geometry [23, 24].

This review is structured as follows. In Sec. 2.2, we briefly introduce the technique of optical pumping, through which atomic-spin polarization can be created using resonant laser light. Then we present what we consider to be the most important equation of magnetometry, the Bloch equation, which describes the interaction of atomic spins with an external magnetic field—the heart of an atomic magnetometer. To illustrate the process of magnetometer operation, we consider a specific example of an M_z magnetometer. Sec. 2.3 provides an overview of the relevant figures of merit used to characterize magnetometer performance, some of which were already introduced in Table 2.1. Sec. 2.4 compares the different types of atomic magnetometers and guides the reader in selecting an appropriate operating mode for the desired application (e.g., biological/non-biological, applied/fundamental) and performance requirements. From Sec. 2.5, the tutorial becomes more hands-on. Here we describe how to choose proper components for the magnetometer, including a suitable atomic vapor cell for the sensing volume, as well as laser and magnetic-shielding systems. Next, we outline the step-by-step operational principles of the M_z magnetometer and describe how to obtain a free-induction-decay (FID) signal[1]—steps which can be applied by the reader to other types of atomic magnetometers. Sec. 2.6 focuses on how to characterize magnetometer performance according to the figures of merit discussed in Sec. 2.3.

As the title of this review suggests, we will be covering magnetometers based on thermal atomic vapors. In cold-atom magnetometry, laser cooling is employed to trap and control the sensing atoms, and to prevent spin-destructive atomic collisions which worsen magnetometer performance (Sec. 2.3). Although cold atoms offer advantages in terms of spatial resolution and stand-off distance, the experimental requirements are more stringent and require the use of a vacuum system, and the number of atoms which can be trapped is limited. Despite progress in recent years [25, 26], the sensitivity of cold-atom sensors is not yet competitive with thermal sensors utilizing buffer-gas or anti-relaxation-coated atomic vapor cells (Sec. 2.5.1). Therefore, the latter are preferred for most atomic-magnetometry applications (Sec. 2.7).

Furthermore, we focus specifically on alkali-vapor sensing. References are provided for readers interested in learning more about magnetic sensing with nuclear or electron spins

---

[1] Throughout this thesis, we follow the literature convention of using the term FID to describe the characteristic decaying sinusoidal signal resulting from magnetization precession in a transverse field, regardless of whether this is detected using inductive methods.

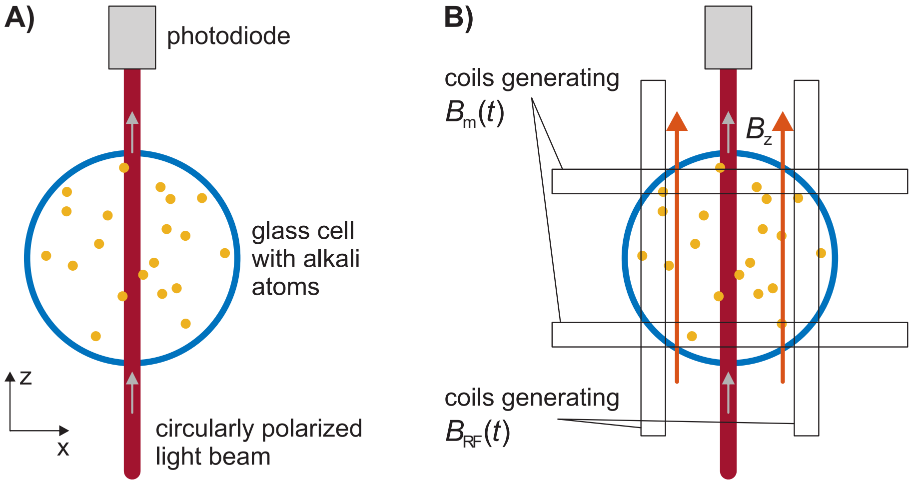

Figure 2.2: **A)** Basic setup of an optically pumped magnetometer. **B)** Setup for the M_z mode of operation.

in helium [27–33], as well as comagnetometers incorporating both noble-gas and alkali vapors in tandem, whereby the nuclear-spin signal is enhanced via spin-exchange optical pumping [34, 35]. Helium magnetometers have traditionally been used for military and aerospace applications, due to their instrinsic robustness and stability, and optically pumped He-4 sensors have recently begun to approach the sensitivity levels of their alkali cousins [28, 36]. Alkali/noble-gas comagnetometers are primarily used in fundamental-physics and gyroscope experiments [34, 37–40].

2.2 The Bloch equation and all that jazz

This section introduces the methodology for theoretical modeling of an atomic magnetometer. As a starting point for the concrete description of such a magnetometer, we choose the experimental setup shown in Figure 2.2A. The core of the magnetometer is the alkali atoms which form a vapor in a glass cell. A laser beam traverses the cell, and the power of the transmitted light is measured by a photodiode. Since atoms interact with both the ambient magnetic field $\vec{B}$ and the laser light, they mediate magneto-optical coupling, such that information about $\vec{B}$ is transferred to the measurable optical signal. At the level of individual atoms, this interaction is characterized by the total atomic angular momentum $\vec{F}$, often referred to as the atomic spin. However, since the laser beam interacts with a large number of atoms at the same time, the ensemble average of $\vec{F}$ is the relevant quantity here. This ensemble average, which we denote as $\vec{M}$, is a macroscopic quantity describing the magnetization state of the atomic medium. Because $\vec{M}$ is derived from atomic spins, it is a macroscopic sum of atomic angular momenta. In the atomic-magnetometry literature, $\vec{M}$ is commonly referred to as the **bulk magnetization** or just **magnetization** of the atomic medium. (We note that in electromagnetism, $\vec{M}$ is defined as bulk magnetization per unit volume.)

Although in this section we primarily rely on the classical description of spin dynamics, we'll first briefly introduce some basics of the quantum description which are relevant for understanding. Our chosen theoretical treatment of the magnetometer can be described as semiclassical, where quantum mechanics is only explicitly invoked in the discussion of optical pumping (Sec. 2.2.1). We find that this approach, based on classical Bloch formalism, is typically the most intuitive and accessible for new experimentalists. However, we wish to emphasize that physically equivalent quantum treatments are also possible. These include the density-matrix formalism—whereby the atomic spin state is encoded in multipole moments of a density matrix which evolves, e.g. in the presence of any electromagnetic fields, according to the quantum Liouville equation [41, 42]—as well as the Floquet description [43] and representations within the framework of quantum optics [44].

In spectroscopic notation, the electronic energy levels of an atom are denoted nL_J. Here n is the principal quantum number and $\vec{L}$ is the orbital angular momentum with quantum number L (S=0, P=1, D=2); $\vec{J} = \vec{L} + \vec{S}$ is the total electronic angular momentum, with $\vec{S}$ being the electron spin ($S = 1/2$). The total angular momentum of the atom is then $\vec{F} = \vec{I} + \vec{J}$, where $\vec{I}$ is the nuclear spin. Let us take as an example the alkali atom Cs-133, the only stable isotope of cesium, with $I = 7/2$: the ground state $6\mathrm{S}_{1/2}$ ($\vec{L} = 0$) splits into two hyperfine states with $F = 3$ and $F = 4$.

Atomic magnetometers make use of this **hyperfine structure** of electronic energy levels, which arises from the magnetic interaction between the nucleus and the electron. The magnetic structure becomes experimentally discernible as a result of the **Zeeman effect**, whereby the otherwise-degenerate hyperfine energy levels split in the presence of a static magnetic field (linearly, in the low-field regime). Summing over all N atomic spins in the ensemble gives us the bulk magnetization:[2]

$$\vec{M} = \sum_{n=1}^{N} \vec{F}_n \,. \tag{2.1}$$

Both quantities, $\vec{F}_n$ and $\vec{M}$, can be measured experimentally from outside the medium [45, 46].

The magnetic quantum number $m_F = F, F-1, \ldots, -F$ measures the atomic-spin component along a given quantization axis. In the absence of optical pumping with laser light (Sec. 2.2.1), each atom's m_F-substates will be thermally populated—corresponding to an unpolarized medium in which the atomic spins are randomly oriented, with an average magnetization given by $\vec{M} = 0$. This is the state which the medium always tends to approach, due to various effects that disturb the atomic spins and thus randomize them. If we are able to put most of the atoms into one of the extreme hyperfine substates $m_F = \pm F$, we have achieved macroscopic spin polarization along the direction of the quantization axis—which manifests classically as bulk magnetization—and we say that there is **orientation** of the atomic-spin ensemble. The spin state of an individual fully polarized atom, in $m_F = \pm F$, is known as a "stretched state".

---

[2] We note that this procedure is not limited to atomic spins and can be extended to other spin systems—such as, as we shall see in Ch. 4, nuclear spins.

Other interesting situations are possible: some magnetometers utilize atomic-spin **alignment**—similar to orientation in the sense that there is a preferred polarization *axis*, but different in that there is no preferred polarization *direction*. Alignment is important for atomic magnetometers based on the principle of nonlinear magneto-optical rotation (NMOR), described in Sec. 2.4. The concept of orientation-to-alignment conversion is treated in a didactic and visual way in [47].

Note that throughout this tutorial and in other atomic-physics literature, the word "polarization" is commonly used to refer to both atomic-spin polarization and light polarization (direction of the light electric field). We hope that the distinction will be clear from the context, such that this overlapping terminology does not cause confusion.

2.2.1 Optical pumping

The first step toward making the medium useful for magnetometry purposes is to create spin polarization, equivalent to magnetizing the medium: orienting a sizeable fraction of the atomic spins in the same direction. In nuclear-magnetic-resonance (NMR) experiments this is typically achieved using a strong (few T) magnet, but alkali atoms can be much more efficiently magnetized using optical pumping. Optical pumping is a field of atomic physics in itself, and a detailed treatment may be found in the canonical reference [48]. For our purposes it suffices to say that using the Hamiltonian for a light-atom dipole interaction, one can derive the following angular-momentum **selection rules** for the driven atomic transitions:

$$\Delta L = \pm 1\,, \tag{2.2}$$

$$\Delta S = 0\,, \tag{2.3}$$

$$\Delta J = \pm 1, 0\,, \tag{2.4}$$

$$\Delta F = \pm 1, 0\,. \tag{2.5}$$

We see that a photon can transfer angular momentum, but it does not interact with the electron spin. The selection rules for the magnetic quantum numbers depend on the polarization of the light. For circularly polarized light, we have

$$\sigma_+ \,\text{photon} \Rightarrow \Delta m_F = +1\,, \tag{2.6}$$

$$\sigma_- \,\text{photon} \Rightarrow \Delta m_F = -1\,. \tag{2.7}$$

Here σ_+ and σ_- denote, respectively, right- and left-circular polarization. When we talk about circular polarization, we should be clear about the convention we are using for handedness. If we visualize the light as a classical wave, σ_+ (σ_-) polarization means that the polarization vector is rotating in the clockwise (counterclockwise) direction *as seen from the source.* An atom may also decay by spontaneous emission with $\Delta m_F = \pm 1, 0$. Examples of the pumping process in alkali atoms are illustrated in 2.8.1 and in [49, 50].

Thus, the first interaction we need in our model is the absorption of circularly polarized photons by the atoms, in order to create orientation in the atomic ground state. Each photon carries a quantum of angular momentum which is transferred to the atoms. As a consequence, $\vec{M}$ builds up in the direction of the laser beam. This build-up can be modeled classically by the following differential equation:

$$\frac{d}{dt}\begin{pmatrix} M_x(t) \\ M_y(t) \\ M_z(t) \end{pmatrix} = \Gamma_\mathrm{p}\begin{pmatrix} 0 - M_x(t) \\ 0 - M_y(t) \\ M_\mathrm{p} - M_z(t) \end{pmatrix} - \Gamma_\mathrm{r}\begin{pmatrix} M_x(t) \\ M_y(t) \\ M_z(t) \end{pmatrix}. \tag{2.8}$$

Here, Γ_p is the pumping rate, Γ_r is the relaxation rate due to as-yet-unspecified relaxation mechanisms (for now assumed to be the same for all magnetization components), and M_p is the maximum magnetization which can be achieved in the absence of relaxation according to this equation, such that eventually $M_\mathrm{p}/M_z = 1$. This expression explicitly assumes that the laser-light direction is parallel to the z-axis, as shown in Fig. 2.2. The pumping rate quantifies how fast the optical pumping works and is proportional to the power of the laser beam. We see that in the absence of relaxation mechanisms, any magnetization in the x- or y-directions tends toward 0 with a rate Γ_p, while the magnetization in the z-direction approaches the value M_p.

Eq. (2.8) can be simplified by defining an effective relaxation rate $\Gamma = \Gamma_\mathrm{p} + \Gamma_\mathrm{r}$ and an effective asymptotic (steady-state) magnetization $M_\mathrm{a} = M_\mathrm{p}\,\Gamma_\mathrm{p}/\Gamma$, which yields

$$\frac{d}{dt}\begin{pmatrix} M_x(t) \\ M_y(t) \\ M_z(t) \end{pmatrix} = \Gamma\begin{pmatrix} -M_x(t) \\ -M_y(t) \\ M_\mathrm{a}\, M_z(t) \end{pmatrix}. \tag{2.9}$$

This means that in the general case of optical pumping along the z-direction, any magnetization in the x- or y-directions tends toward 0 with a rate Γ, while the magnetization in the z-direction approaches the value M_a.

Traditionally, the electromagnetic field that creates the magnetization is referred to as **pump** light, and the one that is used to detect it as **probe** light. However, in many magnetometer arrangements, light from the same laser plays both roles. If all atomic spins in the medium are parallel or antiparallel to the direction of the laser beam—i.e., each atom is in a stretched state, having the maximum amount of angular momentum with respect to the light direction—no atom can absorb a photon, since it would be physically impossible to transfer even more angular momentum to the atom. Thus, the medium has become transparent to the laser light. In general, one can detect the direction of atomic magnetization optically, since the amount of light transmitted through the medium is proportional to the projection of $\vec{M}$ onto the light wavenumber $\vec{k}$. In most systems, transmission is high (absorption is low) for $\vec{M}$ parallel to $\vec{k}$, while transmission is low (absorption is high) for $\vec{M}$ antiparallel to $\vec{k}$. Further discussion of optical detection is provided in Sec. 2.2.5.

Figure 2.3 shows how the magnetization accumulates after optical pumping is started at time $t = 0$. Time is measured in units of the characteristic relaxation time $T_1 \equiv 1/\Gamma_\mathrm{r}$, $T_2 = 1/\Gamma_\mathrm{r}$ and amplitude is measured in units of M_p. The different curves show how the

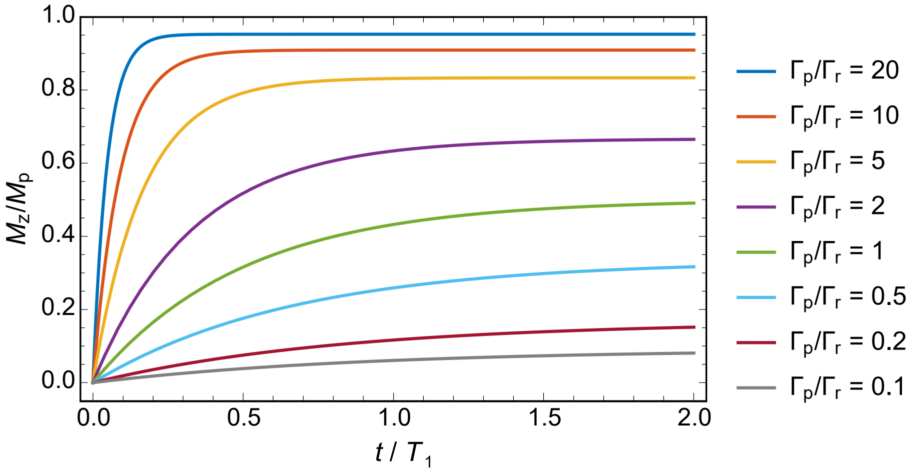

Figure 2.3: Simulation of atomic magnetization as it can be measured by monitoring transmitted light power as a function of time. The different curves show the magnetization behavior for different laser powers and thus different pumping rates Γ_p, defined with respect to the spin relaxation rate Γ_r. For $\Gamma_\mathrm{p}/\Gamma_\mathrm{r} = 20$, a spin-ensemble polarization of approximately 95% is achieved.

magnetization behavior changes as a function of laser power, proportional to the pumping rate Γ_p. All quantities in the graph are dimensionless, and thus the curves are universally applicable when the scaling coefficients Γ_p and M_p are known. Since the transmitted light power is proportional to $\vec{M}\,(t)$, the displayed curves can be easily measured.

Solving Eq. (2.9) yields

$$M_z\,(t) = M_\mathrm{a}\left(1 - e^{-\Gamma\,t}\right) = M_\mathrm{p}\,\frac{\Gamma_\mathrm{p}}{\Gamma_\mathrm{r} + \Gamma_\mathrm{p}}\,\left[1 - e^{-(\Gamma_\mathrm{r}+\Gamma_\mathrm{p})\,t}\right]\,. \tag{2.10}$$

With increasing laser power, the asymptotic magnetization M_a comes closer to its maximum value, given by M_p. It is also evident that the time constant of the exponential approach to steady state is shortened by increasing the laser power. Solving for the steady state, we find that optical pumping alone gives

$$\frac{d}{dt}\begin{pmatrix} M_x\,(t) \\ M_y\,(t) \\ M_z\,(t) \end{pmatrix} = 0 \quad \Rightarrow \quad \begin{pmatrix} M_x\,(t) \\ M_y\,(t) \\ M_z\,(t) \end{pmatrix} = \begin{pmatrix} 0 \\ 0 \\ M_\mathrm{a} \end{pmatrix}. \tag{2.11}$$

2.2.2 Spin-relaxation times

Let us assume that we are able to create a high degree of magnetization $M_z/M_\mathrm{p} \approx 1$ along the z-direction via optical pumping. Looking at Eq. (2.8), we see that if we then turn off the pump beam at time $t = 0$ such that $\Gamma_\mathrm{p} = 0$, the longitudinal magnetization decays as

$$M_z\,(t) = M_z\,(0)\;e^{-\Gamma_\mathrm{r}\,t} = M_\mathrm{p}\,e^{-t/T_1}\,, \tag{2.12}$$

Here we have explicitly introduced the traditional **spin-depopulation time** $T_1 = 1/\Gamma_\mathrm{r}$, which describes how fast the atomic magnetization decays to the unpolarized thermal state—or, in in the presence of a longitudinal magnetic field, to a nonzero equilibrium magnetization.

What happens to the magnetization components transverse to the pumping direction, M_x and M_y, in this case? Until now, we have assumed that the transverse and longitudinal relaxation rates are the same. Although it is possible to add by hand different relaxation rates for each magnetization component in Eq. (2.8), here we begin to reach the limits of the classical description. According to our modeling thus far, in the absence of any additional electromagnetic fields (Sec. 2.2.3), after optical pumping we should effectively have $M_x = 0 = M_y$. This is not the full picture, however, since atomic magnetometers are quantum devices which make use of **spin coherence**. Although the expectation value of each atomic spin along either transverse direction is zero, there are nonzero quantum fluctuations in accordance with the Heisenberg uncertainty principle, as discussed further in Sec. 2.3.1. In the density-matrix description of the atomic spin state [41, 42], the diagonal elements of the density matrix give the m_F-sublevel population probabilities, while the off-diagonal elements represent the coherences (superpositions) among sublevels. These coherences give rise to the transverse spin components, which also decay exponentially with a time constant called the **spin-(de)coherence time** T_2. As explained in Sec. 2.3.1, the T_2 time is a crucial parameter which defines the sensitivity of an atomic magnetometer. In general, the longer the T_1 time in an atomic ensemble, the longer will be the T_2 time as well. Although typically $T_1 \geq T_2$, for purposes of calculation it is often convenient to set $T_1 \approx T_2$. In thermal atomic vapor cells, a dominant spin-relaxation mechanism is collision of atoms with the cell walls (Sec. 2.5.1).

2.2.3 Interaction of atoms with a magnetic field

Apart from optical pumping, the second interaction that drives an atomic magnetometer is the effect of external magnetic fields on the magnetization $\vec{M}$ of the medium. A magnetic field acting on polarized atoms induces a torque that aims to align the magnetization with the field lines. Since the magnetization results from atomic spins with angular momentum, this torque induces a precession motion of the spins, known as Larmor precession. The precession frequency or **Larmor frequency** Ω is proportional to the magnetic field, and it is convenient to express all magnetic-field components in terms of precession frequencies. For example, we define for the x-component $\Omega_x = \gamma\, B_x$,[3] with the gyromagnetic ratio γ (see [51] for the γ values of different alkali atoms). This allows us to model the evolution of M in the following way:

$$\frac{d}{dt}\begin{pmatrix} M_x(t) \\ M_y(t) \\ M_z(t) \end{pmatrix} = \begin{pmatrix} M_x(t) \\ M_y(t) \\ M_z(t) \end{pmatrix} \times \begin{pmatrix} \Omega_x \\ \Omega_y \\ \Omega_z \end{pmatrix} + \Gamma \begin{pmatrix} -M_x(t) \\ -M_y(t) \\ M_\mathrm{a} - M_z(t) \end{pmatrix}. \tag{2.13}$$

The first part of this expression is the classical Bloch equation, which has been extended to model optical pumping along the z-direction as well as relaxation of the magnetization. The equation is useful for a basic description of virtually all processes in optically pumped

---

[3] Note that Larmor frequency is conventionally defined as $\Omega = -\gamma\, B$, which corresponds to righthanded precession for particles with $\gamma < 0$, such as electrons. Here we are only concerned with the magnitude of Ω.

atomic magnetometers. For example, it defines how the optical absorptive and dispersive properties of the atomic medium are modified, which enables optical detection of the change in spin state as discussed in Sec. 2.2.5.

More detailed descriptions of the atom-field interaction can be derived from quantum density-matrix calculations [41, 42, 52].

2.2.4 A specific example: Measuring the transverse magnetic field

Let us have a look at some special cases. First, we assume that we have a magnetic field parallel to the laser beam. In this situation, the pumping process creates magnetization only along the magnetic-field direction. The field induces precession around an axis given by the field direction, which in this case does not change the magnetization at all. Due to the cross-product in Eq. (2.13), the z-component of the field mixes the x- and y-components of the magnetization, which are zero in this case. Thus, the situation is stable, and we find the same result as in Eq. (2.11).

The situation changes when we apply a magnetic field along a direction perpendicular to z—for example, the x-direction. When we solve for the steady state (by setting the time derivatives equal to zero) with $\Omega_y = 0$ and $\Omega_z = 0$, Eq. (2.13) simplifies to

$$\frac{d}{dt}\begin{pmatrix} M_x(t) \\ M_y(t) \\ M_z(t) \end{pmatrix} = \begin{pmatrix} & - & \Gamma M_x \\ M_z\,\Omega_x & - & \Gamma M_y \\ -M_y\,\Omega_x & + & \Gamma\,(M_\mathrm{a} - M_z) \end{pmatrix} = \begin{pmatrix} 0 \\ 0 \\ 0 \end{pmatrix}. \tag{2.14}$$

Apart from the trivial result $M_x = 0$, this equation contains the essence of many atomic magnetometers. In the term for M_y, two contributions have to balance each other in the steady state. The first contribution is a source term that increases the modulus of M_y proportionally to Ω_x, by rotating magnetization from the z-direction to the y-direction. The second contribution is the relaxation, which decreases the modulus of M_y.

The term for M_z has similar contributions, which here have reversed roles. The first one models the loss of M_z as it is rotated to M_y, and the second one is a relaxation towards the asymptotic magnetization M_a. Solving the system of equations yields

$$M_y = M_\mathrm{a}\,\frac{\Gamma\,\Omega_x}{\Gamma^2 + \Omega_x^2} = M_\mathrm{a}\,\frac{x}{1+x^2}\,, \qquad M_z = M_\mathrm{a}\,\frac{\Gamma^2}{\Gamma^2 + \Omega_x^2} = M_\mathrm{a}\,\frac{1}{1+x^2}\,, \tag{2.15}$$

where $x = \Omega_x/\Gamma$ is a dimensionless variable that expresses the magnetic-field component scaled to the corresponding precession frequency and divided by the relaxation rate. Both M_y and M_z show resonant behavior, and the dimensionless parameterization allows us to generate the universally applicable plots shown in Fig. 2.4.

The amplitude of both resonances is given by the asymptotic magnetization M_a. When $B_x = 0$ and consequently $x = 0$, M_z reaches M_a and M_y vanishes. This is the same situation as in Eq. (2.11) for optical pumping alone. The magnetization M_z shows an absorptive Lorentzian peak and thus gets smaller with an increasing magnitude of B_x. At $x = \pm 1$, we find $M_z = M_\mathrm{a}/2$; this means that the half width at half maximum (HWHM) gives the

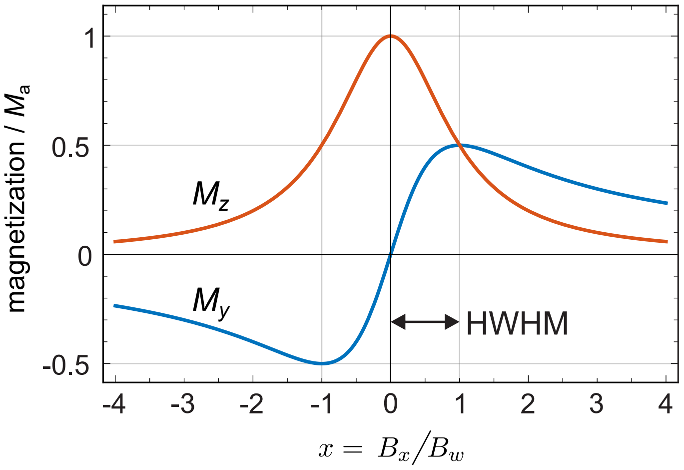

Figure 2.4: Magnetic-resonance spectrum for the case $B_y = B_z = 0$. The M_y and M_z components of the magnetization show resonant behavior as a function of B_{x}. The scale for the x-axis is given by the magnetic linewidth B_{w}. M_y displays a dispersive and M_z an absorptive Lorentzian resonance.

points where the modulus of the precession frequency Ω_x is equal to the relaxation rate Γ. We can define the magnetic linewidth B_{w} by rearranging the terms that define x:

$$x = \frac{\gamma\, B_x}{\Gamma} = \frac{B_x}{B_{\mathrm{w}}} \quad \text{with} \quad B_{\mathrm{w}} = \frac{\Gamma}{\gamma}\,. \tag{2.16}$$

This concept is not limited to the x-component of B, as we shall see in Sec. 2.5.4.

The M_y component follows a dispersive Lorentzian curve with a linear zero crossing. Close to $x = 0$, the M_y component is thus proportional to the applied magnetic field. The larger the change in magnetization signal (relative to noise) produced by a small change in the magnetic field, the more sensitive the magnetometer. This exact method is used in magnetometers based on the ground-state Hanle effect, also known as zero-field resonance, which often operate in the spin-exchange-relaxation-free (SERF) regime (see Sec. 2.4).

2.2.5 Optical detection

The propagation of light through an atomic medium can be modeled semiclassically, whereby the electronic energy levels are quantized but the light is treated as a classical electromagnetic field in which the electrons are oscillating dipoles [53]. Based on its electric polarizability, the atomic medium has a complex index of refraction for light:

$$n\,(\omega) = n_{\mathrm{Re}}\,(\omega) + i\, n_{\mathrm{Im}}\,(\omega)\ , \tag{2.17}$$

expressed as a function of the angular frequency ω of the incident light. Here n_{Re} defines the real index of refraction, characterized by dispersive behavior as a function of ω; n_{Im} defines the absorption, characterized by resonant behavior at the resonance frequency $\omega = \omega_0$. At resonance, $n_{\mathrm{Re}} = 0$ and $n_{\mathrm{Im}} = 1$, in analogy to the behavior of the magnetization curves in Fig. 2.4. This duality enables two different modes of optical detection in atomic magnetometry, either absorptive (based on light transmission) or dispersive (based on light polarization rotation).

An external magnetic field creates birefringence in the atomic medium, such that the σ_+ and σ_- polarization components of incident light along the magnetic-field direction experience different values of n. Depending on the detection mode, this manifests as a change in absorption or polarization rotation of the transmitted probe light. In both cases, the change is proportional to the projection of the atomic magnetization in the direction of light propagation, from which the Larmor frequency can be extracted.

2.3 Define your requirements: Figures of merit

When designing a magnetometer, the following questions should first be considered in order to select an appropriate operating mode (Sec. 2.4). They relate the application requirements to associated magnetometer performance figures, some of which were already introduced in Sec. 2.1.

1. What are the amplitude and frequency ranges of the signals I want to measure? → **sensitivity, bandwidth**
2. How close must the sensing volume be to the sample? How well do I need to localize the measured signals? → **standoff distance, spatial resolution**
3. Am I interested in measuring absolute or relative field values? → **accuracy**
4. Over what time scale do I plan to measure? → **stability**

2.3.1 Sensitivity and noise

Sensitivity to magnetic fields is arguably the most important benchmark used to characterize magnetometer performance. In atomic magnetometry, sensitivity is typically reported in units of $\mathrm{T}/\sqrt{\mathrm{Hz}}$ (SI) or $\mathrm{G}/\sqrt{\mathrm{Hz}}$ (CGS). Although these units may appear mysterious to newcomers, they can be understood by noting that magnetic-field noise fluctuates over the frequency bandwidth of a magnetometer. In order to measure sensitivity, one records the magnetometer response for some time duration. To convert from the time domain to the frequency domain, a fast Fourier transform (FFT) is performed to produce a magnetic-field-noise power spectrum (see Sec. 2.6).[4] Calculating root-mean-square (RMS) amplitudes of the noise in 1 Hz bins leads to a sensitivity expressed per $\sqrt{\mathrm{Hz}}$. Note that although both sensitivity and **resolution** are essentially a measure of the smallest change in magnetic field detectable by the sensor (at a given frequency), the units are different—resolution is reported in magnetic-field units alone.

For measurement of relatively small magnetic fields, we would like the sensitivity of our magnetometer to be as good as possible—in the ideal case, limited only by fundamental quantum mechanics. It is important to identify the various contributions to noise in our measurements, and to understand how they behave.

---

[4] The topic of FFTs is further treated in Ch. 4.

The basic sensitivity limits for an atomic magnetometer are set by the Heisenberg uncertainty principle, which manifests in the **spin-projection noise** δB_{PN} of the atoms and the **shot noise** δB_{SN} of the probe light. These contributions to the magnetometer sensitivity scale as [1]

$$\delta B_{\mathrm{PN}} \propto \frac{1}{\sqrt{N\,T_2\,t}}\,, \tag{2.18}$$

$$\delta B_{\mathrm{SN}} \propto \frac{1}{\sqrt{\Phi\,t}}\,, \tag{2.19}$$

where N is the number of atoms in the ensemble, T_2 is the spin-coherence time of the ensemble introduced in Sec. 2.2.2, Φ is the photon flux of the probe light, and t is the total measurement time. We see that noise decreases the longer we measure, corresponding to a better sensitivity and underscoring the value of averaging over many measurement cycles. In order to express Eqs. (2.18–2.19) as noise densities (per $\sqrt{\mathrm{Hz}}$), we can multiply by $\sqrt{t}$.

Spin-projection noise is a type of **atomic noise** that ultimately limits the sensitivity of any atomic magnetometer regardless of the particular modality or detection method. In order to understand this limit, it is instructive to consider a single atom. Imagine that we prepare the atom in a stretched state along the z-direction, as described in Sec. 2.2, and then measure the atomic-spin projection m_F along some axis. If this experiment is repeated a number of times, we find the expectation value $\langle F_z \rangle = F$. Along the x- and y-directions we measure zero on average, but each individual measurement yields a random result according to the uncertainty principle:

$$\Delta F_x\,\Delta F_y \geq \frac{\langle F_z \rangle}{2}\,, \tag{2.20}$$

which in the case of the minimum-uncertainty stretched state becomes

$$\Delta F_x\,\Delta F_y = \frac{F}{2}\,. \tag{2.21}$$

A derivation of Eq. (2.18) may be found in Sec. 2.8.2. As explained in quantum-optics textbooks, it is possible to beat the limit set by Eq. (2.21) for ΔF_x or ΔF_y (but not both simultaneously) via a technique known as **spin squeezing**, such that the magnetometer sensitivity may be improved [54]. Squeezing of the probe light may also be employed to beat sensitivity limits set by photon shot noise. Such “quantum-enhanced” atomic magnetometry is an active area of research [55–61].

Another quantum-mechanical source of atomic noise is **back-action noise**. This stems from the fundamental problem of not being able to measure a quantum system without disturbing it. In the case of atomic magnetometry, we use light as a detection tool since we cannot read out the atomic spin states directly. This interference by the experimenters results in “back action” of the light onto the atoms—essentially an AC Stark shift, also known as light shift, caused by the probe light which shifts the hyperfine energy levels and changes the Larmor precession frequency. In effect, a “fictitious magnetic field” is generated on top of the real one that we actually want to measure. Various evasion techniques have been developed for reducing or eliminating back-action noise [62, 63]. Since, in contrast to shot noise (Eq. (2.19)), the contribution of back-action noise to sensitivity scales as $\sqrt{\Phi}$, one does not generally gain by increasing probe power—which can also introduce additional atomic noise due to undesirable depumping effects.

In practice, there may be additional systematic sources of noise that worsen the sensitivity of a magnetometer, including **electronic noise** and **technical (classical) noise**. These categories are, of course, somewhat artificial, as some electronic noise may be classical. Furthermore, some classical noise may be atomic—according to our definition, atomic noise is anything that causes **broadening** of the magnetic resonance. Since the resonance linewidth is inversely proportional to the spin-coherence time T_2, sensitivity worsens in the presence of any such broadening. One common source of classical atomic noise is magnetic-field gradients. Systematics are discussed further in Sec. 2.4.2.

Whether or not it is necessary to suppress systematic noise sources enough to achieve so-called quantum-noise-limited operation depends on the application requirements. In any case, it is considered best practice to remove electronic noise from the photodetector signal by measuring and subtracting dark counts. For detection modalities based on light polarization rotation (Sec. 2.4), many classical noise sources can be removed via homodyne-detection schemes, a common technique in quantum optics [64]. Absorption-based detection modalities, while generally simpler to implement, are more prone to systematics due to, e.g., laser-intensity noise.

Going back to Eq. (2.18), we also see that in order to optimize sensitivity—i.e., to make it as small as possible—one should increase both the number of atoms and the coherence time inside the vapor cell. The latter can be accomplished in two ways: (1) by using **antirelaxation wall coating** that has low absorption energy for the atoms, so that they spend less time at the cell walls, or (2) by using a **buffer gas** to prevent atoms from diffusing to the walls. Both these techniques, which are discussed further in Sec. 2.5.1, are effective because spin relaxation at the cell walls is a key relaxation mechanism [65, 66]. A popular way to increase the density of atoms is by heating the vapor cell—SERF magnetometers work at temperatures over 100°C (Sec. 2.4).

2.3.2 Bandwidth and spatial performance

One often hears the statement that in magnetometry, there exists a trade-off between sensitivity and bandwidth, i.e. that improving the sensitivity comes at the cost of reduced bandwidth and vice versa. This is because these two parameters tend to have an opposite dependence on the the width of the atomic resonance. Narrow resonances may provide better sensitivity (which is good), but smaller bandwidth (which is usually bad). Another way to think about this intuitively is to recall that bandwidth gives us information about how quickly a magnetometer responds to sudden changes in magnetic field: the smaller the change to which the magnetometer is sensitive, the longer it takes for the magnetometer to react to this change. A directly related concept is **dynamic range**, or the range of field magnitudes that can be measured within the magnetometer response bandwidth.

The sensitivity-bandwidth trade-off is not the only one arising in the context of magnetometer performance figures. We have already seen that we want to maximize the number of atoms in the sensing volume, as per Eq. (2.18). Naively, this suggests that we should make the sensing volume as large as possible. Regardless of the cell volume, for atoms in thermal motion, the probe light effectively interacts with all atoms equally, such that the motion of individual atoms averages out and we can think of the light as addressing a homogeneous atomic ensemble, a principle known as motional averaging. In the case of buffer-gas cells, where the atoms are prevented from diffusing to the cell walls, the size of the probe beam is typically chosen to interact with a majority of atoms in the cell. However, a larger volume tends to increase the sensor standoff distance and decrease the spatial resolution of measurements.

More precisely, the standoff distance of a sensor is generally defined as the distance between the sample of interest and the geometric center of the sensing volume; the spatial resolution is the smallest spatial variation in the measured signal that can be resolved. Thus, we may run into trouble if we want to localize signals to within distance scales smaller than the diameter of the sensing volume. One way around this is to decrease the size of the sensing volume but increase the atomic density via heating, ideally in the SERF regime. Arrays of miniaturized vapor cells can be used to obtain excellent spatial localization and mapping of magnetic signals (Secs. 2.4.2 and 2.5.1). An alternative way to effectively increase the atomic density, by actually increasing the light-atom interaction, is to place the vapor cell in an optical cavity or to use a multipass cell [67–70].

2.3.3 Stability and accuracy

Stability essentially refers to how long a magnetometer can operate continuously, or continually in pulsed mode, before it needs to be recalibrated. For example, some popular commercially available sensors operate at zero field via integrated field coils which null the local magnetic field. However, any drifts in the local magnetic-field environment over time eventually push the sensor out of its sensitive range, limiting the duration of continuous magnetometer operation. For longer-term sensor usage demanding greater stability with limited power consumption, e.g. in non-lab settings, a self-oscillating mode of operation is preferred which renders the magnetometer insensitive to such drifts; the NMOR magnetometers discussed in Sec. 2.4 are ideal in this case. Feedback control of various other time-dependent sensor parameters, such as laser frequency and cell temperature, is typically also required for practical operation. A standard way to quantify the stability of a magnetometer, or other frequency-based measurement device, is to calculate the Allan variance over time [71].

Finally, the accuracy of a sensor has to do with whether we are measuring absolute or relative magnetic-field values—in the latter case, this performance figure is less critical. In essence, magnetometers measure frequencies which must be converted to corresponding magnetic-field values. For some applications, such as precise mapping of the geomagnetic field and other coarse magnetic structures, or precise measurement of physical constants, accuracy is paramount and may outrank sensitivity as the dominant figure of merit [31, 72]. Since atoms form the heart of the magnetometers under consideration here, these can be used as an absolute reference during magnetometer calibration, in order to improve accuracy. In practice, however, various systematics may worsen measurement accuracy during magnetometer operation (Sec. 2.4.2).

2.4 Choose your operating mode

As discussed in Sec. 2.2, most atomic magnetometers have a similar underlying physical principle of operation, relying on a resonant change in either light absorption or rotation of the light polarization to determine the Larmor precession frequency and extract the magnetic-field value. Yet, this operational principle allows for many different configurations, each having its own strengths and weaknesses. The choice of a particular approach is usually dictated by the desired magnetometer performance and other application-specific restrictions. In this section, we provide a brief comparative analysis of the main approaches for magnetic-field measurements and their basic performance characteristics, as summarized in Table 2.2.

2.4.1 Common types of atomic magnetometers

We saw in Sec. 2.2.1 that many atomic magnetometers rely on circularly polarized light, tuned near one of the atomic optical transitions, to optically pump atoms and create the desired magnetization of the atomic ensemble. Among these devices, summarized in the first four columns of Table 2.2, the most common are probably M_z and M_x magnetometers, so named for the magnetization component to which the device is sensitive. Both of them utilize a resonant radiofrequency (RF) field to induce an optical absorption resonance. The other two magnetometers of this type are all-optical: in Bell-Bloom magnetometers, amplitude modulation of the optical field plays the role of the effective RF interrogation, and, unlike others, this type of magnetometer can operate as an active device if the output signal of a photodetector is fed back into the modulation circuit. Finally, Hanle magnetometers use a pump-probe geometry, in which atomic spins are oriented with a circularly polarized strong pump optical field, and then their precession in the bias magnetic field is probed through the polarization rotation of a weaker probe optical field. The most successful realization of the Hanle magnetometer operates in the SERF regime, which has now become a well-recognized magnetometer type in its own right. The magnetometer operating principles in the first four columns of Table 2.2 may be loosely categorized under the umbrella of “magneto-optical double resonance”—a general term which refers to the dual combination of optical and magnetic resonances, manifested physically when the frequency of an applied or effective RF field matches the Larmor frequency. This concept and its

Magnetometer type	**Mz**	**Mx**	**Bell-Bloom**	**Hanle/SERF**	**NMOR**	**CPT/EIT**
Typical geometry	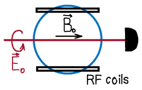	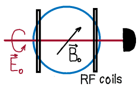	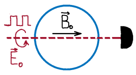	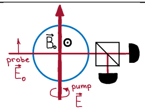	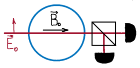	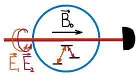
Operational principle	Circularly polarized light $\vec{E}_0$, parallel to the bias magnetic field $\vec{B}_0$, magnetizes atoms along the z-axis. An orthogonal resonant RF field at the Larmor frequency produces a narrow absorption resonance [15, 73].	Circularly polarized light $\vec{E}_0$ propagates at an angle to the bias magnetic field $\vec{B}_0$ and along the oscillating RF field. Light absorption is defined by the transverse magnetization component [15, 74–76].	Intensity modulation of the laser light $\vec{E}_0$ produces stroboscopic optical pumping when modulated at the Larmor frequency [77, 78].	Circularly polarized pump light $\vec{E}$ sets the atomic magnetization, whose orientation imprints on the polarization angle of a weak probe $\vec{E}_0$. Often operates in the spin-exchange relaxation-free (SERF) regime [67, 79].	Linearly polarized light $\vec{E}_0$ aligns the atoms, whose precession in the magnetic field $\vec{B}_0$ imprints back onto the light polarization angle [80–82]. Use of the modulated light enables operation at nonzero magnetic field [83, 84].	A bichromatic optical field $\vec{E}_{1,2}$ prepares atoms in a superposition of magnetosensitive hyperfine sublevels with increased transmission ("dark state") [85, 86].
Sensitivity fT/$\sqrt{\mathrm{Hz}}$	10 [87]	1 [74]	20 [88–90]	0.16 [91]	70 [92]	10 000 [86, 93]
Bandwidth kHz	0.6 [87]	1 [94, 95]	1 [90]	1 [95, 96]	>100 [97]	>0.1 [98, 99]
Can operate at Earth field?	yes	yes	yes	no	yes	yes
Has been modified for vector measurement?	no	[100]	[69, 101, 102]	[103, 104]	[105, 106]	[107]
Miniaturization cell volume | sensor volume | sensitivity	1 mm^3 | 22 cm^3 | 15 pT/$\sqrt{\mathrm{Hz}}$ [108, 109]	2 mm^3 | 25 mm^3 | 5 pT/$\sqrt{\mathrm{Hz}}$ [108, 110, 111]	16 mm^3 | NA | 0.07 pT/$\sqrt{\mathrm{Hz}}$ [111–113]	6 mm^3 | NA | 0.07 pT/$\sqrt{\mathrm{Hz}}$ [96, 114]	$7 \cdot 10^{-4}$ mm^3 | NA | 700 pT/$\sqrt{\mathrm{Hz}}$ [115]	1 mm^3 | 12 mm^3 | 50 pT/$\sqrt{\mathrm{Hz}}$ [116, 117]

Table 2.2: Brief summary of the main atomic-magnetometer technologies.

experimental demonstration in atomic spectroscopy predate magnetometry applications [118, 119].

By contrast, the devices in the last two columns of Table 2.2 rely on evolution of a quantum superposition of atomic spin states, rather than on magnetization. Magnetometers based on nonlinear magneto-optical rotation (NMOR) generally employ linearly polarized light to create atomic alignment (Sec. 2.2)—a quadrupole magnetic moment, corresponding to a coherent superposition of Zeeman sublevels—and then detect the optical polarization rotation caused by alignment evolution in the magnetic field to be measured. Typically, such measurements are done using amplitude- or phase-modulated optical fields (similar to the Bell-Bloom approach) to enable detection at nonzero magnetic field. Finally, if atoms are prepared in a non-interacting coherent superposition of the hyperfine atomic states (usually referred to as a "dark state") via coherent population trapping (CPT), the magnetometer uses an associated transmission resonance (electromagnetically induced transparency, or EIT) to measure the magnetic-field value.

It is important to emphasize that this list is not exhaustive and that there are no clear boundaries between different methods. Indeed, many researchers have successfully combined the characteristic features of two or more of these techniques: examples include the M_z-M_x

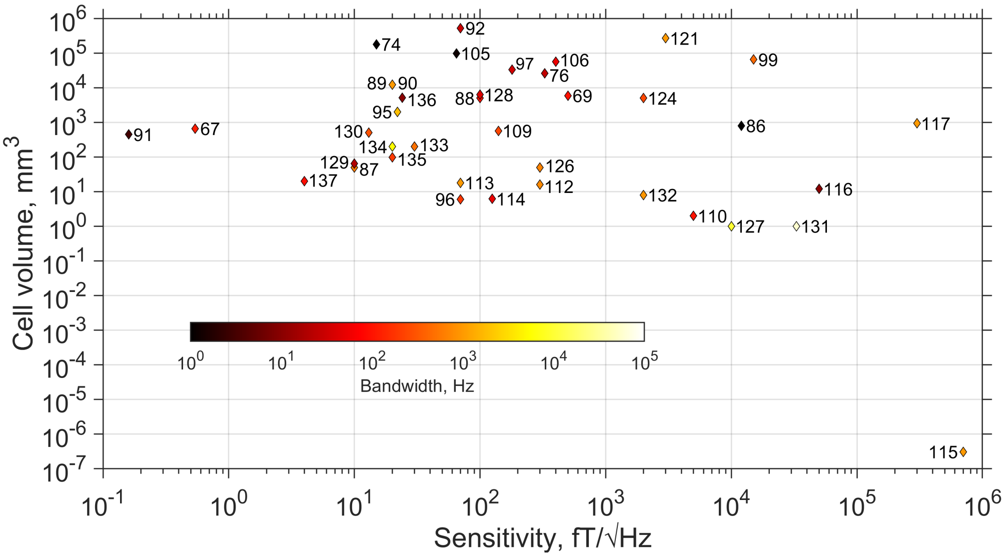

Figure 2.5: Characteristics of various atomic magnetometers [67, 69, 74, 76, 86–92, 95–97, 99, 105, 106, 109, 110, 112–117, 121, 124, 126–137] utilizing atomic vapor cells: magnetic-field sensitivity, cell volume, and measurement bandwidth (indicated by color). For cases where a gradiometric configuration was used, the volume of a single cell is given.

tandem [120, 121], RF atomic magnetometers sensitive to RF magnetic fields [62, 122], magnetometers based on free spin precession [123], active self-oscillating magnetometers [93, 124], and many others. A commercial example is the QuSpin zero-field magnetometer mentioned in Table 2.1, which is essentially a Hanle/SERF device using a single-beam M_z-type geometry to measure transverse magnetic fields [125]. Not included in Table 2.2 are non-alkali atomic-magnetometer types—such as those employing the technique of parametric resonance, an established subfield of fundamental and applied magnetometry research [28–30].

2.4.2 Typical performance characteristics of different magnetometer types

The choice of an optimal method for magnetic-field measurements depends on the application and the expected performance. Altogether, existing atomic magnetometers span a very wide range of achievable characteristics, as shown in Fig. 2.5. It is easy to trace some general trends, discussed in Sec. 2.3: for example, more sensitive devices tend to use larger vapor cells and operate at lower bandwidth. Since a given type of magnetometer may or may not be suitable for a particular application, here we discuss some specific requirements that can be important when making the choice.

What sensitivity does my application require? Hanle magnetometers operating in the SERF regime [77] (usually just referred to as "SERF magnetometers") are currently the most sensitive among all atom-based devices by a wide margin, reaching down to the sub-fT range—although their sensitivity may vary widely depending on the experimental parameters, such as cell size, light-source characteristics, etc. As such, they can easily compete with SQUIDs in performance without the need for bulky cryogenics. It is important to note, however, that such magnetometers are most sensitive at zero magnetic field, and thus optimal for measuring the faintest magnetic fields in a shielded environment, such as MEG signals. In fact, the commercially available atomic magnetometers (Table 2.1) are primarily designed with MEG applications in mind. As discussed in Sec. 2.3, there is also an expected trade-off in performance, as SERF magnetometers tend to have limited dynamic range and a potentially larger volume. While these challenges can be overcome with clever engineering, for a number of applications with less stringent sensitivity requirements it may be simpler to use alternative approaches that can provide sensitivity at the level of tens of fT while operating in a fairly large background optical field (Sec. 2.5).

What is the expected magnetic-field magnitude? One important characteristic to consider is the base level of the measured magnetic fields. Some magnetometers (M_z/M_x, Bell-Bloom, CPT/EIT) are intrinsically designed to operate at nonzero bias magnetic field, since the measured Larmor frequency value directly appears at the frequency of the RF field or modulation. These methods are well-suited for applications in Earth's magnetic field—for example, geomagnetometry or medical diagnostics in a magnetically unshielded environment [138]. Notably, the basic NMOR effect was also initially restricted to near-zero-field measurements, but later modifications using amplitude- or phase-modulated lasers rendered it possible to extend the operational range of NMOR-based magnetometers up to Earth field.

Which magnetic-field parameters need to be measured? Most atomic magnetometers are intrinsically **scalar**, as the measured spin-precession frequency depends only on the magnitude of the magnetic field. However, the expected direction of the magnetic field must be taken into account even when constructing a scalar magnetometer, due to the possibility of **heading error** (the dependence of the readout on the orientation of the sensor in space) [139–141] or blind spots (the inability of the sensor to measure magnetic field in certain orientations). If information about the direction of the magnetic-field vector is required by the application, various strategies have been explored to enable operation in the **vector** modality. Most magnetometers based on the Hanle effect are intrinsically sensitive to one vector component only. Apart from that, the most common approach is to use three pairs of mutually orthogonal external magnetic-field coils to zero the magnetic field at the sensor location. In this case, the electric current in each coil can be translated into a corresponding magnetic-field component. Alternatively, the field orientation, together with the light polarization, determines the selection rules and relative strength of the involved optical transitions, and thus the vector field information may be deduced from the optical-resonance position or amplitude (or both).

How fast is the magnetic field changing? In general, speed of operation is not one of the strengths of atomic magnetometers. Their exceptional magnetic sensitivity originates from long lifetimes of atomic magnetization (Sec. 2.2.2), which may range from tens of milliseconds to tens of seconds depending on the size and quality of the vapor cell. However, that renders them unable to respond quickly to rapid changes in the magnetic field, limiting their operational bandwidth. Some strategies have been proposed to break this limit. For example, the operational bandwidth was successfully extended by several orders of magnitude by using active feedback to adjust the pump modulation frequency in NMOR and SERF magnetometers [97, 134], albeit with proportional deterioration of sensitivity. Alternatively, a causal waveform estimation using Kalman filtering was demonstrated to accurately predict the magnetic-field variations at time scales shorter than the sensor's intrinsic time resolution, without paying the sensitivity penalty [142].

Can the sensor operate in a gradiometric configuration? Accurate measurements of the magnetic field using optical-atomic magnetometers may also be challenging due to a number of potential systematics, such as heading errors caused by orientation-dependent light shifts and the nonlinear Zeeman effect [139–141]. Moreover, as mentioned in Sec. 2.3.1, the sensitivity of measurements may be limited by technical noise from the laser or electromagnetic background coupling to the atomic spins. Some of these issues can be resolved by operating the magnetometer in gradiometer mode, in which two or more nominally identical probe regions are introduced inside the sensor to conduct differential measurements. Of course, this approach is only effective if the expected source of the magnetic field is well-localized and has a distinctly different value for each probe region. In this case, any common-mode noise will be suppressed in the differential signal, while maintaining the same useful signal. On the other hand, when it is necessary to reconstruct a detailed spatial map of the magnetic field, one must usually employ arrays of sensors [5, 23, 135, 143]. In these cases, additional system characteristics must then be considered, such as the common-mode rejection ratio, relative gain and phase stability, low crosstalk, etc., across multiple sensors.

Are there any restrictions on the physical size of the sensor? Eq. (2.18) clearly illustrates the advantages of larger sensor size: with a larger cell, one can increase the number of interacting atoms and reduce the magnetization decay due to collisions with the cell walls. Indeed, the best sensitivity for all types of atomic magnetometers has been demonstrated in cells with a few-cm^3 volume. However, as discussed in Sec. 2.3.2, a large sensor size severely limits the spatial resolution as well as the achievable standoff distance. Many applications place restrictions on the sensor dimensions, unavoidably compromising their sensitivity, while also increasing the risk of exposure to magnetic-field gradients. Indeed, while most types of magnetometers have been successfully shrunk to few-mm^3 cell volumes, the average sensitivity of such miniature versions dropped to a few pT/$\sqrt{\text{Hz}}$. Notably, the magnetometers with purely optical interrogation (NMOR, EIT, Bell-Bloom) seem better suited for extreme miniaturization to chip-scale sensor sizes, whereas the need for rf coils around the cell poses additional geometrical limitations for M_z and M_x magnetometers. An alternative approach to enhancing spatial resolution in larger buffer-gas cells with low spin diffusion is to use multiple probe beams and a photodiode array, thereby subdividing the cell into multiple effective miniature sensing volumes [54]. Finally, to obtain true sub-wavelength magnetic-field resolution, nanocells can be utilized [144].

2.5 Choose your components and assemble your magnetometer

In Sec. 2.2 we derived the basic equations (2.15) for the zero-field resonances of a Hanle/SERF magnetometer, which was further discussed in Sec. 2.4. In the derivation we assumed that $\Omega_y = 0$ and $\Omega_z = 0$, which means that this kind of magnetometer works only in conditions where all components of the magnetic field are close to zero. We assumed further that the optical pumping is along the z-direction (Fig. 2.2). Consequently, the measurement of the M_y component must not contribute to the optical pumping and thus must rely on a measurement principle that does not involve resonant circularly polarized light. Both conditions can be achieved experimentally but typically require good magnetic shields, magnetic compensation coils in all directions, and a second laser to produce probe light. For the rest of this section, however, we mainly focus on magnetometer schemes that are easier to implement, in particular the M_z mode of operation (Table 2.2).

Monitoring the transmission of the laser, used for optical pumping, also allows us to measure the M_z component. While the absorptive Lorentzian line shape is perfectly suited for the optimization of the magnetometer (Sec. 2.5.3–2.5.4), it does not give us a signal proportional to the magnetic field, as was derived in Eq. (2.15). To obtain such a signal requires generating the derivative of the absorptive Lorentzian. This is typically achieved by applying an additional oscillating magnetic field using a coil. Figure 2.2B shows the setup in which a function generator drives the modulation coil with a sinusoidal current $B_m(t) = A_m \sin(\omega_m t)$. The frequency ω_m of the modulation has to be slow enough that the magnetization does not deviate significantly from its steady state, which means that $\omega_m < \Gamma$. The derivative of the Lorentzian is generated when the signal from the photodiode is demodulated using a lock-in amplifier [145]. Internally, the lock-in determines the amplitude of the signal component at a given reference frequency, which should be the same as ω_m. The output of the lock-in (Fig. 2.6) is phase-sensitive: positive when the signal and the reference are in-phase and negative when they are out-of-phase. Thus, on the rising slope of the Lorentzian the output is positive and on the falling slope it is negative.

This is still not the full picture for an M_z magnetometer, since in general we do not measure only around $B_x = 0$, and the magnetometer can operate in an unshielded environment at Earth field (Table 2.2). So how can a useful absorption signal be generated? As usual, we return to the modified Bloch equation, Eq. (2.13), and write out the time derivatives of the magnetization components for our case:

$$\frac{d}{dt}\begin{pmatrix} M_x(t) \\ M_y(t) \\ M_z(t) \end{pmatrix} = \begin{pmatrix} M_y\,\Omega_z & -M_z\,\Omega_y & -\Gamma\, M_x \\ M_z\,\Omega_x & -M_x\,\Omega_z & -\Gamma\, M_y \\ M_x\,\Omega_y & -M_y\,\Omega_x & +\Gamma\,(M_a - M_z) \end{pmatrix}. \tag{2.22}$$

For simplicity we continue to assume that the longitudinal and transverse atomic-spin components exhibit the same relaxation behavior, i.e. $T_1 \approx T_2$ (Sec. 2.2.2). Solving the

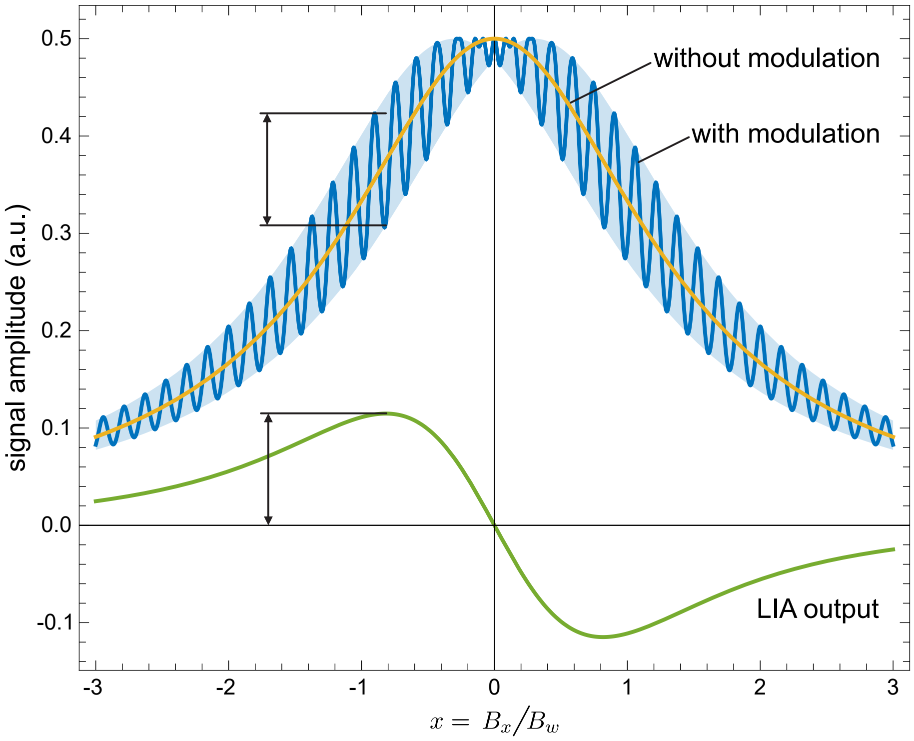

Figure 2.6: Generation of a dispersive signal from an absorptive signal, using a lock-in amplifier.

system of equations for the steady state, we find the longitudinal term

$$M_z = M_a \frac{\Gamma^2 + \Omega_z^2}{\Gamma^2 + \Omega_x^2 + \Omega_y^2 + \Omega_z^2} \, . \tag{2.23}$$

Thus, we see that a small amplitude change in either of the transverse fields will modulate M_z, but there is also a messy dependence on changes in the longitudinal field.

Luckily, clever tuning of the modulation coil to the Larmor frequency Ω_z generates a DC absorption dip which allows us to measure and track changes in B_z. This is best understood in the reference frame rotating around the z-axis at the Larmor frequency Ω_z. An atomic spin at rest in this rotating frame effectively experiences $B_z = 0$. If the additional field is applied along the x-direction, $B_{\mathrm{RF}} = \sin(\omega_{\mathrm{RF}}\, t)$ in the laboratory frame, it appears in the rotating frame as a static field $B_{\mathrm{RF}}\, \hat{x}$ when the resonance condition $\omega_{\mathrm{RF}} = \Omega_z$ is met. Thus, the spin will tend to rotate around $\hat{x}$ in the y-z plane. This tipping of the spin away from $\hat{z}$ produces a resonant dip in the absorption signal measured by the photodetector. In order to generate a dispersive signal for locking to the resonance, the oscillation frequency of the applied field can be modulated around Ω_z.

We shall now present some important aspects of magnetometer assembly, which will prepare us for discussion of actual operation in Sec. 2.5.4.

2.5.1 Choice of atomic system and vapor cell

Why do we use alkali atoms in atomic magnetometers?

An alkali atom has a single valence electron, which makes it an ideal candidate for optical pumping and control of the electronic angular momentum (Sec. 2.2.1).

Does it matter which alkali atom I choose?

In many cases, the choice of atom may be informed by strictly technical considerations such as availability of lasers at the appropriate wavelengths. Beyond that, requirements of the particular application should be considered. For example, different atomic species have different vapor pressures, with the vapor pressure of cesium being higher at any given temperature than that of rubidium, potassium, sodium, or lithium [51]. This makes cesium a popular choice for operation near room temperature [24, 62]. The frequency resolution of different isotopic and hyperfine lines in the atomic spectra also varies by atomic species, and is an important consideration for magnetometry modalities requiring such resolution. For applications requiring robustness in non-laboratory conditions, potassium is a favorite due to its narrowband spectral lines.

Should I heat my vapor cell?

As discussed in Sec. 2.3.1, since the sensitivity of a magnetometer is ultimately limited by the number of atoms in the interaction volume (Eq. (2.18)), it is beneficial to increase this number as much as possible. In order to increase the atomic density without increasing the overall cell size, one typically heats the cell above room temperature. Different techniques are possible, including ovens and coil-based heating systems using high-resistance wire [146]. Care must be taken to avoid heating gradients which can damage the cells, particularly if antirelaxation coating is used—another reason why buffer-gas cells are preferred for higher-temperature operation. Coated cells are intended to be heated to temperatures up to around 40°C, depending on the exact chemical composition of the coating used. Radiation trapping of spontaneous emission may also play a negative role at higher atomic densities, unless quenching buffer gas is introduced [147, 148].

I need a microfabricated vapor cell—what are my options?

Although we saw in Sec. 2.3 that reducing the number of atoms worsens the sensitivity of a magnetometer, there may be strong motivations for miniaturization—including reduced standoff distance and improved spatial resolution, or integration of the cell into small quantum systems [23, 96, 111, 113–115, 149–151] with low size, weight, and power (SWaP). Production of MEMS ("microelectromechanical systems") vapor cells for magnetometers and atomic clocks is a rapidly growing field, typically incorporating anodic-bonding techniques [152–154]. Most MEMS vapor cells are filled with buffer gas, although antirelaxation-coated cells may offer advantages for biological applications where elevated-temperature operation is problematic [24, 155].

2.5.2 Laser systems and magnetic shielding

Nowadays there are a number of commercial laser systems suitable for atomic magnetometry available at various price ranges, including edge-emitting and distributed-feedback (DFB) diode lasers and vertical-cavity surface-emitting lasers (VCSELs). An inexpensive but more time-consuming option is to construct a homemade device using a laser-diode element. The main requirement in any case is single-mode operation around the alkali optical transition of interest, so frequency stabilization of the probe light is critical. (An introductory treatment of the theory of laser locking, also relevant to frequency stabilization generally, can be found in [156].) Laser power requirements may vary according to the specific magnetometer implementation; in devices utilizing two separate probe and pump beams, higher power is required for optical pumping than for probe readout.

When conducting sensitive magnetometry measurements at zero field, for example in the SERF regime, one needs to reliably shield atoms from unwanted ambient fields. Therefore the cell is contained in a nested magnetic-shielding structure, which may be small enough to fit on a laser table or large enough for experimenters to enter (magnetically shielded room [157]). The innermost layers of the shield typically contain a system of coils to produce the desired DC and/or RF magnetic fields for magnetometer operation, as well as to compensate for field gradients in the cell volume. The surrounding layers usually consist of mu-metal and iron, while strategically placed holes in the shield enable access for laser beams and cables. Mu-metal is a nickel-iron alloy with high magnetic permeability. The idea behind magnetic shielding is not actually to block external fields, but rather to provide a literal "path of least resistance" for the magnetic field lines. Since the permeability, and therefore the effectiveness, of mu-metal varies with field strength, several layers can be used to successively reduce the unwanted fields: an outermost iron layer takes care of stronger fields, since iron saturates at a higher field strength than does mu-metal. Such tabletop shielding systems are commercially available, offering shielding factors on the order of 10^6 in the central region, or may be machined according to individual requirements. To further improve shielding performance, active compensation coils may be used, with current state-of-the-art solutions even enabling MEG measurements from human subjects in motion within shielded rooms [158].

Of course, many atomic magnetometers operate unshielded within Earth's field (typically at the cost of sensitivity performance, see Table 2.2), or unshielded within field-canceling coil systems [98, 103, 159]. For Earth-field operation, it may be especially desirable to operate in a gradiometric configuration [151].

2.5.3 Cell performance

Before being used for magnetometry or any other experiment, an atomic vapor cell must undergo a testing process in order to verify that several requirements are fulfilled:

- There are in fact atoms in the cell.
- The density of atoms is sufficiently high.
- It is possible to create a high-quality spin-polarization state (magnetization).
- The buffer-gas or coating quality (see below) is such that the decay time T_1 of the magnetization is adequately long.

Further information about how to conduct such tests may be found in various introductory references and theses covering absorption spectroscopy, optical pumping, and spin-relaxation measurements [146, 160, 161].

What is the difference between buffer-gas and antirelaxation-coated vapor cells?

The smaller the magnetization relaxation rate, the longer the atomic spins can precess in the magnetic field and the more accurately the magnetic field can be measured (Sec. 2.3.1). While ground-state spin coherence of alkali atoms isolated from the environment can live almost indefinitely long, there are many experimental factors that limit its lifetime. Random motion of thermal atoms inside a glass cell inevitably leads to their collisions with the cell walls, which effectively destroy any prior magnetization and lead to thermalization of the atomic spin state. Thus, in an evacuated cell the effective spin relaxation rate is determined by the average time it takes for atoms to cross the laser beam (known as transient time). For a typical few-mm-wide laser beam, this time is limited to a few microseconds.

To extend the spin-relaxation time T_2, two common strategies are employed. In one, a buffer gas is added to the cell, so that alkali atoms undergo diffusive, rather than ballistic motion. This way, the T_2 time can be significantly lengthened. The choice and pressure of the buffer gas is typically customized for each cell geometry: while higher pressure increases atomic transient time, it also increases resonance collisional broadening and shifts [48]. Most common buffer gases are inert gases with low collisional cross-sections (Ne, He, Ar, etc.), although nitrogen (N_2) is commonly used to quench spontaneous emission. The main advantages of using cells with buffer gas are their scalability (the shorter transient time due to reduction in the cell volume can be at least partially compensated by an increase in buffer-gas pressure) and relative manufacturing simplicity. Notably, collisions with buffer gas are not always bad: a high collision rate plays a crucial role in the excellent performance of SERF magnetometers (Sec. 2.4), as it allows for suppression of the spin-exchange decoherence mechanism in a dense vapor [77]. At the same time, there are some potentially serious drawbacks: buffer gas effectively “freezes” atoms in their locations, making the system more susceptible to local magnetic-field gradients and inhomogeneous optical pumping. Also, collisional dephasing of the excited state is typically much more significant than for the ground state, leading to additional homogeneous broadening of optical transitions. In conjunction with velocity-changing collisions, this can result in undesirable modifications of the atomic-spin response, especially in the presence of multiple excited states [162].

The second approach is to use a hydrocarbon antirelaxation coating for the inner cell walls, which is applied during cell production. The science of antirelaxation coatings for atomic vapor cells has actually been described in the literature as "black magic". This is because the details of how the coating works are not fully understood, and the coating process does not necessarily yield reproducible results in cell performance. Hence, for mass production of commercial systems, buffer-gas cells are typically preferred (Table 2.1) At the time of writing, there are no commercially available anti-relaxation coated vapor cells, although such cells are used in some commercially available magnetometers [163].

The process of alkali-atom relaxation on paraffin surfaces was modeled quantitatively, based on experimental work, already in the 1960s [65]. Some relevant qualitative points are the following. Atoms do not scatter elastically off the coated surface, but rather spent a finite time in the coating. For temperatures in the range 20–60°C, this is an adsorption process. (Adsorption is the process whereby molecules adhere to a surface; in absorption, they are taken up by a volume.) Spin relaxation takes place primarily at the walls and not in the cell body, as supported by the fact that the relaxation times scale with the cell dimensions [164].

Antirelaxation coatings are conventionally based on paraffin, also known as alkane (C_nH_{2n+2}). In recent years, coatings based on alkene (C_nH_{2n}) have also shown promise. An important parameter is the number of atom-wall collisions (bounces) that the coating can sustain before the atomic spins depolarize: on order 10^4 polarization-preserving bounces for paraffin and 10^6 for alkene [165]. Although the interaction of alkali atoms with alkene surfaces has not been studied in detail, it appears that the performance enhancement is related to carbon double bonds which are present in alkene but absent in paraffin [3]. However, paraffin coatings tend to offer better performance operation above room temperature [146]. In the SERF regime, buffer-gas cells are the only viable choice. Further details regarding production of various coated-cell types may be found in [166, 167], and specific considerations of optical pumping in coated cells are treated in [148].

2.5.4 Magnetometer operation

Further technical details of setting up an atomic magnetometer in the lab may vary greatly depending on the operating mode (Sec. 2.4)—see, e.g. [168]. Regardless of the specific design, however, one usually needs to go through the following general steps:

1. Align the vapor cell and all optomechanics with respect to the laser beam(s).

2. Lock each laser to the correct frequency.

3. Prepare the atomic spins via optical pumping, and allow them to evolve in the presence of the magnetic field to be measured.
4. Scan the magnetic resonance to obtain the magnetometer signal in frequency space (Fig. 2.4).
5. Tuning to resonance, for example via phase-locking techniques, enables tracking changes in the magnetic field as a function of time.

As mentioned previously, the linewidth of the magnetic resonance in step 4 is proportional to the transverse coherence rate $1/T_2$, so in principle one may be able to extract the T_2 value directly from the magnetometer signal. However, the strength of optical fields affects this linewidth, so the most precise T_2 measurements are usually conducted using a pulsed pump/probe regime whereby a free-induction-decay (FID) signal can be obtained. Another common approach to finding the T_2 time is to measure power-broadened resonance linewidths and extrapolate to zero laser power [66]. Whether or not such an investigation is necessary or desirable is context-dependent; for many applications it suffices to perform characterization of magnetometer time-series data as discussed in Sec. 2.6. However, linewidth measurements can be an important tool for noise characterization (Sec. 2.3.1), as various noise sources—including magnetic-field gradients and anything else that couples to the atomic spins—manifest themselves as broadening mechanisms.

In terms of data acquisition, there is great freedom of choice as regards both hardware and software. Commercial data-acquisition (DAQ) systems are available with a corresponding price tag; lower-budget options may involve open-source software and inexpensive hardware such as a computer sound card [169]. When sampling an oscillating signal, care should be taken to ensure that the sampling rate is fast enough to avoid aliasing effects.

2.6 Characterize and optimize your magnetometer

To illustrate how to analyze actual data, in 2.8.3 we provide magnetometer time-series data from [170], along with an accompanying analysis notebook. Although the data were obtained with a Hanle magnetometer, the illustrated analysis techniques are broadly applicable. The analysis is performed in Mathematica, but any other analysis program with similar capabilities can be used instead.

Measurement of magnetic signals in the time domain may be interesting and useful in itself, especially in the case of transient and/or triggered signals such as those encountered in biological applications. However, to characterize magnetometer performance as per the figures of merit introduced in Sec. 2.3, it is generally more instructive to work in the frequency domain. This is usually done by applying a fast Fourier transform (FFT) to the time-series data, in order to produce a frequency spectrum.

Figure 2.7 illustrates this analysis process for the case where no magnetic signal is present, such that the intrinsic magnetometer noise can be characterized. Looking at the

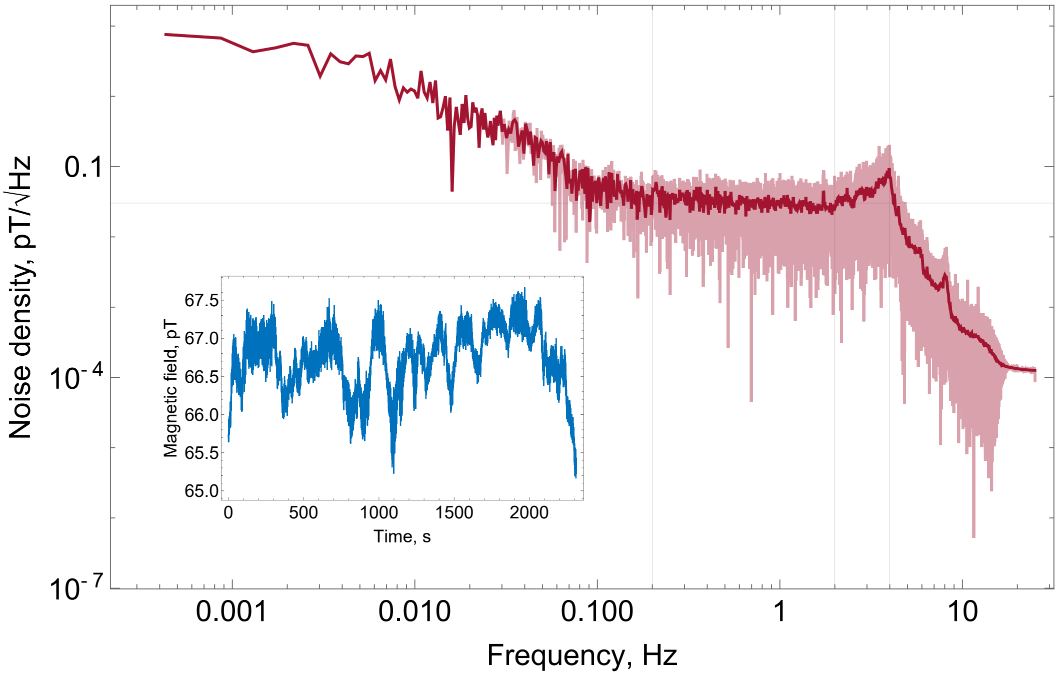

Figure 2.7: Noise-density frequency spectrum obtained by applying a fast Fourier transform (FFT) to raw magnetometer time-series data (inset) from [170]. The dark-red and light-red curves show the results with and without averaging, respectively. Vertical lines separate frequency regions dominated by different noise behavior, as explained in the text; the horizontal line indicates magnetometer sensitivity in the bandwidth of flat frequency response.

noise-density spectrum, we see that the noise behavior is highly frequency-dependent and can be characterized as follows:

- The noise is highest at lower frequencies, dominated by $1/f$ (so-called "pink" or "flicker") noise from background magnetic fields.
- Between 0.2 and 2 Hz, we have the flat or "white"-noise region of the spectrum. This region defines the useful bandwidth of the magnetometer and corresponds to a sensitivity of 30 $\mathrm{fT}/\sqrt{\mathrm{Hz}}$.
- The noise increases between 2 and 4 Hz, in this case due to an acoustic resonance of the magnetically shielded room in which measurements were conducted.
- Above 4 Hz, the magnetometer response drops off rapidly, here because of the low-pass filter of the lock-in amplifier used for data acquisition.

For purposes of characterizing magnetometer response, data may also be obtained by measuring known magnetic-field reference signals produced using a calibrated coil system—standard procedure for device optimization before any measurement of unknown fields is attempted. Peaks should then appear in the frequency spectrum corresponding to the frequencies of the applied fields; any peaks already appearing in the absence of applied fields are likely due to frequency-dependent noise sources.

Biomedical	magnetomyography (MMG) [155, 171], magnetoencephalography (MEG) [5, 89, 129, 130, 136, 172–176], (fetal) magnetocardiography (MCG and fMCG) [21, 22, 98, 128, 175, 177], magnetic-field imaging (MFI) [178] magnetic biomarkers [132, 179–182] biomagnetism of plants [183, 184] and livestock [185]
Zero-/low-field NMR	[133, 134, 149, 186–193]
Geophysics	[91, 194]
Aerospace	[108, 195]
Laser guide stars	[196]
Defense and industry	underwater surveillance [143], electromagnetic induction imaging [197–200]
Fundamental science	search for new physics beyond particle standard model [82, 201–204], with comagnetometry [34, 38–40, 72, 90] precision measurements [72, 203] *Quantum applications*: squeezing-enhanced magnetometers [55–58, 60, 61], quantum non-demolition measurements of atomic spins [95, 205], quantum information [206, 207], entanglement [62]

Table 2.3: Common applications of atomic magnetometers.

2.7 Typical applications of atomic magnetometers

In Table 2.3, we summarize the main current applications of atomic magnetometers. Not surprisingly, many of these diverse applications value high sensitivity and high accuracy at frequencies below tens of Hz. Non-invasive detection of biological magnetic signals is probably the most sought-after example, since such measurements can be carried out in a magnetically shielded environment to take maximum advantage of SERF magnetometers' exceptional sensitivity. Another important feature of atomic sensors is their negligible internal magnetic signature, making them desirable both for biomedical and surveillance applications. In summary, alkali-metal atomic magnetometers are admittedly still in their early steps toward widespread commercial success, and we may optimistically expect the emergence of new applications as fuller capabilities of atomic systems are explored in research laboratories.

2.8 Appendix

2.8.1 Optical pumping in cesium

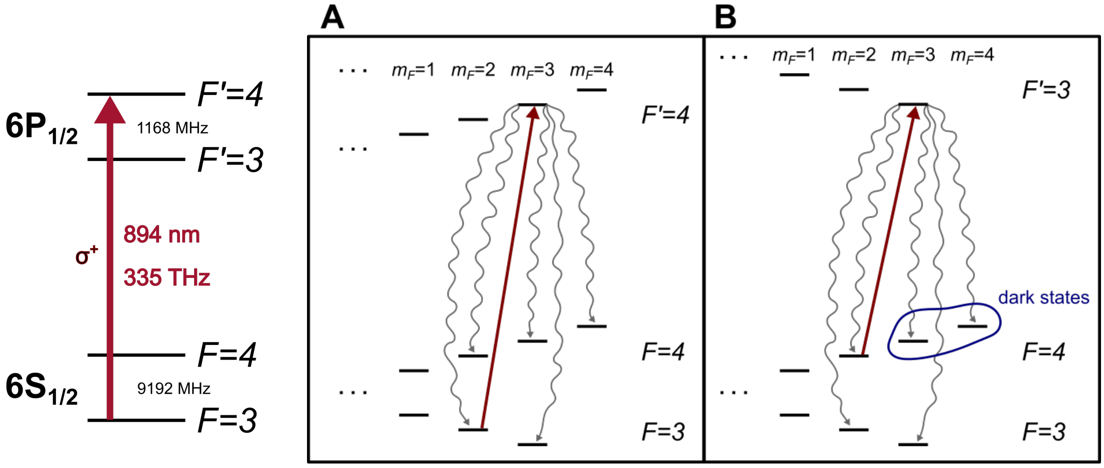

Figure 2.8: Example of optical pumping on the cesium D1 line (see Sec. 2.2 for notation and further details), illustrating one of the excitations and associated decay paths. Here we do not consider the possible presence of buffer gas, which may complicate the pumping process in an atomic vapor cell. **A)** Right-circularly polarized light tuned to the $F = 3 \longrightarrow F' = 4$ transition tends to pump the atom into the extreme hyperfine substate $F = 3$, $m_F = 3$. This particular transition is "leaky" because an excited atom may also decay to the $F = 4$ ground state. **B)** Pumping on the $F = 4 \longrightarrow F' = 3$ transition is preferred since it allows us to make use of the "dark states" $F = 4$, $m_F = 3$ and $m_F = 4$.

2.8.2 Sensitivity of an atomic magnetometer

How does the sensitivity of the magnetometer scale with the number of atoms N and the measurement time τ?

Here we choose $\hat{x}$ as atomic-spin polarization (pump) axis, $\hat{y}$ as magnetic-field direction, and $\hat{z}$ as probe direction, as shown in Fig. 2.9. This is a typical geometry for SERF magnetometers (Table 2.2), although the same derivation is possible for other operating modes.

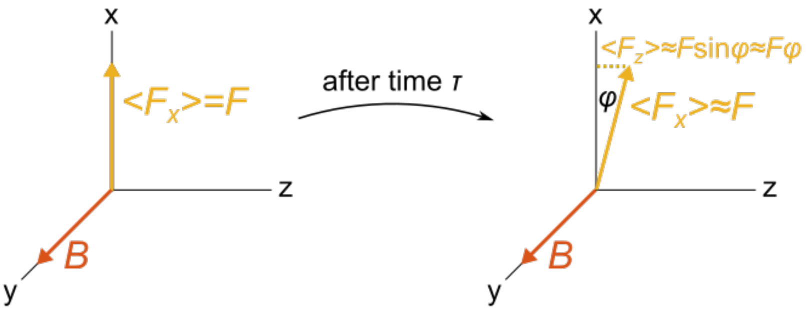

Figure 2.9: Spin evolution in an atomic magnetometer.

After polarizing an atom along $\hat{x}$, we want to measure the angular-momentum projection $m_F = F, F-1, ..., -F$ along $\hat{z}$ for some measurement duration τ. Meanwhile, the atomic spin is evolving under the influence of the external magnetic field $\vec{B}$ according to the Bloch equation (Sec. 2.2.2):

$$\frac{\mathrm{d}\vec{F}}{\mathrm{d}t} = \gamma\,\vec{B} \times \vec{F}\,. \tag{2.24}$$

The gyromagnetic ratio γ of the atomic system can also be expressed as $\gamma = g\,\mu_B/\hbar$, where g is the ground-state Landé factor and μ_B is the Bohr magneton. For simplicity, we initially assume a static magnetic field.

Treating the expectation value of the angular momentum as a classical vector, we find for the evolution of $\langle F_z \rangle$:

$$\frac{\mathrm{d}\,\langle F_z \rangle}{\mathrm{d}t} = -\gamma\,B\,\langle F_x \rangle\ . \tag{2.25}$$

Starting from $\langle F_z \rangle = 0$ because the atom is polarized along $\hat{x}$, and integrating over a small measurement time τ during which $\langle F_x \rangle$ can be considered constant (practically speaking, a time much less than the longitudinal spin-relaxation time T_1), we obtain

$$\langle F_z\,(\tau) \rangle = -\gamma\,B\,\langle F_x \rangle\,\tau\,. \tag{2.26}$$

Looking at Fig. 2.9, which shows the spin precession angle ϕ, we see that

$$\sin\phi \approx \langle F_z \rangle\,/\,\langle F_x \rangle \approx \phi\,. \tag{2.27}$$

Setting $F \approx \langle F_x \rangle \sim 1$ for an order-of-magnitude (for our example of cesium, we typically have $F = 4$), we end up with the following expression:

$$|\phi| \approx \gamma\,B\,\tau\,. \tag{2.28}$$

This spin precession may be detected via optical rotation or some other technique; in any case we assume that our magnetometer has 100% detection efficiency. (Note that for polarization-based detection, the angle of optical rotation of the probe light is proportional to ϕ.) Hence the uncertainty in B depends on the uncertainty in ϕ:

$$\delta B \approx \frac{\delta\phi}{\gamma\,\tau}\,. \tag{2.29}$$

The same result can also be derived for a magnetic field $\vec{B} = B\cos\left(\Omega t\right)\hat{y}$ oscillating at the Larmor frequency $\Omega = -\gamma B$. Then we find

$$\langle F_z\,(\tau) \rangle = -\gamma B\,\langle F_x \rangle\,\frac{\sin\left(\Omega\tau\right)}{\Omega}\,. \tag{2.30}$$

Taking $F \sim 1$ as before and noting that typically $\Omega\tau \ll 1$, we arrive again at Eq. (2.28).

If we are limited only by the quantum noise of the atom (spin-projection noise, Sec. 2.3.1), $\delta\phi$ is fundamentally set by the Heisenberg uncertainty relation:

$$\Delta F_y\,\Delta F_z \geq \frac{\langle F_x \rangle}{2}\,, \tag{2.31}$$

or, assuming minimum uncertainty $\Delta F_y = \Delta F_z$,

$$\Delta F_z = \sqrt{\frac{\langle F_x \rangle}{2}} \approx \sqrt{\frac{F}{2}} \sim 1\,. \tag{2.32}$$

We also have

$$\Delta F_z \approx F\,\delta\phi \sim \delta\phi\,, \tag{2.33}$$

such that we find an uncertainty (standard deviation) in the precession angle of order 1 rad, i.e. $\delta\phi \sim 1$. So Eq. (2.29) becomes

$$\delta B \approx \frac{1}{\gamma\,\tau}\,. \tag{2.34}$$

Basic statistics tells us that if we perform the same measurement on N independent atoms, the total measurement uncertainty (standard error) improves by $\sqrt{N}$. Similarly, if we repeatedly perform measurements of duration τ for a total time t, we gain another factor of $\sqrt{t/\tau}$. Thus we arrive at the total sensitivity

$$\delta B_{\mathrm{PN}} = \delta B \frac{1}{\sqrt{N}} \frac{1}{\sqrt{t/\tau}} \approx \frac{1}{\gamma} \frac{1}{\sqrt{N\,\tau\,t}} = \frac{\hbar}{g\,\mu_B} \frac{1}{\sqrt{N\,\tau\,t}}\,. \tag{2.35}$$

Although we would like τ to be as long as possible, in reality this time is limited by the coherence time T_2 of the atomic ensemble, and therefore

$$\delta B_{\mathrm{PN}} \approx \frac{\hbar}{g\,\mu_B} \frac{1}{\sqrt{N\,T_2\,t}}\,. \tag{2.36}$$

2.8.3 Data-analysis example

The data file and accompanying Mathematica analysis notebook used to produce the results in Sec. 2.6 are available online in the published version of this article (open access): DOI:10.1088/1367-2630/acb840.

Author contributions[5]

A.F. organized the tutorial and all authors share full responsibility for its content. While there was much overlap of efforts, primary leadership of individual sections was distributed as follows. A.F.: 2.1, 2.2.2, 2.2.5, 2.3, 2.5, 2.8. I.N.: 2.4, 2.7. G.B.: 2.2.1, 2.2.3–2.2.4, 2.6.

Acknowledgments

We thank our many colleagues from the Workshop on Optically Pumped Magnetometers (WOPM) for their generous support and assistance throughout the writing process, in particular Theo Scholtes. A.F. thanks Danila Barskiy, Dmitry Budker, Pavel Fadeev, Till Lenz, and Hendrik Bekker for helpful discussion and editing. Some portions of the text were adapted from [208].

---

[5] This section does not appear in the published version of the manuscript.

Chapter 3

Action potentials induce biomagnetic fields in carnivorous Venus flytrap plants

> The secrets are in the plants. To elicit them you have to love them enough.
>
> ---
>
> George Washington Carver, as quoted in *The Secret Life of Plants*

Scientific Reports **11**, 1438 (2021), DOI:10.1038/s41598-021-81114-w.

Anne Fabricant[1,2], Geoffrey Z. Iwata[1,2], Sönke Scherzer[3], Lykourgos Bougas[1,2], Katharina Rolfs[4], Anna Jodko-Władińska[4,5], Jens Voigt[4], Rainer Hedrich[3], and Dmitry Budker[1,2,6]

[1] *Institute of Physics, Johannes Gutenberg University of Mainz, Germany*
[2] *Helmholtz Institute Mainz, GSI Helmholtzzentrum für Schwerionenforschung, Darmstadt, Germany*
[3] *Department of Molecular Plant Physiology and Biophysics, University of Würzburg, Germany*
[4] *Physikalisch-Technische Bundesanstalt, Berlin, Germany*
[5] *Faculty of Mechatronics, Warsaw University of Technology, Poland*
[6] *Department of Physics, University of California, Berkeley, USA*

Upon stimulation, plants elicit electrical signals that can travel within a cellular network analogous to the animal nervous system. It is well-known that in the human brain, voltage changes in certain regions result from concerted electrical activity which, in the form of action potentials (APs), travels within nerve-cell arrays. Electro- and magnetophysiological techniques like electroencephalography, magnetoencephalography, and magnetic resonance imaging are used to record this activity and to diagnose disorders. Here we demonstrate that APs in a multicellular plant system produce measurable magnetic fields. Using atomic

optically pumped magnetometers, biomagnetism associated with electrical activity in the carnivorous Venus flytrap, *Dionaea muscipula*, was recorded. Action potentials were induced by heat stimulation and detected both electrically and magnetically. Furthermore, the thermal properties of ion channels underlying the AP were studied. Beyond proof of principle, our findings pave the way to understanding the molecular basis of biomagnetism in living plants. In the future, magnetometry may be used to study long-distance electrical signaling in a variety of plant species, and to develop noninvasive diagnostics of plant stress and disease.

3.1 Introduction

In the plant kingdom, electrical signaling pathways are involved in reception and transduction of external stimuli such as light [209], temperature [210], touch [211, 212], wounding [213], and chemicals [214]. Although human and animal magnetophysiology are well-developed areas of research [24, 155, 215–221], very little analogous work has been conducted in the plant kingdom [183, 209, 213, 222]. Our research aims to help establish magnetic sensing as a viable complement to traditional plant-electrophysiological techniques [223].

The bilobed trap of the *Dionaea muscipula* plant [212, 224] (Fig. 3.1A,B), formed by the modified upper part of the leaf, snaps closed within a fraction of a second when touched. Three trigger hairs that serve as mechanosensors are equally spaced on each lobe. When a prey insect touches a trigger hair, an AP (Fig. 3.1C) is generated and travels along both trap lobes [225]. If a second touch-induced AP is fired within 30 s, the viscoelastic energy stored in the open trap is released and the capture organ closes [226, 227], imprisoning the animal food stock for digestion of a nutrient-rich meal. The leaf stalk, or petiole, is not excitable and is electrically insulated from the trap [228]. Because of this, the trap can be isolated functionally intact from the plant by a cut through the petiole. On the isolated trap, stimuli trigger APs and closure just as on the intact plant. For the comfort of electrophysiological studies, one of the trap lobes can be fixed to a support while the other is removed, without affecting the features of AP firing. It has been shown that this simplified experimental flytrap system is well-suited to study the AP under highly reproducible conditions [229]. Other than by touch (mechanical energy), APs in traps can be induced by salt loads (osmotic energy) [230] and temperature changes (thermal energy).

Since mechanical activation of APs can cause unwanted noise in electric and magnetic recordings, we use thermal stimulation in our experiments. The interdisciplinary work presented here encompasses two complementary sets of experiments: the temperature dependence of flytrap electrical activity was studied in a plant-physiology laboratory, while magnetometer measurements of heat-stimulated traps were conducted in a magnetically shielded room.

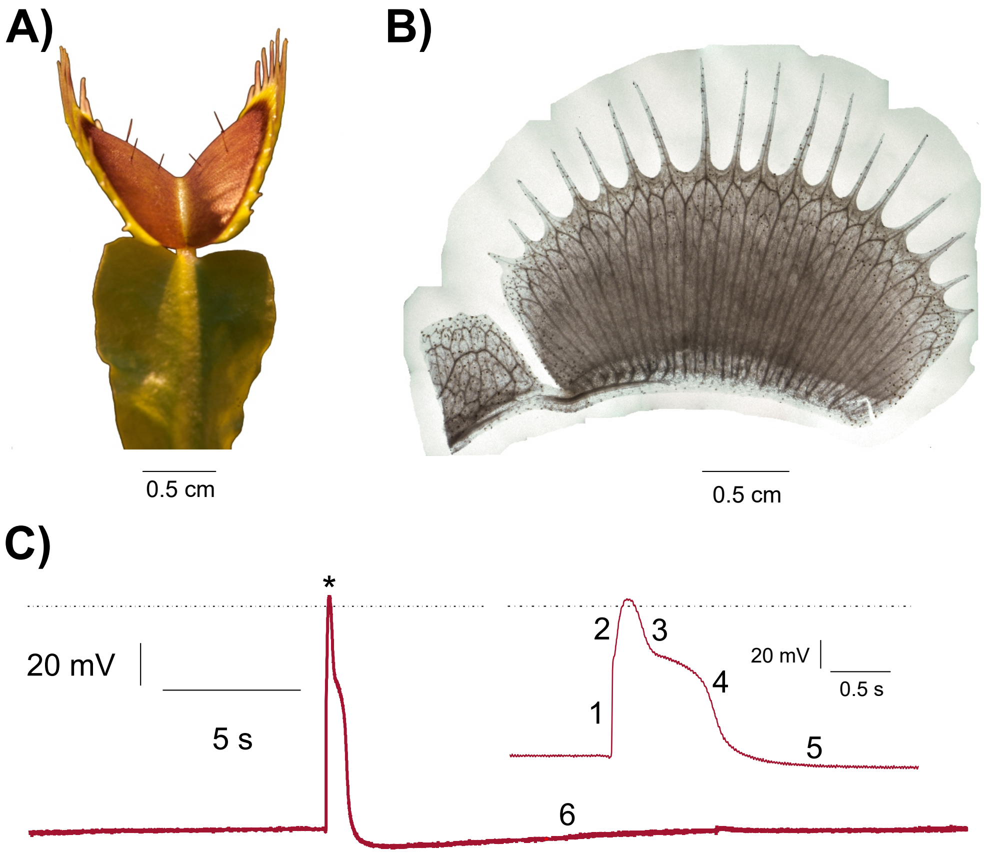

Figure 3.1: Venus flytrap geometry and action potentials. **A)** *Dionaea muscipula* leaf forms into a bivalved snap trap connected to the leaf stalk, or petiole. **B)** Side view of a destained trap lobe showing vasculature structure. In contrast to the petiole, the trap contains parallel veins of interconnected cells. These veins consist of both dead low-conductivity water pipes (xylem) and living conductive phloem. Here the trap was destained using a modified protocol according to [231], as described in Sec. 3.5. **C)** Intracellular AP lasting 2 s is subdivided into six phases (numbers), as explained in the text. The depolarization peak is indicated by an asterisk; the dotted line represents 0 mV. Inset: zoom-in on the AP, resolving the first five phases of the AP.

3.2 Heat-induced action potentials

When we heated up the support to which excised open traps were fixed, APs were elicited and the traps closed (Fig. 3.6 and Movie S1 [online]). To study the temperature dependence of heat-induced AP initiation (Fig. 3.2A), from a resting temperature of 20 °C, the trap temperature was increased monotonically to 45 °C at a rate of 4 °C/s (Fig. 3.7). Below 30 °C, no APs were observed; above 30 °C, the probability of AP firing increased and was maximal (100%) above 40 °C. In 60 independent experiments using 10 different traps from 10 different plants, we recorded the temperature at which an AP was first induced. When these data were plotted as temperature-dependent AP-firing probability (Fig. 3.2B), the curve could be well-fitted by a single Boltzmann equation characterized by a 50% AP-firing probability at 33.8 °C. This behavior indicates that heat activation of the AP is based on a two-state process. The ion channels that carry the classical animal-type AP also occupy two major states: closed and open. In contrast to the animal sodium-based AP, the plant AP

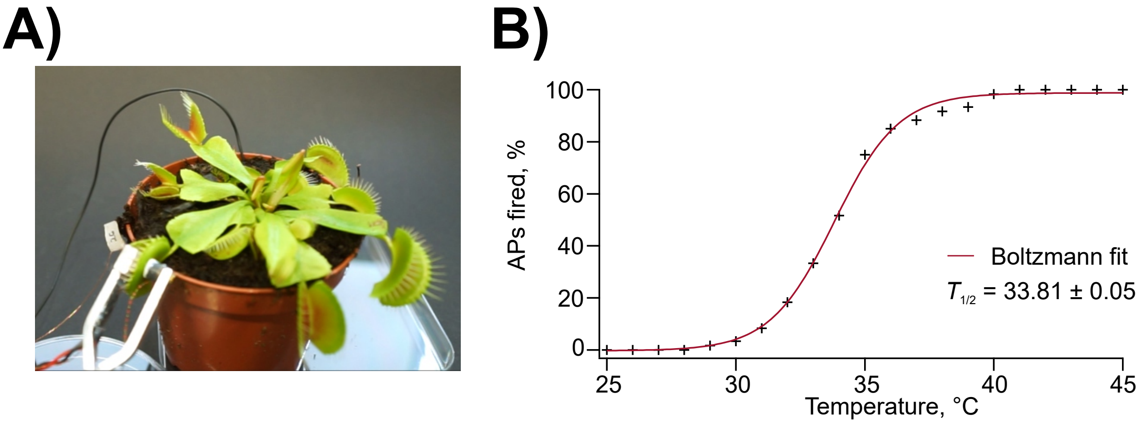

Figure 3.2: Electrical measurements of heat-induced action potentials. **A)** *Dionaea* plant with clamp mounted on one lobe of a trap, equipped with a Peltier device and surface-voltage electrode. A ground electrode is placed in the soil surrounding the plant root. **B)** Temperature dependence of AP-firing probability fitted by a Boltzmann equation (red curve), characterized by 50% firing probability at temperature $T_{1/2}$.

depolarization is operated by a calcium-activated anion channel [212]. Thus, we conclude that the temperature "switch" of the *Dionaea* AP is based on a calcium-dependent process. Following Ca^{2+} binding, the anion-channel gates open. Our experiments indicate that at temperatures of $T \lessapprox 34\,°C$ the cellular Ca^{2+} level remains below threshold, but at $T \gtrapprox 34\,°C$ there is enough chemical energy to open a critical number of anion channels, driving the fast depolarization phase of the AP.

The *Dionaea* AP can be subdivided into six well-defined phases (Fig. 3.1C): 1) fast depolarization, 2) slow depolarization, 3) fast repolarization, 4) slow repolarization, 5) transient hyperpolarization, and 6) slow recovery of the membrane potential to the pre-AP state. When comparing APs recorded at different temperatures, we found that temperature affects the signal amplitude and duration. Increasing the thermal energy input changed not only the probability for an AP to be fired, but also led to an increased AP amplitude and decreased half-depolarization time (3.6). These facts indicate that heat-sensitive ion channels trigger and shape the AP: at higher temperatures, thermal energy input causes more closed Ca^{2+}-activated anion channels to open and depolarize the membrane potential. Compared to depolarization, fast repolarization (mediated by K^+ channels) and transient hyperpolarization (caused by depolarization activation of outward-directed protein pumps) were much less affected by temperature. The recovery time to reach the resting membrane potential was essentially insensitive to temperature changes.

Besides lowering the AP firing threshold and changing certain features of the AP, prolonged heat stimulation can induce trap lobes to enter an autonomous AP firing mode (Fig. 3.6). When increasing the bottom surface temperature of the recording-chamber base from 20 to 46 °C, AP spiking activity sets in after a couple of seconds, reaching a steady AP firing frequency of 3.8 per minute at a stable 46 °C surface temperature. Induction of autonomous APs has also been obtained using flytraps treated with NaCl salt (osmotic energy) [232].

3.3 Biomagnetism

Having established heat stimulation as a reliable noninvasive technique for inducing flytrap APs, we searched for the magnetic field associated with this electrical excitability. Magnetometry experiments were carried out at Physikalisch-Technische Bundesanstalt (PTB) Berlin in the Berlin Magnetically Shielded Room 2 (BMSR-2) facility [233], using four QuSpin Zero-Field Magnetometers (QZFM). These commercial optically pumped magnetometers (OPMs) employ a glass cell containing alkali vapor to sense changes in the local magnetic-field environment [1, 125]. A magnetically shielded environment is required for operation of these magnetometers, and use of a walk-in shielded room allowed for the constant presence of an experimenter to prepare plant samples and carry out measurements. As shown in Fig. 3.3, an isolated trap lobe was attached to the housing of the primary sensor (denoted A), such that the distance between the plant sample and the center of the atomic sensing volume was approximately 7 mm. Two secondary sensors (B and C) were placed nearby the primary sensor to measure signal fall-off, and an additional background sensor (D) was used to monitor the magnetic environment in the shielded room. Each magnetometer is sensitive to signals along two orthogonal axes. Resistive heaters in the magnetometer housing, which are used to increase the atomic density and improve sensitivity, also served to induce autonomous AP firing via surface heat transfer at 41°C. To monitor heat-induced APs, we used two silver-tipped copper surface electrodes, inserted in either end of the plant sample [234]. Prior to the measurements, we performed tests to ensure that no spurious magnetic fields were generated by the electrode system (Figs. 3.8–3.6.3). The magnetic and electric data, together with other auxiliary trigger signals, were sampled simultaneously using the same data-acquisition system located outside the MSR.

To better distinguish possible magnetic signals from background noise, we triggered on the electric signals and averaged the magnetic data in a time window around those trigger points. Examples of averaged magnetic data are shown in Fig. 3.4. A clear magnetic signal with a time scale corresponding to that of the averaged electric signal is visible in the primary-sensor data. For comparison, data from several different experiments were plotted (Fig. 3.5). To minimize common background noise, we subtracted the magnetic data of sensor D to create a gradiometer with a 48 mm baseline. Signals of up to 0.5 pT are visible in the y-axis gradiometric data, normal to the sample surface. The signal magnitude obtained is comparable to what one observes in surface measurements of nerve impulses in animals [155].

To quantify the significance of the measured signals, signal-to-noise ratios (SNR) were calculated from the average y-axis gradiometric time traces as follows. The noise level is defined as the standard deviation of the gradiometric response in a 1.5 s time window (from time $t = -2$ s to $t = -0.5$ s in Fig. 3.4A) prior to signal onset. The signal size is defined as the amplitude of the extreme (minimum) field value, with respect to the mean value in the noise window. For the four experiments shown in Fig. 3.5, the SNR ranges from 8 to 20. The corresponding p-values are $p < 9 \times 10^{-16}$, indicating that the probability

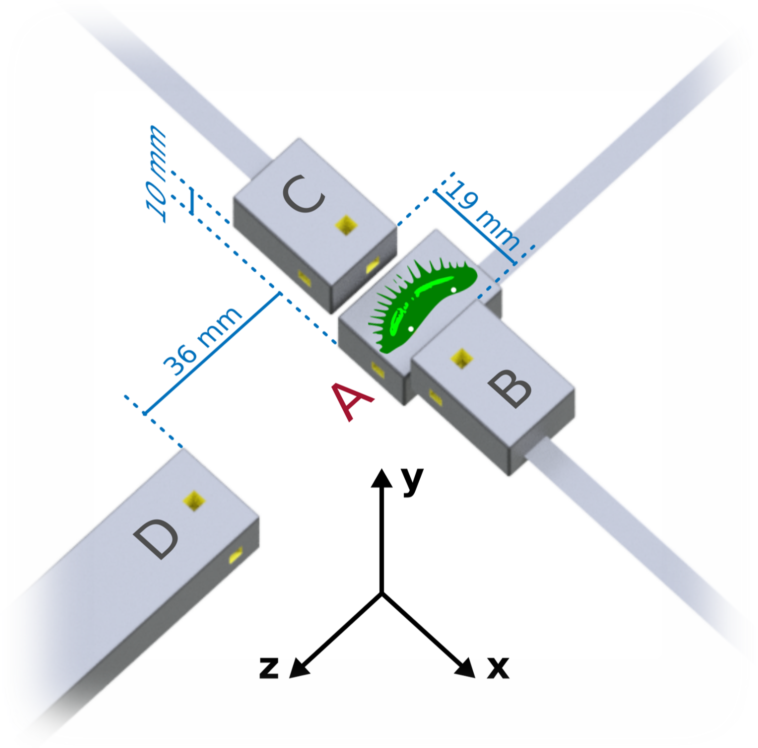

Figure 3.3: Schematic of the experimental setup in the magnetically shielded room (MSR). The plant sample, an isolated lobe of the flytrap, is placed on top of primary sensor A, in the x–z plane with trigger hairs exposed. For reference, the dimensions of the housing (gray boxes) for the primary and secondary sensors are $24.4 \times 16.6 \times 12.4\,\mathrm{mm}^3$. Yellow cut-outs indicate the position of the $3 \times 3 \times 3\,\mathrm{mm}^3$ atomic sensing volume. A 3D-printed ABS plastic structure (not shown) holds the magnetometers in position on a wooden table. White dots on the plant sample, approximately 1 cm apart, indicate the placement of surface electrodes for AP monitoring. In the coordinate system shown, all magnetometers are sensitive along the y-axis, normal to the surface of the plant sample; furthermore, A and D are sensitive along the z-axis, and B and C are sensitive along the x-axis. Sensors B and C are positioned symmetrically around sensor A. Sensor D serves as a background sensor and is therefore located farther away from the sample.

of such signals arising from random noise is negligible. At the sub-Hz signal frequency, the sensitivity of the gradiometer is approximately $100\,\mathrm{fT}/\sqrt{\mathrm{Hz}}$ (Fig. 3.11). For both the electric and magnetic signals, the full width at half extremum (maximum or minimum, FWHM) were also calculated, where the extremum is defined with respect to the mean value in the noise window.

The temporal superposition of the electric and magnetic signals in Fig. 3.5 suggests that we have detected the magnetic activity associated with the flytrap AP. Unlike in measurements of animal nerve axons and the large internodal cells of *Chara corallina* alga, where the magnetic field is proportional to the time derivative of the intracellular voltage [221–223], the magnetic signal from the complex multicellular flytrap lobe has a shape similar to that of the electric signal. We see features in the magnetic signal which appear to correspond to the depolarization and repolarization phases of the AP. In electric recordings using surface electrodes, the exact shape and duration of signals are dependent on the placement of electrodes on the measured sample. By contrast, magnetometry records

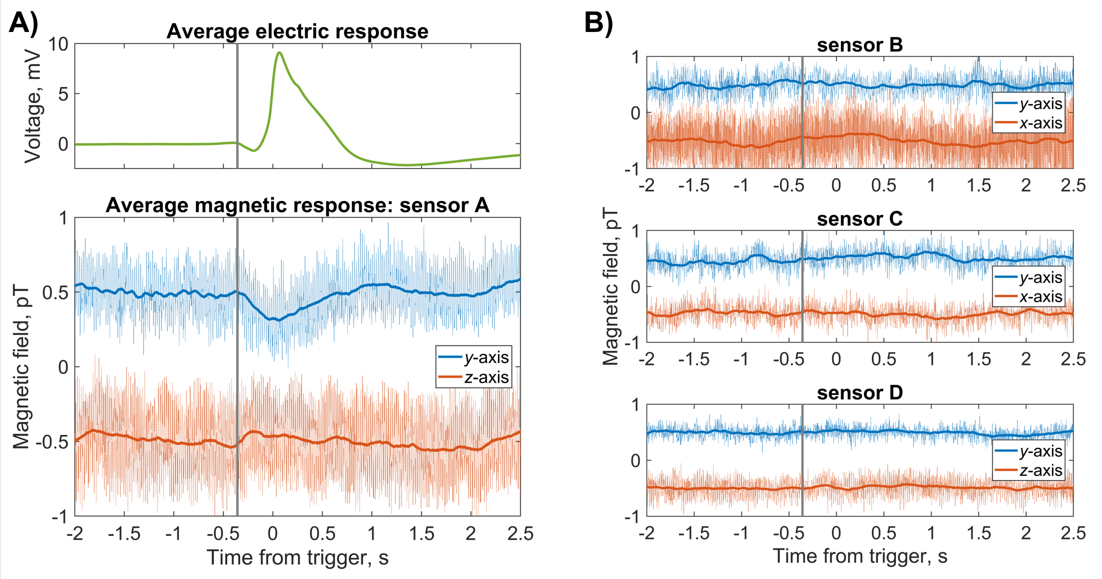

Figure 3.4: Average action potential and corresponding magnetic signals. **A)** Result of triggering on nine consecutive APs from a trap lobe heated to 41°C, then averaging the electric and magnetic data from a 4.5 s window around each trigger point. The average magnetic traces (bottom graph, opaque traces) were frequency-filtered (50 Hz low-pass), then smoothed with a 0.2 s running average. A magnetic signal is visible in both sensitive axes of the primary sensor A. For comparison, the raw unfiltered data are plotted behind the processed data. For visual clarity, DC offsets have been added to the data, and vertical gray dotted lines indicate the approximate start time of the electric signal. **B)** Average magnetic response from the other three sensors, obtained using the same procedure as in **A)**. The data from the secondary sensors, B and C, do not show a signal. The data from the background sensor D can be used to remove noise common to all sensors (see Figure 3.5).

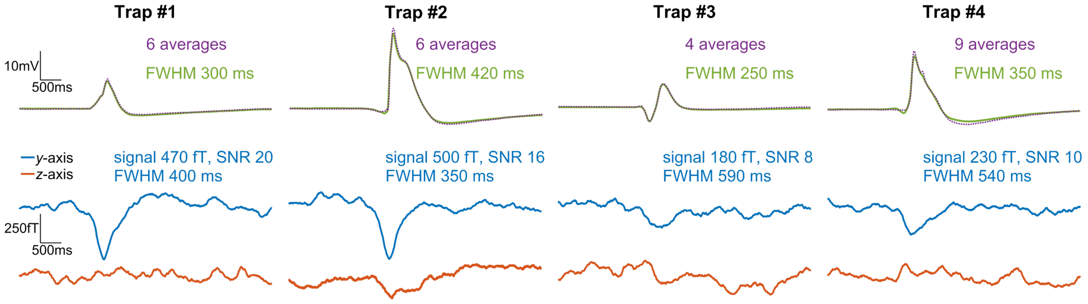

Figure 3.5: Comparison of average electric and gradiometric signals from four different experiments. In each case we triggered on heat-induced APs in the electric trace and performed the same data analysis as for Fig. 3.4. The electric response recorded by the surface electrodes (top row; average signal plotted as solid green, single AP plotted as dashed purple) varies in amplitude because a different plant sample was used in each experiment. To produce the gradiometric plots (bottom graphs) we subtracted the magnetic data of background sensor D from that of primary sensor A. The number of averages in each experiment is indicated, along with the amplitude and signal-to-noise ratio (SNR) of the y-axis gradiometric signal. The rightmost panel (Trap #4) shows the same data set as in Fig. 3.4.

a "true" physical signal from the organism. In this sense, it is comparable to intracellular electrode techniques. Whereas intracellular electrodes are sensitive to electrical activity of single cells, magnetometers can record both local and systemic activity at the multicellular level. In this way, magnetometry might be considered a complementary tool to the emerging technique of gene-based imaging of plant electrical signaling [228, 235].

The physical origin of the measured biomagnetic fields is related to an outstanding question in plant electrophysiology: how electrical signals propagate over long distances through the plant. Essentially this is a scaling problem: while electrical signaling is well-understood in some unicellular plant systems [222], much less is known about the propagation mechanisms of such signals between cells and along cellular pathways. For the Venus flytrap system, it is known from electrode measurements that APs propagate through the trap at speeds of around 10 m/s [224].[1] A proposed pathway of long-distance signal propagation between plant cells in the trap is the electrically conductive phloem in the vasculature (Fig. 3.1B). Given that the typical resistance between two points on a trap is $R \approx 1\,\mathrm{M\Omega}$ [237], we can perform a basic calculation to confirm that the magnitude of the magnetic fields we measure is reasonable. We estimate the expected magnetic-field magnitude at the center of the sensing volume to be

$$B \approx \frac{\mu_0 I}{2\pi r}\,, \tag{3.1}$$

where $I = V/R \approx 10\,\mathrm{nA}$ is the current passing through the trap between the electrodes, and $r \approx 7\,\mathrm{mm}$ is the perpendicular distance from the trap surface. Using these values, we find $B \approx 0.3\,\mathrm{pT}$, a magnitude which corresponds well with the y-axis experimental results of sensor A. Although the precise distribution and directionality of current flow in the trap is unknown, we can use the geometry of the trap (Fig. 3.1A,B) and magnetometry setup (Fig. 3.3) to further interpret our results. If the x-oriented parallel-cable structure of the vasculature is the primary conduction pathway, magnetic field along the y-direction is expected at the primary sensor A, but not at the secondary sensors B and C. The symmetry of the trap about the x-direction could explain the relative lack of z-axis magnetic signal in our measurements. Thus, our magnetometry results agree with a hypothesis that the vasculature serves as a network for long-distance electromagnetic signaling within the trap.

3.4 Discussion

Previously reported detection of plant biomagnetism, which established the existence of measurable magnetic activity in the plant kingdom, was carried out using superconducting-quantum-interference-device (SQUID) magnetometers [209, 213, 222]. Atomic magnetometers are arguably more attractive for biological applications, since, unlike SQUIDs [238, 239], they are noncryogenic and can be miniaturized to optimize spatial resolution of measured biological features [24, 155, 240]. In the future, the SNR of magnetic measurements in

---

[1] This value is now thought to be too large, with adjusted estimates placing the speed of AP propagation in the range 2–10 cm/s ([236] and personal communication with S. Scherzer, May 2021).

plants will benefit from optimizing the low-frequency stability and sensitivity of atomic magnetometers. Just as noninvasive magnetic techniques have become essential tools for medical diagnostics of the human brain and body, this noninvasive technique could also be useful in the future for crop-plant diagnostics—by measuring the electromagnetic response of plants facing such challenges as sudden temperature change, herbivore attack, and chemical exposure.

3.5 Methods

Biology

To obtain strong electric and magnetic signals, the health of the plants is paramount. We purchased adult Venus flytraps from a carnivorous-plant greenhouse (Gartenbau Weilbrenner, Freinsheim, Germany). Normally the plant samples were housed in a growth chamber manufactured by Poly Klima. The plants are kept on an automated 12/12 h light/dark cycle at approximately 25°C and 75% relative humidity, treated only with distilled water. To keep the flytraps alive during the PTB measurement run, we used homemade plastic greenhouses equipped with plant-cultivation lighting and temperature and humidity monitoring.

To produce the destained image of the flytrap lobe shown in Fig. 3.1B, the trap chlorophyll was removed using methanol at 37°C for 4 weeks, followed by final clearing in 4% sodium dodecyl sulfate (SDS) for 4 weeks.

For recording of flytrap APs in our heat-stimulation investigations, we used surface electrodes measuring the extracellular potential of a trap. The measuring electrode (blank silver wire; 0.25 mm, WPI, Sarasota, USA) was inserted into the trap, with the electrical connection enhanced by application of a droplet of contact gel (Laboklinika), while the reference electrode was inserted into wet soil or the petiole midrib. Electrical signals were amplified 100-fold and recorded with Patchmaster software (HEKA). Temperature dependence of AP induction was studied by application of a homemade Peltier device powered by a PTC-10 temperature-control system (npi electronic, NJ 08510, United States). Constant heat was applied using an IKA RET basic hot plate (IKA-Werke GmbH & Co. KG, Staufen, Germany) heated to 46°C.

Magnetometry

Several types of magnetometry experiments were conducted at PTB: controls, OPM measurements using four QuSpin sensors (three Gen-2: denoted A, B, C; one Gen-1.5: denoted D), and measurements using the multichannel SQUID array of BMSR-2. See Sec. 3.6 for further details of the SQUID measurements.

For the OPM measurements of isolated trap lobes, each sample was cleaved from the plant with a razor blade and placed on the primary sensor A for immediate measurement. The sample was either secured to the sensor housing with double-sided adhesive tape (acrylate, thickness 0.5 mm) or placed on a plastic slide (PET, thickness 0.22 mm) on the

Figure 3.6: Spontaneous AP firing on a hot plate heated to 46 °C. Surface-potential measurements confirming that heat evokes APs. Corresponds to Movie S1 [online], showing trap closure on the hot plate.

housing. Electrode, magnetometer, and electric reference signals were recorded at a 500 Hz acquisition rate on a 9-channel analog data-acquisition system with PC control. The raw difference signal from the two surface electrodes was first sent through a voltage preamplifier (Stanford Research Systems, Model SR560), AC-coupled with a gain of 100. It is essential to use a voltage, rather than current, preamplifier to avoid currents in the electrical leads whose magnetic fields may be detected by the magnetometers. Since leakage of electrical signals into magnetic channels is a serious concern, we address the topic in detail in Sec. 3.6.

3.6 Appendix

3.6.1 Heat stimulation

As part of our study of heat-induced flytrap electrical behavior (Figs. 3.6–3.7, we compared the amplitude and depolarization kinetics of APs recorded at 10, 20, 30, and 40°C. There was a 1.6-fold increase in AP amplitude from 10 to 40°C. When heating the trap from 10 to 30°C, the half-depolarization time dropped from 0.29 ± 0.08 s to 0.13 ± 0.02 s.

3.6.2 SQUID measurements

In the PTB data run, as a complement to the OPM measurements we also conducted two types of experiments using 57 channels of the BMSR-2 built-in SQUID array. The first type involved placing an intact flytrap plant directly under the SQUID dewar, whose bottom surface has a 2.8 cm offset from the plane of the pick-up coils. We closed each trap in turn by two consecutive mechanical stimulations of the trigger hairs with a plastic pipette tip. In the data analysis, we looked for signals in the magnetic data corresponding to either the APs or subsequent trap closure. Even after averaging multiple SQUID channels, no signals were found, probably because of the large distance between sample and sensors. In the second type of SQUID experiment, we attached an isolated trap lobe directly to the bottom of the dewar and performed mechanical stimulation, but again no magnetic signals were found during data analysis. Following the calculation in the main body of the paper, at offset distance of at least 2.8 cm from the sample we would reasonably expect a magnetic-field magnitude on the order of 10 fT. Since this is approximately the noise floor

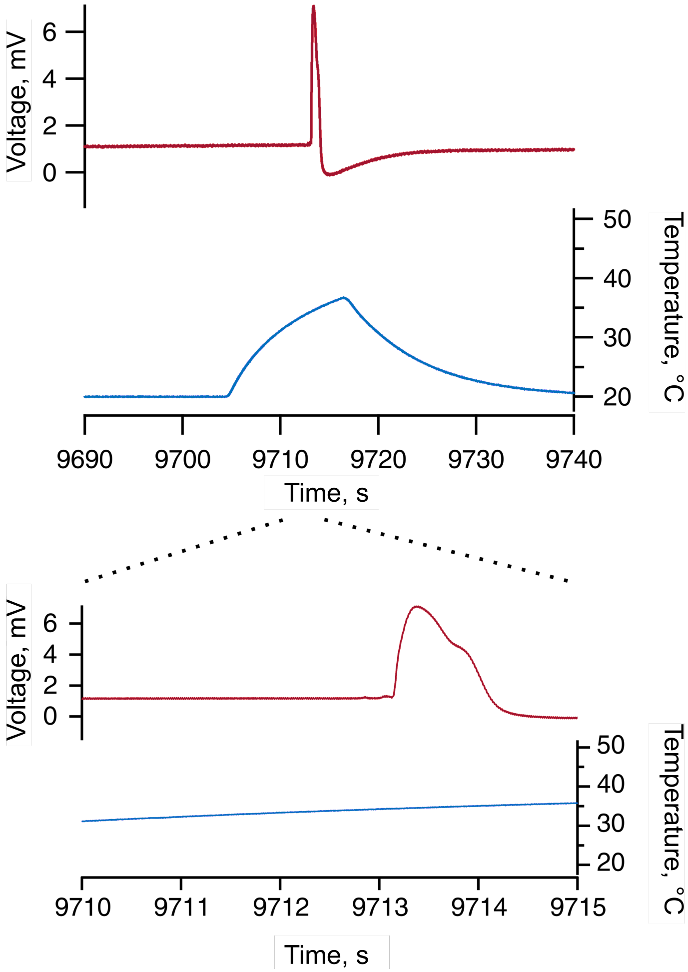

Figure 3.7: Comparison of measured surface potential and applied temperature. Heat was applied via a Peltier element placed on the inner trap surface. An AP (red curve) occurred as the temperature (blue curve) increased from 20 to 45 °C. The lower graph is a zoom-in on the time axis to define the temperature at which the AP occurred.

of the SQUID magnetometer system at 1 Hz (under ideal operating conditions), the null result is consistent with expectations.

3.6.3 Electrode tests

Prior to the data run, we tested the electrode system to ensure that no spurious magnetic fields due to currents in the electrode wires would be picked up by the magnetometers under usual experimental conditions. These tests were conducted using the circuit depicted in Fig. 3.8, with a four-layer MS-2 magnetic shield from Twinleaf containing two active QuSpin sensors (B and C) placed side-by-side. A function generator (Tektronix AFG2021) in parallel with a resistor created a sawtooth “artificial flytrap action potential” signal at 1.2 Hz. This signal was sent through a low-noise voltage preamplifier (SRS Model SR560) with typical experimental settings (6 dB low-pass 10 Hz filter, AC coupling, gain 1000, input impedance 100 MΩ) that yielded a preamplifier output of amplitude 2 V—corresponding to the output amplitude we would see in an actual flytrap experiment. The crucial step

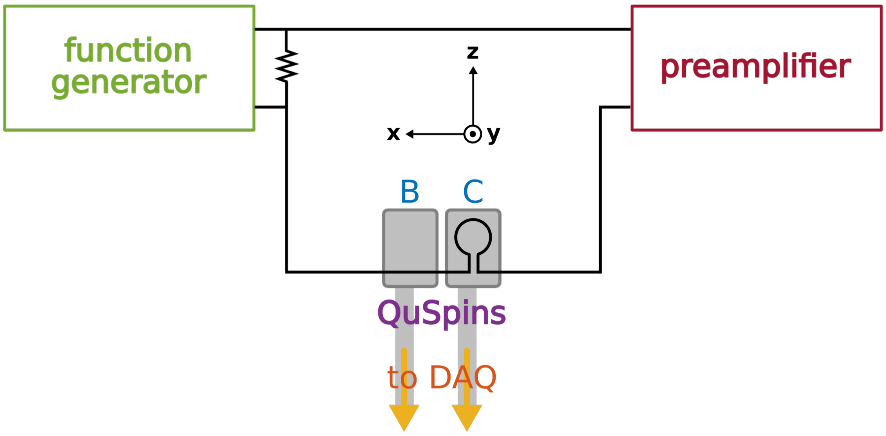

Figure 3.8: Circuit for testing the preamplifiers. See text for details.

was to simulate a "worst-case scenario" for the electrode wires. To that end, a 1 cm copper coil, in series with the preamplifier, was placed directly on top of sensor C. As is evident in Fig. 3.6.3, no signal at 1.2 Hz was visible in the y-axis or z-axis data of either magnetometer. Even when we increased the amplitude of the electric signal by five times (corresponding to 10 V preamplifier output), no signal at 1.2 Hz was observed. Thus, we were satisfied that the electrode/voltage-preamplifier system was not a source of unwanted noise. The voltage preamplifier and electronics used in these diagnostic experiments were the same as those used in BMSR-2 for plant experiments.

For comparison, we also conducted identical tests with a low-noise current preamplifier (SRS Model SR570, 6 dB low-pass 10 Hz filter, sensitivity 100 nA/V). In this case the signal at 1.2 Hz did appear above the noise in the data of sensor C. For example, the 2 V experiment yielded a 3 pT signal along the y-axis, indicating that a current of over 20 nA was flowing in the current loop. Based on these results, we exclusively used the voltage preamplifier in our data run at PTB. As an additional security check, in all OPM experiments we ran one of the electrode wires over the background sensor D to monitor for possible spurious signals (none were detected).

3.6.4 OPM data

Figure 3.10 shows the electric time traces used in the data analysis for Figs. 3.4 and 3.5. The recorded APs are slightly variable in shape and exhibit certain artifacts, which is normal for surface-electrode measurements. In some time traces (e.g. Fig. 3.10) we observed the frequency of autonomous AP firing increasing over time, which may be explained as follows. Sufficient input energy is required to increase the cytosolic calcium level to threshold—once this threshold is reached, an AP is released. As the trap heats up in our setup, the stored cellular energy increases while the new energy which needs to be input for the next AP decreases, which could lead to an increase in AP firing frequency.

To characterize the performance of the QuSpin gradiometer system in the shielded room, we recorded the background in the room and performed frequency analysis. A typical noise

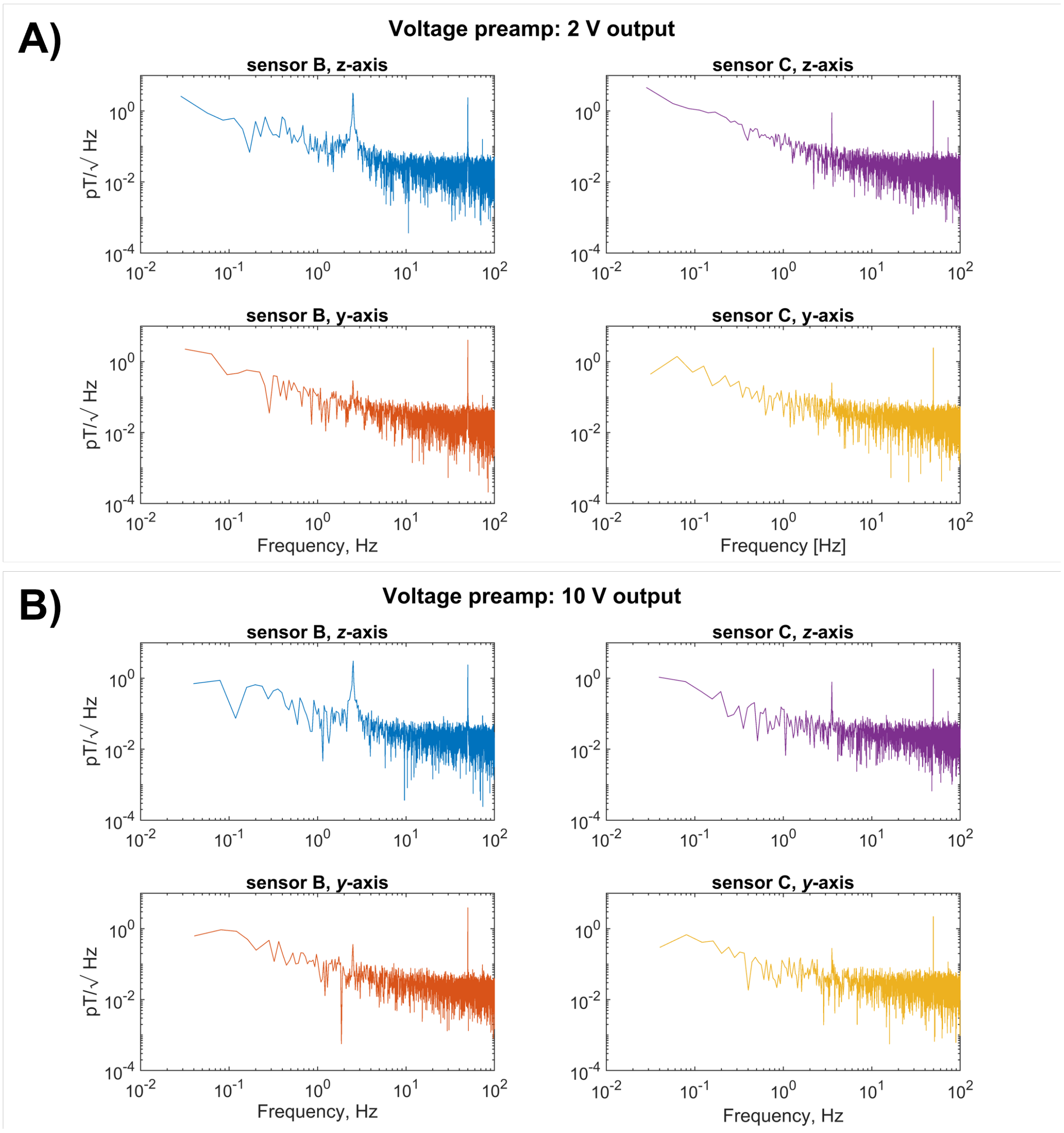

spectrum is shown in Fig. 3.11.

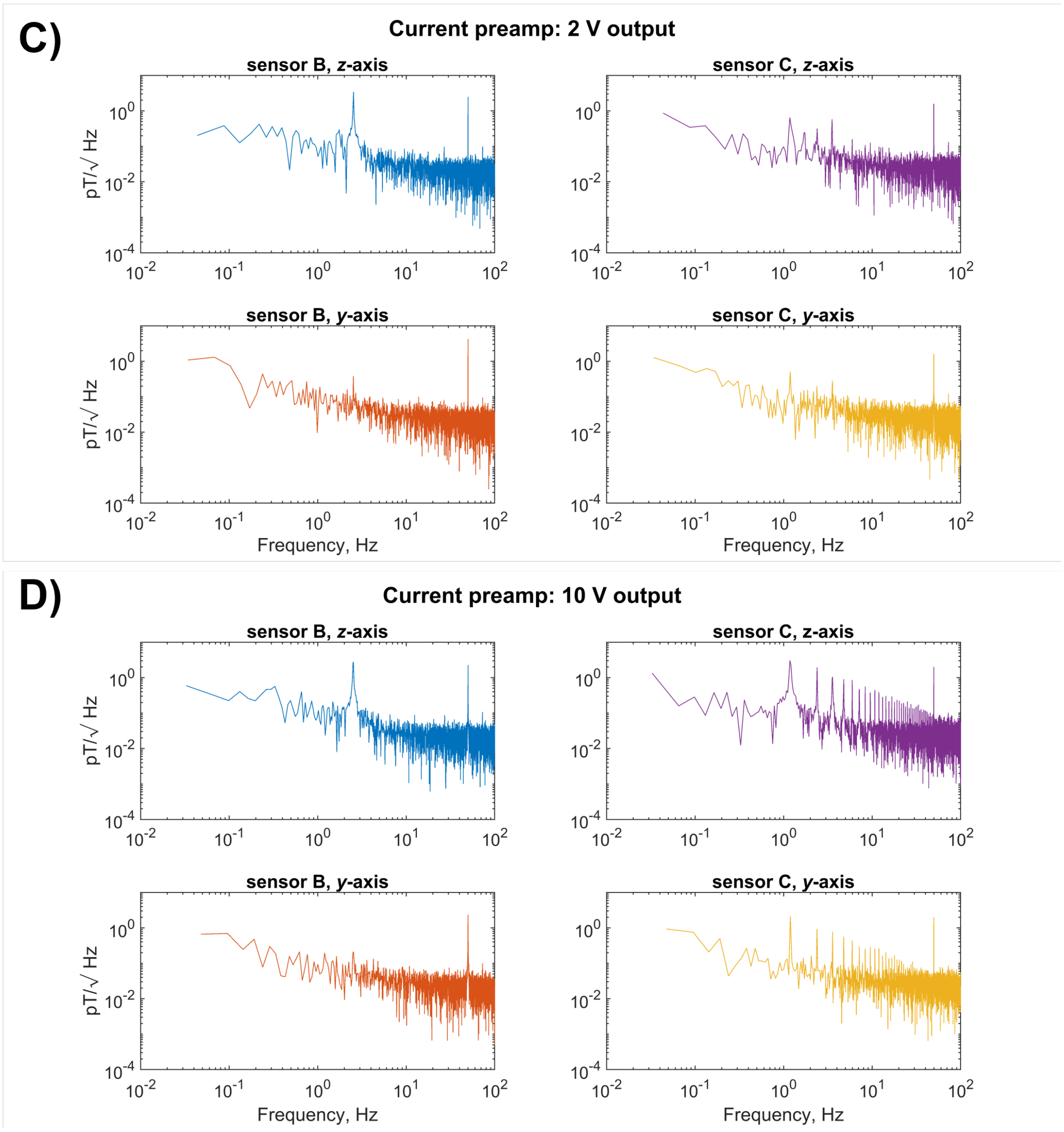

Figure 3.9: Results of the preamplifier tests. In addition to the 50 Hz line frequency, peaks due to lab background noise appear at 2.5 and 3.5 Hz. Signal from the current preamplifier appears in the data of sensor C (panels **C)** and **D)**), but this effect is not seen when the voltage preamplifier is used (panels **A)** and **B)**).

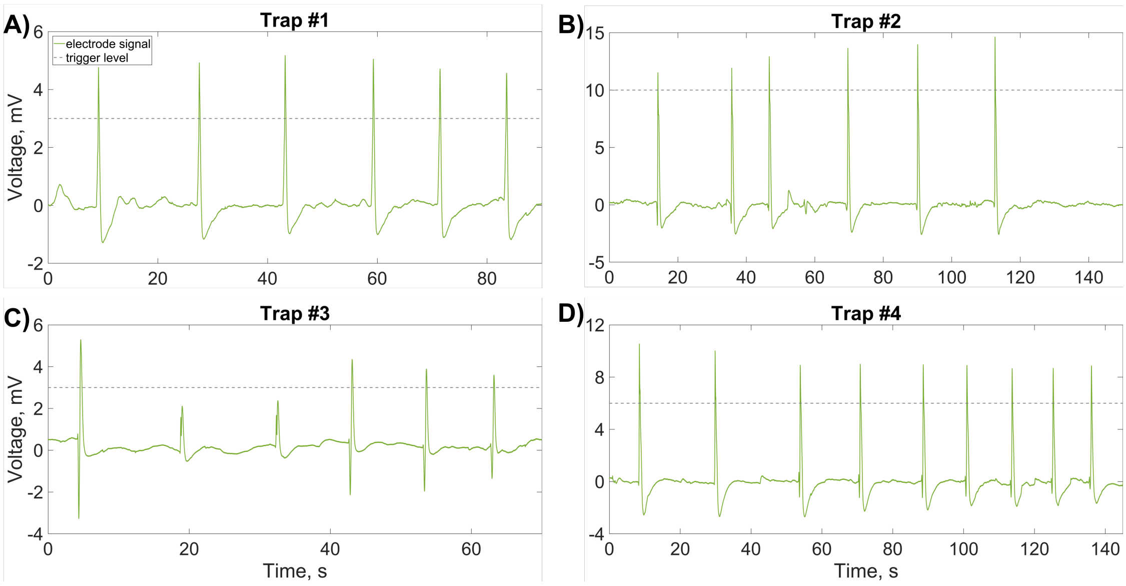

Figure 3.10: Electric time traces showing heat-induced action potentials. Data were recorded from four separate experiments (panels **A)**–**D)**) with different plant samples, corresponding to the data shown in Fig. 3.5. The APs are used as a trigger so that we can perform averaging of the simultaneous magnetic data; the trigger level is indicated by the gray dashed line.

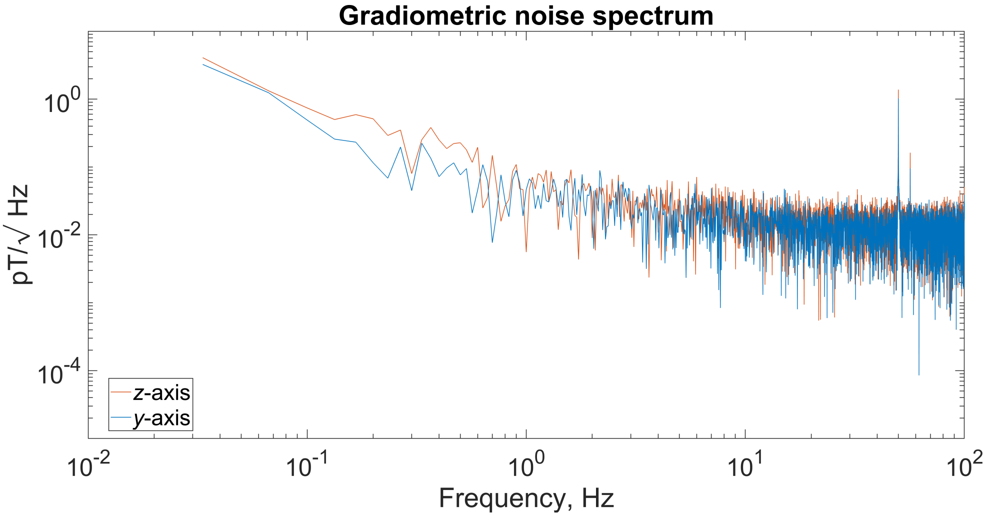

Figure 3.11: Typical noise floor of the gradiometer in the MSR. Obtained by recording a 30 s time trace prior to the start of an experiment.

Author contributions

A.F. and D.B. proposed to study biomagnetism in the Venus flytrap. A.F., G.I., S.S., L.B., K.R., A.J.W., and J.V. conducted experiments. A.F. and S.S. analyzed data. A.F., R.H., and S.S. wrote the manuscript. R.H., D.B., G.I., L.B., S.S., J.V., A.J.W., and K.R. edited the manuscript. D.B. and R.H. supervised research.

Acknowledgments

Dr. Tilmann Sander-Thömmes and Sophia Haude assisted during the PTB data run. Dr. Rob Roelfsema of the University of Würzburg provided valuable guidance in the early stages of the project. Dr. Andreas Trabesinger and Pavel Fadeev offered helpful comments on the manuscript. We acknowledge the support of the Core Facility "Metrology of Ultra-Low Magnetic Fields" at the Physikalisch-Technische Bundesanstalt, which receives funding from the Deutsche Forschungsgemeinschaft (DFG KO 5321/3-1 and TR 408/11-1). A.F. was supported by a Carl-Zeiss-Stiftung graduate fellowship. This research was supported in part by the German Federal Ministry of Education and Research (BMBF) within the Quantumtechnologien program (FKZ 13N14439), as well as the DFG Koselleck award HE 1640/42-1 to R.H.

Chapter 4

Proton relaxometry of tree leaves at hypogeomagnetic fields

> My life now is just trees, isn't it.
> Trees and, um, champagne.
>
> Dame Judi Dench

Frontiers in Plant Science **15**, 1352282 (2024), DOI:10.3389/fpls.2024.1352282.

Anne M. Fabricant[1,2], Piotr Put[3], and Danila A. Barskiy[1,2]

[1]*Institute of Physics, Johannes Gutenberg University of Mainz, Germany*
[2]*Helmholtz Institute Mainz, GSI Helmholtzzentrum für Schwerionenforschung, Darmstadt, Germany*
[3]*Faculty of Physics, Astronomy and Applied Computer Science, Jagiellonian University in Kraków, Poland*

We report on a cross-species proton-relaxometry study in *ex vivo* tree leaves using nuclear magnetic resonance (NMR) at 7 μT. Apart from the intrinsic interest of probing nuclear-spin relaxation in biological tissues at magnetic fields below Earth field, our setup enables comparative analysis of plant water dynamics without the use of expensive commercial spectrometers. In this work, we focus on leaves from common Eurasian evergreen and deciduous tree families: Pinaceae (pine, spruce), Taxaceae (yew), Betulaceae (hazel), Prunus (cherry), and Fagaceae (beech, oak). Using a nondestructive protocol, we measure their effective proton T_2 relaxation times as well as track the evolution of water content associated with leaf dehydration. Newly developed "gradiometric quadrature" detection and data-processing techniques are applied in order to increase the signal-to-noise ratio (SNR) of the relatively weak measured signals. We find that while measured relaxation times do not vary significantly among tree genera, they tend to increase as leaves dehydrate. Such experimental modalities may have particular relevance for future drought-stress research in ecology, agriculture, and space exploration.

4.1 Introduction

The essential problem of measuring water content and dynamics in plants may seem simple enough. To this day, however, the water-monitoring toolbox remains surprisingly limited, especially where nondestructive techniques are concerned. A standard approach involves desiccating harvested plant organs and comparing their fresh and dry weights [241–244]. In recent years, proton (^{1}H) nuclear magnetic resonance (NMR) has emerged as a promising alternative technique, due to its sensitivity to water protons. ^{1}H NMR has found a number of plant-related applications—including measurement of water content in lumber wood [245], investigation of moisture stress in agricultural seeds [246, 247], and characterization of microbial interactions in soil [248]. Techniques based on proton relaxometry are now particularly relevant within food science [249–251], where magnetic resonance imaging (MRI) is also employed [252]. However, commercially available NMR spectrometers typically do not have suitable geometries for measurement of intact plants or plant organs.

Leaves are arguably the most critical actor in the plant water cycle, given that a majority of transpiration and systemic water loss occurs there. Despite this, the use of proton NMR in leaf water studies is far from mainstream, although some relaxometry work has been carried out with low-field benchtop spectrometers. Notably, relaxometry of senescing rapeseed leaf pieces (excised discs) at 20 MHz was investigated using a Carr-Purcell-Meiboom-Gill (CPMG) protocol, indicating an increase in some T_2 (spin-spin relaxation time, also known as coherence time) components in older leaves [253, 254]. A similar study at 20 MHz demonstrated the utility of T_2 relaxation for phenotyping and detection of water stress in excised leaves of young potted tobacco plants [255]. At high field, proton T_2 relaxometry was applied to structural water studies in maple leaves [256]. In addition, high-field solid-state proton NMR was shown to be effective for studying relaxation properties of dried leaves and leaf litter even when little water is present, by revealing the molecular fingerprint of plant metabolites and biopolymers [257].

The flexibility and portability of low-field NMR—loosely defined as corresponding to magnetic fields ranging from Earth field up to a few tesla, above which superconducting or hybrid superconducting/electromagnets would be required—also offers potential for taking devices directly into the field, forest, or greenhouse. One major example is the realization of *in vivo* and *ex vivo* water-proton relaxometry of intact leaves from potted agricultural plants, as well as wild shrubs and oak and poplar trees, using a unilateral 18 MHz spectrometer [258]. Currently, noncommercial low-field relaxometers are being developed which enable portable *in vivo* measurement of even larger plant leaves and organs [259]. Such devices complement other novel non-NMR modalities for nondestructive monitoring of leaf water potentials, e.g. nanobiosensors [260]. In trees, water transport in living tree trunks and branches has been studied using custom low-field MRI and NMR devices [261, 262].

In traditional NMR systems based on inductive detection, the tradeoff between portability and achievable signal-to-noise ratio (SNR) limits how low of a magnetic field can be reasonably used for measurement of intact biological systems, where signal strengths tend to be relatively weak. It has been shown theoretically that below proton resonance frequencies of around 50 MHz, detection using atomic (optically pumped) magnetometers can offer better intrinsic sensitivity than that attainable with inductive pickup coils [263]. The atomic-magnetometry detection modality has been instrumental in the subfield of zero-to-ultralow-field (ZULF) NMR [133, 134, 186, 188, 264],[1] where ULF is commonly used in literature to refer to fields below the geomagnetic (Earth) field of tens of microtesla, such that magnetic shielding or active field cancellation is required. Due to varying definitions of ULF by different authors, some absolute [265] and others referenced to the spin system under study—e.g., J-coupling between spins dominates Zeeman interactions with the external field [266]—we choose instead to use the unambiguous term "hypogeomagnetic" in this publication. The hypogeomagnetic regime has already been used for direct detection of biomagnetic fields produced by plant electrical activity, including action potentials and wounding potentials [184, 213, 222]; however, according to our understanding, NMR signals originating from plants have not yet been explored in this regime.

In addition to the fundamental question of how proton relaxation properties behave at hypogeomagnetic fields, the regime is interesting from a practical NMR standpoint, due to the low cost, portability, and low energy consumption of experimental components. Although NMR detection using superconducting-quantum-interference-device (SQUID) magnetometers [265, 267] offers comparable sensitivity to atomic magnetometers at hypogeomagnetic fields (as well as a larger frequency bandwidth), the need for bulky cryogenic cooling limits the applicability of SQUID-based devices. The smaller footprint of atomic magnetometers also allows placement of multiple sensors around a sample, rather than in a single detection plane.

To our knowledge, the work reported here represents the broadest cross-species NMR-relaxation study of tree leaves at any magnetic field, and the first to incorporate both evergreen and deciduous varieties. Through systematic nondestructive measurement of intact leaves from seven different tree genera—spruce, pine, yew, hazel, cherry, beech, and oak—we endeavored to investigate variation in water-proton signals and relaxation times among genera. In targeted studies of spruce and oak samples, we also sought to track the evolution of these parameters as a function of leaf dehydration. While relative proton signal correlates with wet mass upon dehydration, T_2 times tend to increase, indicating the possible presence of compartmentalized water reservoirs with higher water mobility surviving upon dehydration. We note that leaves and other plant tissues contain pools of both free and bound water; our approach is expected to mainly target free and loosely bound water protons. More strongly bound water protons, such as those contained in cell walls, tend to have much shorter T_2 times which would require a targeted technique such

---

[1] Since publication of this manuscript, a new comprehensive review on ZULF NMR has become available (containing some data from the setup here presented): Danila A. Barskiy, John W. Blanchard, Dmitry Budker, James Eills, Szymon Pustelny, Kirill F. Sheberstov, Michael C. D. Tayler & Andreas H. Trabesinger, "Zero- to ultralow-field nuclear magnetic resonance", *arXiv* preprint (2024), submitted to *Progress in Nuclear Magnetic Resonance.*

as time-domain (TD) NMR to resolve [250, 259].

4.2 Materials and Methods

4.2.1 Relaxometry setup

Our gradiometric quadrature detection scheme is shown in Fig. 4.1A, where two commercially available dual-axis vector magnetometers [125] are placed orthogonally in the x-y plane. If the sensors, denoted 1 and 2, are positioned symmetrically around a magnetic dipole initialized along $-\hat{x}$ and undergoing Larmor precession clockwise in the plane at positive angular frequency ω_0,[2] we can write the following (ideal) expressions for the oscillating magnetic field sensed by the four magnetometer channels as a function of time t:

$$\begin{aligned} B_{x_1}(t) &= \mu_0\, m_0 \cdot \cos(\omega_0 t) \cdot e^{-t/T_2} / \left(4\pi r^3\right) \ , \\ B_{y_1}(t) &= \mu_0\, m_0 \cdot \sin(\omega_0 t) \cdot e^{-t/T_2} / \left(2\pi r^3\right) \ ; \qquad (4.1) \\ B_{x_2}(t) &= -\mu_0\, m_0 \cdot \cos(\omega_0 t) \cdot e^{-t/T_2} / \left(2\pi r^3\right) \ , \\ B_{y_2}(t) &= -\mu_0\, m_0 \cdot \sin(\omega_0 t) \cdot e^{-t/T_2} / \left(4\pi r^3\right) \ . \qquad (4.2) \end{aligned}$$

Here, r is the offset distance of the center of the sensing volumes from the magnetic dipole (the sample is modeled as a uniformly magnetized sphere); T_2 is the characteristic exponential decay time of the precession signal; μ_0 is the vacuum permeability constant. Note the factor-of-two difference between pairs of measured field components; this is the result of a dipole-field geometry as measured by point-like sensors. The initial magnetic-moment amplitude m_0 equals the sample volume times the magnetization of the sample. Note that each measured magnetic-field component may be positive or negative, since vector rather than scalar magnetometers are used. For a spherical 1 mL sample of water polarized at 1 T and room temperature (typically 22°C in our lab), one can estimate magnetic-field values (at the beginning of the measurement assuming no relaxation losses) on the order of 100 pT, given the experimental offset distance of 17.5 mm. This agrees with experimental data (Fig. 4.2); a complete calculation is provided in Section 4.5. We note that, fundamentally, Eqs. (4.1)–(4.2) should contain T_2^* rather than T_2, as we do not employ CPMG or other dynamic decoupling sequences to suppress effects of magnetic-field inhomogeneities at the position of the sample during measurement. However, because the studied leaf samples have intrinsically high relaxation rates (T_2 of 150–300 ms, see Section 4.3) which are larger than contributions due to inhomogeneity of the solenoid (Fig. 4.13), such simplification is warranted in our case.

We see from Eqs. (4.1)–(4.2) and the geometry in Fig. 4.1A that by subtracting the measured fields along the $\hat{x}$- and $\hat{y}$-axes, respectively, the signals along each axis add—leading to a signal enhancement of 1.5, assuming identical sensor response—while common-mode noise is canceled. Furthermore, the two gradiometric signals have a relative phase of

---

[2] In Ch 2, Larmor frequency was denoted Ω.

$\pi/2$—i.e., are in-quadrature—which becomes useful for signal processing in the frequency domain via Fourier transform. This is the basis of what we have termed the "gradiometric quadrature" detection scheme, used in the work reported here to achieve enhanced (by a factor of ∼3 compared to single-channel measurement) proton signals in *ex vivo* tree leaves.

The experimental setup, contained in a portable instrument rack, is depicted schematically in Fig. 4.1B. Thermal polarization of nuclear spins is created using a 1 T Halbach magnet with 15 mm bore, which defines the maximum possible diameter of measured samples. After adequate polarization-buildup time in the magnet (5–10 s), rapid (∼100 ms) mechanical shuttling of the sample into the magnetic shield (Twinleaf MS-1LF) is performed using an Arduino-controlled stepper motor driving a plastic gear rack, to which a nonmagnetic sample holder is attached. Shuttling occurs inside a double-layer piercing solenoid wrapped around a plexiglass tube and reaching from the top of the Halbach magnet through the magnetic shield. At the center of the shield, a 3D-printed frame of ABS plastic contains three pairs of Helmholtz coils (radius 33 mm) for creation of magnetic-field pulses along the x-, y-, or z-axes to manipulate the nuclear-spin state, as well as two atomic magnetometers (QuSpin QZFM Gen-2) for detection of nuclear-spin signals (Fig. 4.1A). These zero-field sensors can operate in ambient magnetic fields of up to tens of nT, which is readily achieved with the magnetic shield, with the aid of built-in compensation coils. We introduced the piercing solenoid specifically to be able to separate the background field on the sensors from the precession field on the sample. A field on the order of 10 µT may be generated inside the piercing solenoid without compromising sensor operation, as field leakage outside the solenoid is usually below 1%. The range of achievable precession frequencies is ultimately limited by sensor bandwidth—below 500 Hz for the atomic magnetometers used in this work.

Figure 4.1B shows the typical relaxometry protocol for the experiments reported here. After spin polarization and shuttling, immediate application of a $\pi/2$-pulse in the y-direction rotates the bulk z-magnetization into the x-axis, where it subsequently precesses about the leading z-field of amplitude B_0 at an angular frequency ω_0 given by the proton gyromagnetic ratio $\gamma_{^1\mathrm{H}}$ according to $\omega_0 = \gamma_{^1\mathrm{H}} B_0$, where $\gamma_{^1\mathrm{H}}/2\pi \approx 43\,\mathrm{Hz}/\mu\mathrm{T}$.[3] This Larmor precession gives rise to a free-induction-decay (FID) signal which is acquired by the magnetometers. For proton spins (positive sign of the gyromagnetic ratio), precession is "left-handed", occurring clockwise about the applied magnetic field [269].

Experimental timing and control as well as detector readout were implemented in Labview using NI TTL-pulse and data-acquisition cards. To maximize the SNR of the measured FID signal, a number of experimental parameters were iteratively optimized. These include: polarization time, solenoid field (proton precession frequency), shuttling time and speed/acceleration, pulse duration and amplitude, and acquisition time. Various calibration data, along with photos and further details of the apparatus, may be found in

---

[3] Note that we only consider the magnitude of ω_0 in this equation. However, the proper conventional expression for precession frequency is $\omega_0 = -\gamma_{^1\mathrm{H}} B_0$, where $\gamma_{^1\mathrm{H}} > 0$. Unlike in traditional NMR, quadrature-detected ZULF-NMR enables distinguishing signs of γ [268].

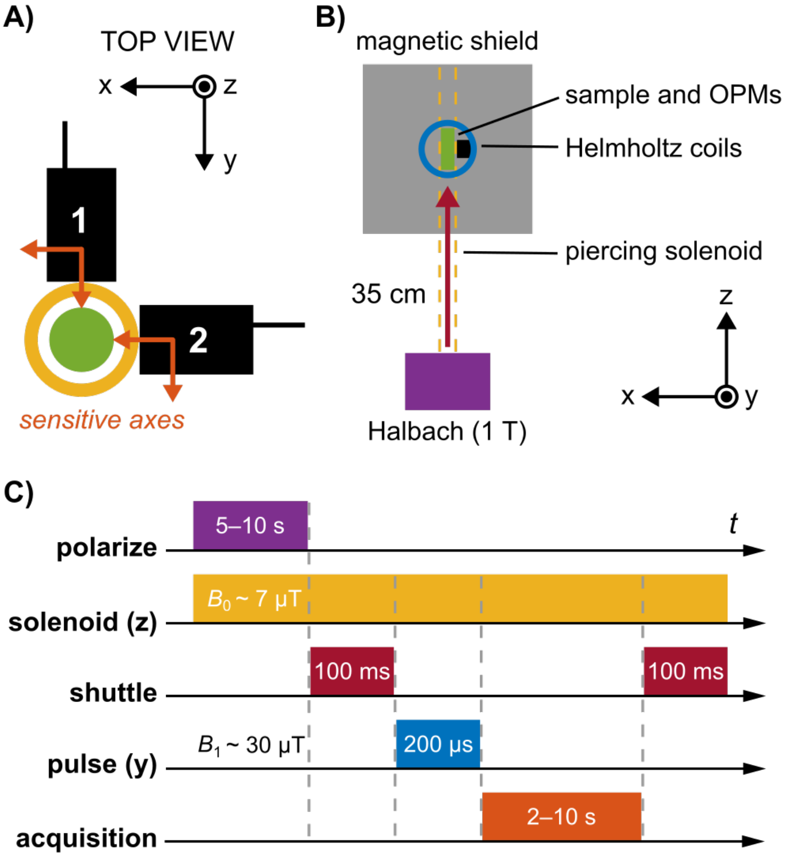

Figure 4.1: Schematic overview of the relaxometry experiment. **A)** A pair of magnetometers (QuSpin QZFM Gen-2; sensing volume $4 \times 4 \times 4\,\mathrm{mm}^3$, Rb vapor cell), each sensitive along two orthogonal axes indicated with orange arrows, are oriented in the x-y plane. The center of sensing volume is located 6.5 mm from the tip of the sensor housing (black boxes). Samples to be measured are enclosed in a 2 mL glass vial with outer diameter 11.6 mm (green circle), located in a plexiglass tube around which a solenoid is wound (yellow circle). The outer diameter of the solenoid is approximately 22 mm, so that the minimum offset distance of the sensing volume from the center of the sample is 17.5 mm. **B)** Nuclear spins are first thermally polarized in a 1 T permanent magnet (Halbach array) before being mechanically shuttled into a magnetically shielded environment. There, three orthogonal pairs of Helmholtz coils enable manipulation of the spin states via controlled application of magnetic-field pulses. The piercing solenoid is used both for guiding during shuttling and for generation of a tunable precession field inside the magnetic shield. **C)** The typical experimental protocol uses a guiding magnetic field of 7 µT inside the solenoid (proton precession frequency ~285 Hz). Polarization in the 1 T magnet lasted 5 s for leaf samples and 10 s for water calibration samples, followed by shuttling into the center of the magnetic shield within 100 ms. A 30 µT magnetic-field pulse was then immediately applied in order to rotate z-magnetization of the sample into the x-y plane ($\pi/2$ pulse), where subsequent free induction decay (FID) of the magnetization signal in the precession field was recorded by the magnetometers. Signal acquisition time was set to 2 s for leaf samples and 3–10 s for water calibration samples.

Section 4.5.

4.2.2 Data processing

During acquisition of an FID according to the protocol in Fig. 4.1B, the analog voltage outputs of all four magnetometer channels are recorded at a user-defined sampling rate, usually 2 kHz, for subsequent analysis. Although the sensors are always calibrated (i.e., ambient magnetic fields internally compensated) with the sample in the measurement position prior to each experiment, application of the magnetic-field pulse drives the sensors out of their sensitive range for some tens of milliseconds. Thus, initial data points must be discarded in post-processing, resulting in an effective linear phase shift of the recorded oscillating signal. Because each magnetometer channel provides a vector measurement—sensitive to the sign of the magnetic field, in contrast to a scalar sensor—the handedness of spin precession may be deduced from a single-channel time trace, if it is possible to reconstruct the true phase of the FID. However, the quadrature detection scheme allows us to determine the handedness without having to reconstruct the phase.

As an illustration of the analysis procedure, Fig. 4.2 shows calibration data from a liquid water sample at a proton precession frequency of 10 Hz, obtained by supplying a current of 54 μA to the piercing solenoid. The first 25 ms of data, corresponding to the first 50 points of the FID sampled at 2 kHz, have been discarded to remove post-pulse artifacts which would otherwise adversely affect the spectral lineshape and baseline (the calibrated magnetometers have a dynamic range of approximately 5 nT; the applied pulse of 30 μT prior to acquisition temporarily pushes them out of range). Plots show the average of multiple (here, four) scans, where a linear trend has been removed from each individual raw time trace prior to averaging. This detrending of time-domain signals mitigates the effect of low-frequency magnetic-field drifts in the lab environment, which may negatively impact spectral baselines in the frequency domain. Initially, we convert from voltage to magnetic-field units to obtain four time series associated with the four magnetometer channels, which we denote x_1, y_1, x_2, and y_2, following Eqs. (4.1)–(4.2). The two gradiometric channels are subsequently constructed as $x = x_1 - x_2$ and $y = y_1 - y_2$. By examining the single-channel and gradiometric time traces in the context of the detection geometry (Fig. 4.1A), we can confirm that the spin signal was initialized along $-\hat{x}$ and is precessing clockwise in the x-y plane, consistent with a precession field along $+\hat{z}$. Furthermore, reduction of noise via gradiometry is clearly visible.

The gradiometric-quadrature channel can be constructed from the two gradiometric channels as $x + iy$ (see Section 4.5 for more details). In our experimental geometry, the time-dependent quadrature signal may be thought of as a vector rotating clockwise in the complex plane defined by a real x-axis and imaginary y-axis. Assuming perfect quadrature geometry, when a standard Fourier transform is performed to convert the signal into the frequency domain, the resulting spectrum should contain a resonance only at +10 Hz and not at −10 Hz.

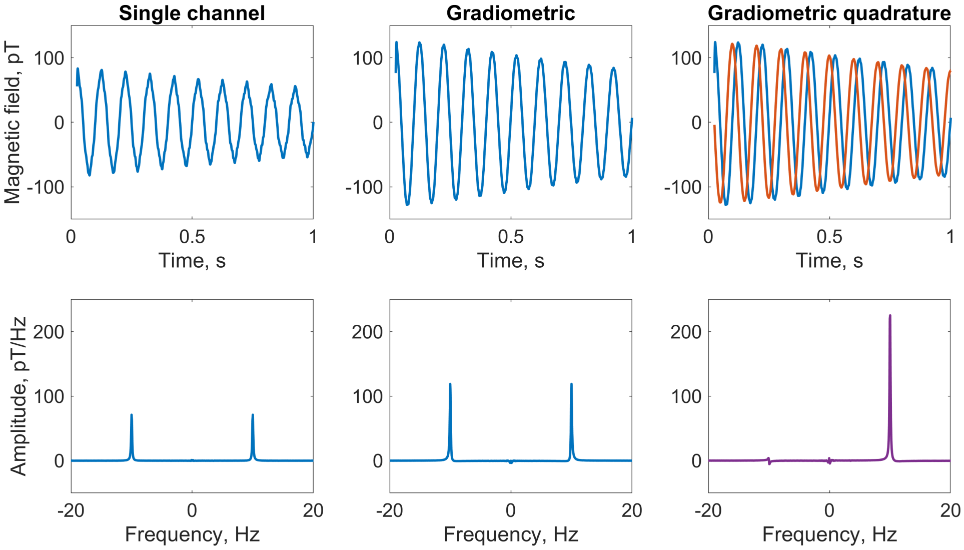

Figure 4.2: Comparison of water-proton NMR calibration spectra using three different detection modalities. A 1.5 mL vial of deionized water was measured using the detection geometry and relaxometry protocol depicted in Fig. 4.1, at a 230 nT (10 Hz) precession field. Plots show the average of four scans. Top row, left to right: first second of the free-induction-decay (FID) signal recorded by the y-channel of sensor 1; gradiometric FID signal (difference of signals from the y-channels of sensors 1 and 2), showing signal enhancement and noise suppression; overlaid x (red) and y (blue) gradiometric FID signals, which are summed in quadrature as described in the text. Bottom row: corresponding frequency spectra obtained by fast Fourier transform (FFT); the signal at +10 Hz is enhanced at least 2.5 times in the phased quadrature spectrum (rightmost panel) as compared to a phased single y-channel spectrum (leftmost panel). Only a small residual remains at −10 Hz due to imperfections in the quadrature geometry, after correcting for differences in gain of the gradiometric channels. For plotting, a 50 Hz low-pass filter was applied to the data in the time domain.

In the time domain, the processed complex gradiometric-quadrature signal is written as

$$S\left(t\right) = e^{i\phi}\left[a \cdot x\left(t\right) + i\, b \cdot y\left(t\right)\right] , \tag{4.3}$$

where $x\left(t\right)$ and $y\left(t\right)$ are the gradiometric signals, and ϕ is an overall phase selected such that the real part of the frequency spectrum has an absorptive peak (see below) [270]. The numerical coefficients a and b are defined so that $a + b = 2$, and may be adjusted to account for possible differences in gain between the two channels—usually a few percent or less, based on suppression of the residual negative-frequency peak. Prior to the Fourier transform, zeros may be added to the end of the time series defined by Eq. (4.3) (zero-filling) in order to increase the spectral resolution.

All frequency spectra throughout this manuscript are plotted such that the y-axis has units of pT/Hz or fT/Hz, depending on the signal strength. These units arise from the discrete Fourier transform (DFT) used to convert data from the time domain to the frequency domain and subsequent data processing, as explained in detail in Section 4.5.

The exact SNR enhancements attainable by the gradiometric quadrature method depend strongly on performance of the individual sensors, which may vary between experiments, as well as non-common-mode systematic noise. In our experience with water calibration samples, compared to single-channel spectra, SNR could be enhanced up to 75% via gradiometry alone and up to 300% via the gradiometric quadrature method (depending on sensor performance). This indicates not only that gradiometry is effective in terms of noise suppression, but also that the quadrature approach is more beneficial than simply summing the positive-frequency and negative-frequency peaks in a traditional "mirrored" non-quadrature spectrum. See Section 4.5 for quadrature simulations, gradiometer sensitivity data, and further details about phasing of quadrature signals. We expect that gradiometric quadrature detection can be especially beneficial for situations in which sensitive magnetometers operate in unshielded environments—if the contribution from common-mode noise dominates the contribution from uncorrelated noise at the positions of two sensors, total measurement noise will be significantly suppressed.

4.2.3 Leaf harvest and sample preparation

A description of all 19 tree-leaf samples included in our study is provided in Table 4.1. For identification purposes, samples from each genus were numbered in order of preparation/measurement date. We note that, due to seasonal availability, evergreen (spruce, pine, and yew) leaves were collected from late February to early April, while deciduous (hazel, cherry, beech, and oak) leaves were collected from early April to late May. Sample collection occurred as close as possible to the time of first measurement. All samples were sourced from the Eurasian arboretum of the Mainz Botanical Garden, which informed the specific choice of species and/or cultivar, although we purposely selected a diverse range of common genera.

During harvest, a branchlet containing sufficient leaf coverage was cut from the branch tip of the tree donor and immediately placed in a glass beaker partially filled with distilled water such that the cut end of the branchlet was submerged, as shown in the photo inset of Fig. 4.3. Sample preparation in the laboratory proceeded as follows. Leaves or needles were gently removed from the branchlet, thoroughly dried with a clean tissue to remove any excess moisture, and packed into a pristine glass shell vial (BGB SV2ML) with outer diameter 11.6 mm and interior volume $3.3\,\mathrm{cm}^3$. Spruce, pine, and yew needles were placed lengthwise vertically into the vial, whereas the hazel, cherry, beech, and oak leaves had to be rolled or folded. Care was taken to avoid tearing or otherwise damaging leaves during sample preparation, thereby preserving the original structure of the plant tissue, while fitting as many leaves or needles as possible into the tubular vial (Fig. 4.3 photo inset). Due to leaf geometry, it was not possible to achieve completely uniform density of leaf material in the vial, particularly for larger deciduous leaves. Each individual vial and its plastic cap were weighed with a digital scale before and after leaf insertion to extract the total leaf mass. Vials were capped prior to and throughout each 13 h experiment in the relaxometry setup, to prevent dehydration of the sample. After each experiment, the capped vial was removed from the setup, uncapped to release any trapped water vapor, recapped and weighed again. We found that post-measurement mass was always within a few mg of pre-measurement

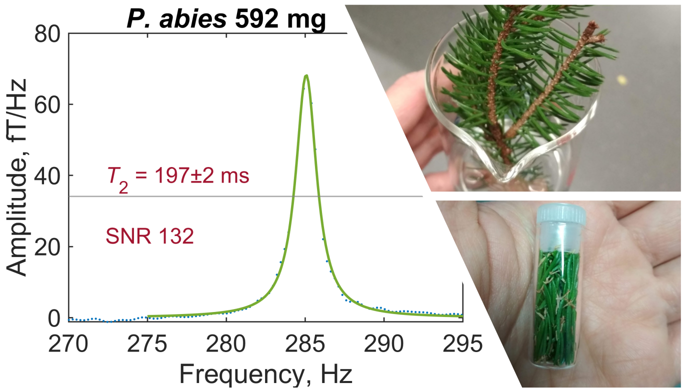

Figure 4.3: Example of a typical leaf spectrum recorded by gradiometric quadrature detection (spruce sample S1). Water-proton signal has been fitted with a Lorentzian and phased such that fit residuals are minimized—see text for details of data analysis. Inset photos show a freshly harvested spruce branchlet (top) and a prepared sample of spruce needles (bottom).

mass (Table 4.1), suggesting that leaf dehydration during the experiment was negligible, and that little to no excess water vapor had been contained inside the vial.

For the dehydration investigation, one evergreen genus (spruce) and one deciduous genus (oak) were selected; each sample was measured three different times, on the dates indicated in Table 4.1. Between experiments, the sample vial was stored uncapped in an on-site plant growth chamber (poly klima PK-520, 22°C, 12/12 h light/dark cycle, no humidity control). Because the vial was open only at one end, uniform dehydration of the leaf content could not be ensured. However, visible inspection of leaf color as well as the usual weighing procedure indicated that water loss had occurred during each storage period. It was critical to ensure that no condensation collected inside the vials at any stage of dehydration or measurement preparation, as this could introduce an additional spurious water-proton signal (sharp peak due to free water) not originating from water protons contained in the leaves themselves.

4.2.4 Leaf measurements

Each leaf measurement was conducted under identical experimental conditions to produce a proton-NMR spectrum as in Fig. 4.3. A resonance frequency of around 285 Hz, corresponding to a 7 μT precession field with 1.5 mA applied to the piercing solenoid, was selected to avoid lower-frequency noise while remaining with the sensitive bandwidth of the magnetometers (see Section 4.5). In the plotted spectrum, linear background was removed in the region 260–320 Hz and a Lorentzian fit (three-parameter Lorentzian function with constant term) was performed using the *lorentzfit* script in Matlab. As expected, the experimental lineshape is well-fitted by a Lorentzian, as it results from an exponentially decaying signal. Phasing of the quadrature signal was optimized by minimizing the root mean square error (RMSE) of the fit. Using the calculated fit parameters and errors thereon, the fit amplitude and linewidth (FWHM, full width at half maximum) were extracted. Typical fit amplitudes

Genus	**Species/cultivar**	**Sample**	**Date measured, 2023–MM–DD**	**Leaf mass, ±1 mg**	**Signal amplitude, fT/Hz**	T_2**, ms**
spruce (*Picea*)	Norway spruce (*Picea abies*) “Acrocona”	S1	02–24	592	68.3 ± 2.2	197 ± 2
			02–27	520	26.7 ± 0.9	158 ± 2
			03–08	344	2.5 ± 0.5	164 ± 13
		S2	02–25	648	53.3 ± 2.1	151 ± 2
			02–28	590	27.0 ± 0.6	162 ± 2
			03–13	322	0.9 ± 0.7	290 ± 83
	Norway spruce (*Picea abies*)	S3	03–02	664	30.0 ± 1.1	193 ± 3
			03–04	592	11.7 ± 0.7	182 ± 4
			03–14	393	2.2 ± 0.8	258 ± 37
		S4	03–03	714	34.9 ± 3.3	310 ± 11
			03–07	616	27.4 ± 1.7	295 ± 7
			03–16	414	1.4 ± 0.7	296 ± 57
pine (*Pinus*)	mountain pine (*Pinus uncinata*)	P1	03–09	1001	10.2 ± 1.0	196 ± 7
		P2	03–10	516	13.1 ± 0.8	173 ± 4
	dwarf mountain pine (*Pinus mugo*)	P3	03–17	512	26.3 ± 1.9	324 ± 9
		P4	03–20	503	22.5 ± 1.5	264 ± 7
yew (*Taxus*)	common yew (*Taxus baccata*)	Y1	03–22	596	4.5 ± 0.6	191 ± 10
		Y2	04–06	690	3.3 ± 0.5	182 ± 10
hazel (*Corylus*)	common hazel (*Corylus avellana*)	H1	04–04	404	5.2 ± 0.7	193 ± 10
		H2	04–07	584	9.8 ± 0.7	209 ± 6
		H3	04–10	682	19.2 ± 1.2	262 ± 6
cherry (*Prunus*)	bird cherry (*Prunus padus*)	C1	04–11	525	23.7 ± 3.9	223 ± 14
		C2	04–12	504	34.7 ± 5.1	189 ± 11
beech (*Fagus*)	European beech (*Fagus sylvatica*) “Rohanii"	B1	05–04	463	48.6 ± 3.4	259 ± 7
		B2	05–05	446	44.2 ± 4.3	355 ± 13
oak (*Quercus*)	pubescent oak (*Quercus pubescent*)	O1	05–17	932	70.3 ± 3.1	222 ± 4
			05–23	738	2.8 ± 0.8	348 ± 38
			05–30	721	3.5 ± 0.8	396 ± 33
		O2	05–19	531	36.0 ± 2.9	233 ± 7
			05–25	323	2.3 ± 1.0	536 ± 93
			05–31	254	4.1 ± 1.4	563 ± 75

Table 4.1: Overview of the leaf measurement campaign, in which samples from seven different tree genera were studied. Branchlets were freshly harvested in the Mainz Botanical Garden and transported to the lab in a beaker of distilled water for immediate sample preparation and measurement. Intact leaves were carefully dried and packed into a 2 mL closed glass vial, which was weighed and inserted into the experimental apparatus for a 13 h measurement (4096 scans). For dehydration studies (spruce and oak), sample vials were stored uncapped between measurements in a plant growth chamber at 22°C.

were on order 1 to 10 fT/Hz—at least three orders of magnitude smaller than for pure water samples of similar volume—after averaging over 4096 scans (repetitions of the measurement protocol). The relaxation time T_2 is related to the FWHM Δ as $1/(\pi\Delta)$. Reported SNR values were obtained from the ratio of fit amplitude to the standard deviation of spectral noise in the region 265–275 Hz. To avoid artificial broadening of the spectral line, no apodization was used, i.e. $\lambda = 0$ in Eq. (4.3); instead, a 300 Hz low-pass filter was applied to each spectrum for lineshape correction of the averaged signal. Measured proton-signal amplitudes and T_2 times are recorded for all 35 leaf experiments in Table 4.1. Complete fitted spectra, along with example analysis code and further details of the analysis protocol, may be found in Section 4.5.

In principle, multiple mechanisms may affect the spectral linewidth. These include magnetic-field gradients at the location of the sample, combined effects of different relaxation mechanisms, and possible contributions from non-water protons. Due to the significant differences in linewidth between liquid and leaf samples, we conclude that field inhomogeneity at the location of the sample is negligible, and therefore we report T_2 rather than T_2^* times in this work. As described in Section 4.2.2, the dead time required before data acquisition places a lower limit of 25 ms on measurable T_2 times, which is acceptable for studies of free or loosely bound water protons. Because experimental parameters remained unchanged over the course of the leaf study and all data underwent an identical analysis procedure, direct comparison of signal amplitudes and T_2 times is possible. Comparing the leaf results to typical water calibration data, we find that T_2 times in fresh leaf samples are an order of magnitude shorter than in liquid water samples of similar volume.

4.3 Results

Figures 4.4 and 4.5 provide graphical representations of the results reported in Table 4.1. In Fig. 4.4A, we see that the normalized signal amplitude of the spectra obtained from freshly prepared leaf samples varies significantly by tree genus. This may indicate different water-storage capacities of leaves from different genera. It is interesting to note that packing more leaf matter into the sample vial to increase the overall sample mass did not necessarily increase the normalized signal amplitude, for leaves of the same species. This could be attributed to two effects: (1) non-uniformity of the packing of leaf matter inside vials and (2) demagnetization effects due to the fact that samples are cylindrical rather than spherical. Due to leaf shape, distribution of leaf material in the sample vial is not necessarily uniform and this is generally worse for deciduous trees than for evergreen trees, due to the needle-like form of the latter. We observe that evergreen tree leaves fill up vials more uniformly. Demagnetization field effects due to cylindrical sample geometry can result in lowered signal for some samples compared to others (Table 4.1). Future studies are warranted to investigate the effects of sample geometry and uniformity of leaf matter on the magnitude of observable NMR signals and the precise amount of water giving rise to them. In contrast to the amplitude results, we see from Fig. 4.4B that average measured

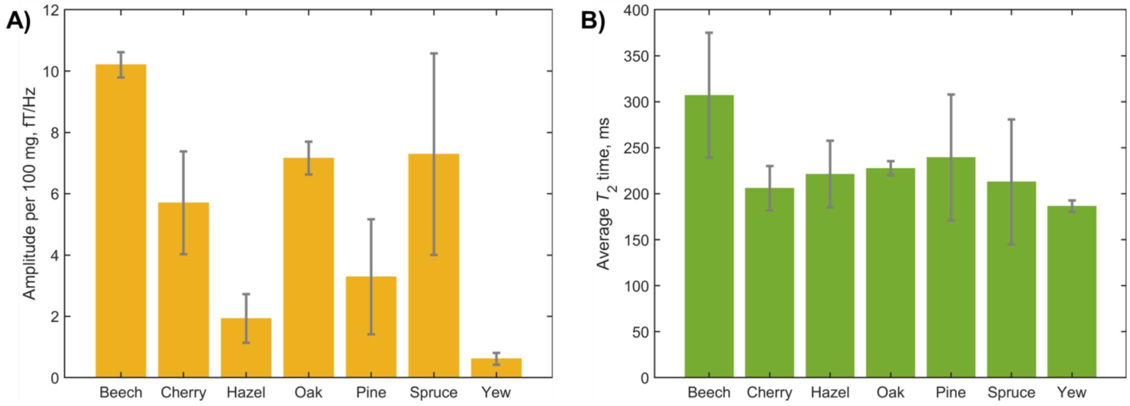

Figure 4.4: Results of the cross-species leaf-relaxometry study encompassing 19 fresh leaf samples. **A)** Average normalized measured water content from the different tree genera. Signal amplitudes were extracted from Lorentzian fits of the measured spectra; error bars indicate the standard deviation of signal amplitude for each genus. Note that the spruce and pine data encompass multiple species or cultivars (Table 4.1). **B)** Average T_2 times, extracted from Lorentzian fits of the measured spectra; error bars indicate the standard deviation for each genus.

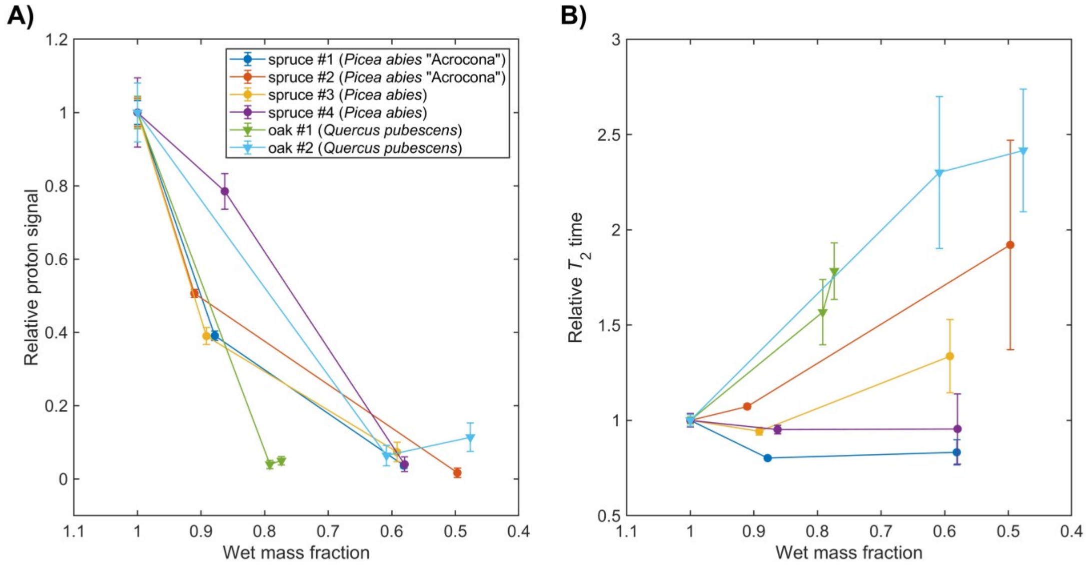

Figure 4.5: **A)** Tracking water content with dehydration in spruce (*P. abies*) and oak (*Q. pubescens*) leaves, see Table 4.1. Signal amplitudes and errors were extracted from Lorentzian fit parameters of the measured spectra; lines connecting data points are a guide to the eye. **B)** Tracking proton T_2 relaxation times with dehydration. Relaxation times and errors were extracted from Lorentzian fit parameters of the measured spectra; lines connecting data points are a guide to the eye.

T_2 times do not appear to vary significantly among the studied tree genera.

In Fig. 4.5, showing the results of the spruce/oak dehydration study, two trends can be observed. First, we observe an overall decrease in signal amplitude as sample mass decreases due to water loss, indicating that our experiments are primarily sensitive to water protons, as expected. However, we note that the dependence on sample mass is not entirely linear—this may be related to inhomogeneous dehydration of the sample, as mentioned above, as well as possible signal contributions from non-water protons. Second, an overall increase of T_2 times, i.e. narrowing of the water-proton peak, is observed as sample mass decreases. This trend is more pronounced for the oak samples, even accounting for increased uncertainty on T_2 due to reduction of SNR with dehydration. Notably, T_2 increases most dramatically for oak samples, as compared to spruce.

4.4 Discussion

In this study, we showcased several key findings, including the noninvasive and nondestructive measurement of water signals in intact *ex vivo* plant parts using a proton relaxometry protocol at hypogeomagnetic field. Additionally, we achieved signal-to-noise ratio enhancement of weak biological NMR signals from non-solution samples by employing a gradiometric quadrature detection scheme, especially useful in a future deployment of this technology in the field. Our research involved a comparative investigation of water-proton signals and T_2 relaxation in 19 tree-leaf samples, encompassing samples from seven genera, eight species, and nine cultivars. With this, we demonstrated sensitivity to the evolution of water-proton signals and T_2 relaxation times through repeated measurements of dehydrating leaf samples.

The experiments reported here were intended as a proof-of-principle of the above, and have not yet attempted to answer specific biological questions. Nonetheless, the preliminary results displayed in Figs. 4.4–4.5 already contain information which suggests future lines of relaxometry research with tree leaves. For example, the observed differences in normalized water-proton signal amplitude among different genera and species/cultivars may motivate further large-sample-size studies of water-storage capacity and possible seasonal variations. By contrast, the relative uniformity of measured T_2 times in all fresh leaf samples indicates that, at least in the hypogeomagnetic field regime, water-proton relaxation in leaf tissue is dominated by mechanisms common to the studied tree types. The observed tendency toward lengthening of T_2 times (narrowing of the proton precession peak) with leaf dehydration, particularly in the measured oak samples, may seem contradictory to intuition—if one expects dehydration and tissue death to further constrain molecular motion and lead to broadening of the spectral feature. However, our result appears to be consistent with previous benchtop relaxometry studies where leaf senescence was correlated with changes in water distribution at the cellular level as well as lengthening of T_2 components [253, 254]. Thus, we hope that our tree-leaf dehydration study will help open to the door to further relaxometry-enabled research on drought stress and tolerance in the context of forestry and agriculture.

Further improvements to the experimental setup will enable the affordable atomic-magnetometer based relaxometry device to achieve the functionality of commercial benchtop spectrometers for biological applications. These refinements may include implementation of spin-echo pulse sequences, SNR enhancements via suppression of low-frequency noise and optimization of the shuttling field profile, and shimming (field compensation) of stray magnetic fields and gradients. Relaxation-dispersion studies (measuring relaxation times as a function of field) may also reveal further information about water-storing structures [271–

273]. Instrumentation such as custom magnetometers tailored to plant samples—with reduced standoff distance and surface temperature—will improve biocompatibility, and the use of Earth-field magnetometers would even enable unshielded measurements (see [274] and references therein). The shielded regime is itself of fundamental interest, for example in studying properties of biological tissues under hypogeomagnetic conditions such as those encountered during long-distance spaceflight. Relaxometry studies of systems in which NMR signals originate from molecules other than water are also valuable, since other relaxation mechanisms can be involved [275]. While future experiments need not be limited to relaxometry of protons only, NMR-enabled investigation of plant water dynamics is highly warranted, particularly in ultralow and hypogeomagnetic regimes.

4.5 Appendix

4.5.1 Photographs and apparatus

Figure 4.6 shows a photo of the experimental setup as well as a selection of measured samples. The following hardware is included in the setup:

- *Experimental timing and data acquisition*—NI cDAQ-9189 ethernet chassis, two NI 9401 TTL-pulse cards with NI 9924 adapters, NI 9215 BNC acquisition card;
- *Spin polarization*—custom 1 T Halbach magnet produced in-house;
- *Mechanical shuttling*—Arduino Uno, Sanyo Denki StepSyn stepping motor 103H7123-5640 with driver, RS PRO plastic gear rack and aluminum rail;
- *Magnetic shielding*—Twinleaf MS-1LF ferrite magnetic shield with CS121 current supply;
- *Spin manipulation*—homemade copper double-layer piercing solenoid (inner diameter 20 mm, height 50 cm, resistance 11.5 Ω, calibration 4.5 nT/µA) wound around an acrylic tube (Acrylhaus) and connected to DM Technologies Multichannel Current Source, homemade 3D-printed ABS-plastic coil frame holding three orthogonal Helmholtz coil pairs (radius 33 mm, resistance 0.9 Ω, 10 copper windings, calibration 256 nT/mA) connected to Mini-Circuits switch ZASWA-2-50DRA+ and three Basetech BT-305 DC power supplies;
- *Detection*—two QuSpin Zero-Field Magnetometers (QZFM Gen-2) also contained in the coil frame.

Many of the commercial electronic items could be replaced with lower-cost or homemade alternatives; our choice of equipment was largely informed by what was already available in our labs.

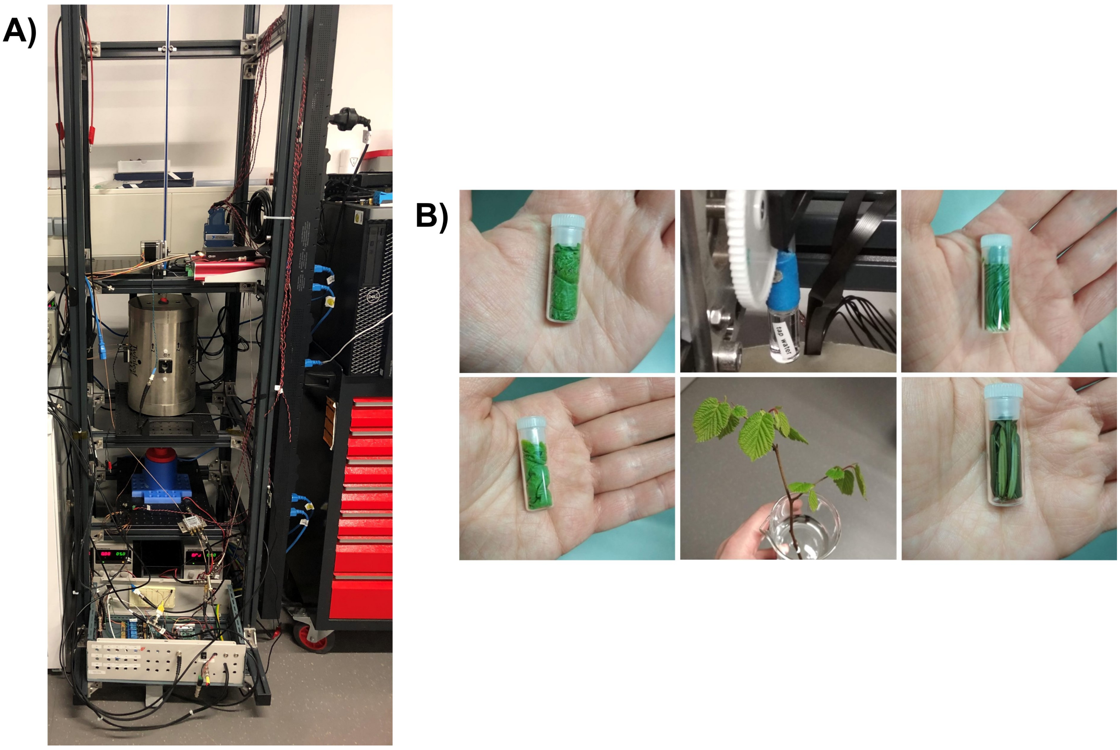

Figure 4.6: Photo collage of the relaxometry setup and samples. **A)** Experimental apparatus, cf. Fig. 4.2A. **B)** Clockwise from top center: water calibration sample, pine sample, yew sample, harvested hazel branchlet, cherry sample, hazel sample.

4.5.2 Expected magnetic-field amplitudes

For a pure water sample polarized at $B_\mathrm{p} = 1\,\mathrm{T}$ and room temperature $T = 293\,\mathrm{K}$, the expected thermal polarization of protons is [276, 277]

$$P_\mathrm{therm} = \frac{\gamma_{^1\mathrm{H}}\,\hbar\,(I+1)\,B_\mathrm{p}}{3\,k_\mathrm{B}T} = \frac{\gamma_{^1\mathrm{H}}\,\hbar\,B_\mathrm{p}}{2\,k_\mathrm{B}T}\,, \tag{4.4}$$

where $\gamma_{^1\mathrm{H}}/2\pi = 42.6$ MHz/T and $I = 1/2$. This calculation yields

$$P_\mathrm{therm} = \frac{\left(42.6\times10^{6}\,\mathrm{Hz}\cdot\mathrm{T}^{-1}\right)\left(6.63\times10^{-34}\,\mathrm{J}\cdot\mathrm{s}\right)(1\,\mathrm{T})}{2\left(1.38\times10^{-23}\,\mathrm{J}\cdot\mathrm{K}^{-1}\right)(293\,\mathrm{K})} = 3.5\times10^{-6}\,. \tag{4.5}$$

Given the molar concentration of water protons, $C = 110$ M, the amplitude of sample magnetization (magnetic moment per unit volume) can then be estimated as

$$\begin{aligned} M &= C\cdot\gamma_{^1\mathrm{H}}\,\hbar I\cdot P_\mathrm{therm} \\ &= \left(110\,\mathrm{mol}\cdot\mathrm{L}^{-1}\right)\left(6.02\times10^{23}\,\mathrm{mol}^{-1}\right)\left(42.6\times10^{6}\,\mathrm{Hz}\cdot\mathrm{T}^{-1}\right)\left(6.63\times10^{-34}\,\mathrm{J}\cdot\mathrm{s}\right)\cdot \\ &\quad\cdot\left(\frac{1}{2}\right)\left(3.5\times10^{-6}\right) \\ &= 3.3\times10^{-6}\ \mathrm{A}\cdot\mathrm{m}^2\cdot\mathrm{L}^{-1} = 3.3\times10^{-3}\ \mathrm{A}\cdot\mathrm{m}^{-1}\,. \end{aligned} \tag{4.6}$$

For a sample of volume $V = 1$ mL, the magnetic moment is then $m = M\cdot V = 3.3\times10^{-9}\ \mathrm{A}\cdot\mathrm{m}^2$.

Let us assume that the sample is a uniformly magnetized sphere, giving rise to a pure dipole magnetic field outside. Referring to Eqs. (4.1)–(4.2) and ignoring any relaxation mechanisms, the maximum magnetic-field amplitude measured at a standoff distance 17.5 mm from the center of the sample is

$$B = \frac{\mu_0\, m}{2\pi r^3} = \frac{\left(1.26\times10^{-6}\,\mathrm{N\cdot A^{-2}}\right)\left(3.3\times10^{-9}\,\mathrm{A\cdot m^2}\right)}{2\pi\,(0.0175\,\mathrm{m})^3} \approx 120\,\mathrm{pT}\,. \tag{4.7}$$

This amplitude is fairly robust with respect to temperature fluctuations, varying only a few percent per 10°C.

4.5.3 Gradiometric quadrature detection: Simulations and signal processing

Figures 4.7 and 4.8 correspond to Figs. 4.3—4.7 illustrates processing of a simulated time trace, while Fig. 4.8 shows the effect of phasing on experimental results.

4.5.4 Sensor performance

Gradiometer sensitivity is presented in Fig. 4.9—both channels exhibit a noise floor of around 100 $\mathrm{fT}/\sqrt{\mathrm{Hz}}$ within the bandwidth of the magnetometers. Feedback control of the atomic-vapor-cell heater is turned off during measurement, as it is affected by the DC magnetic-field pulses and may introduce additional low-frequency noise which negatively impacts measured lineshapes.

4.5.5 Calibration of experimental parameters

Various calibration data are included here, showing optimization of the following: shuttling distance above the polarizing Halbach magnet (Fig. 4.10), duration of the applied DC magnetic-field pulse (Fig. 4.11), polarization time in the magnet (Fig. 4.12), and choice of proton-spin precession frequency (Fig. 4.13). All signals were obtained using the gradiometric quadrature method.

We expect a $\pi/2$ DC pulse, which exploits Larmor precession to rotate magnetization by 90°, to fulfill the condition

$$2\pi\gamma_{^1\mathrm{H}}\, B_{\mathrm{y}}\, \tau_{\mathrm{p}} = \frac{\pi}{2}\,. \tag{4.8}$$

Here B_{y} is the pulse amplitude, held constant at $30\,\mu\mathrm{T}$ in our setup, and τ_{p} is a variable pulse duration. Given the proton gyromagnetic ratio $\gamma_{^1\mathrm{H}}/2\pi \approx 43\,\mathrm{Hz}/\mu\mathrm{T}$, we expect an optimal pulse duration of around $200\,\mu\mathrm{s}$, which agrees well with the experimental data plotted in Fig. 4.11.

Best practice to obtain optimized NMR spectra without lineshape correction involves polarizing spins for ~ 3 times the characteristic magnetization decay time T_1, and acquiring the FID signal for ~ 5 times the T_2 time. However, reduction of the experimental duty cycle is desirable in order to more efficiently increase the number of measurement averages

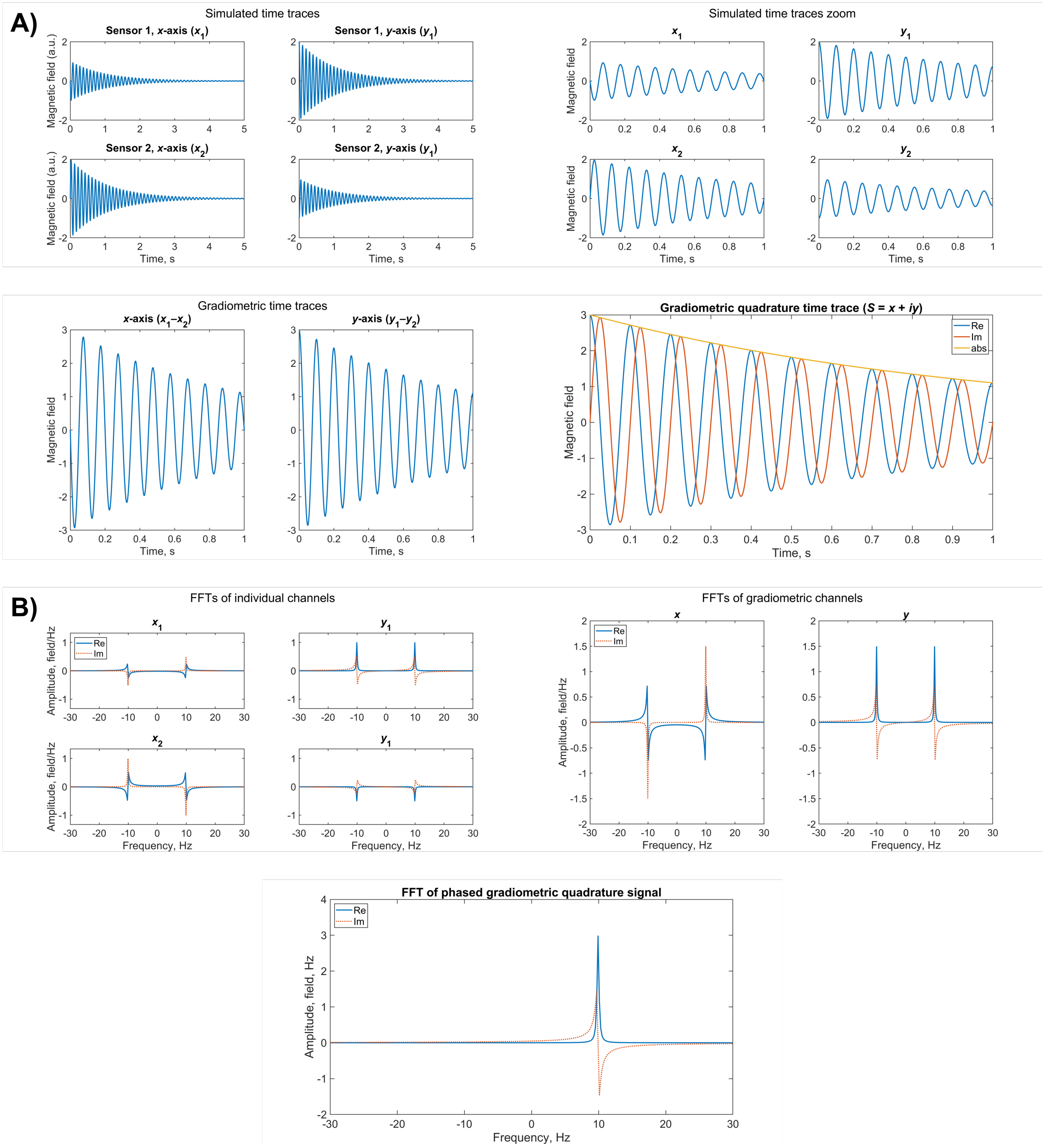

Figure 4.7: Simulations of magnetic-field measurements of a magnetic dipole precessing at 10 Hz in the x-y plane, following the detection geometry in Fig. 4.1. Here we assume that magnetization has been initialized along $\hat{y}$ prior to measurement and relaxes with a T_2 time of 1 s. **A)** Normalized time traces showing the free-induction-decay (FID) signal as seen by the four individual magnetometer channels (top row), the two gradiometer channels (bottom left), and the gradiometric quadrature channel (bottom right). **B)** Corresponding frequency spectra obtained by fast Fourier transform (FFT). An overall phase of $-\pi/2$ has been applied to the gradiometric quadrature time trace such that the real and imaginary parts of the resulting FFT (bottom panel) are absorptive and dispersive, respectively.

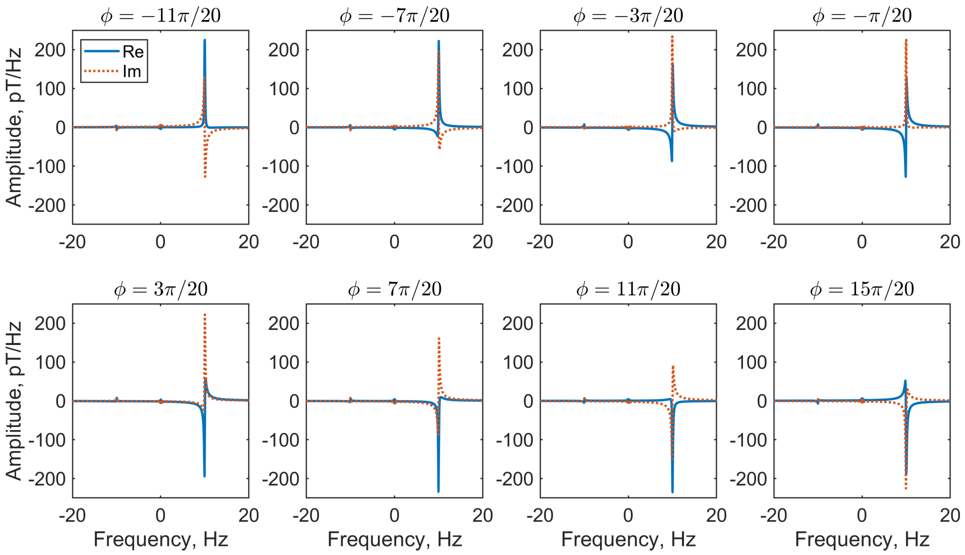

Figure 4.8: Phase sensitivity of the water calibration spectrum, cf. Fig. 4.3. To produce these plots, the measured gradiometric quadrature signal was multiplied by a variable overall phase $e^{i\phi}$.

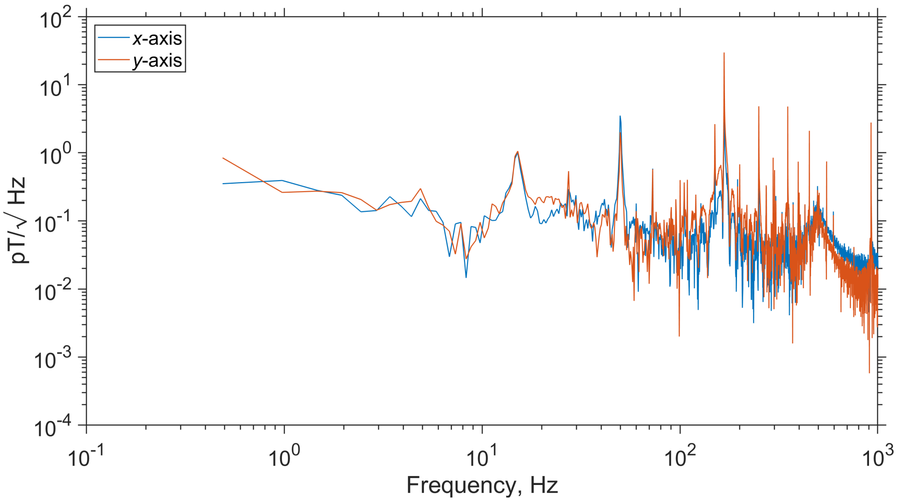

Figure 4.9: Noise floor of the gradiometric magnetometer channels, obtained by taking the power spectral density (PSD) of a single 2 s time trace with an empty sample vial, under experimental conditions and parameters identical to those used in the leaf measurement campaign (Fig. 4.14). Sensors are not responsive above 500 Hz due to an internal cut-off filter; the various background noise sources in the sensitive region below this frequency can be avoided in actual experiment by tuning of the solenoid precession field to an appropriate ^{1}H Larmor frequency (see Fig. 4.13).

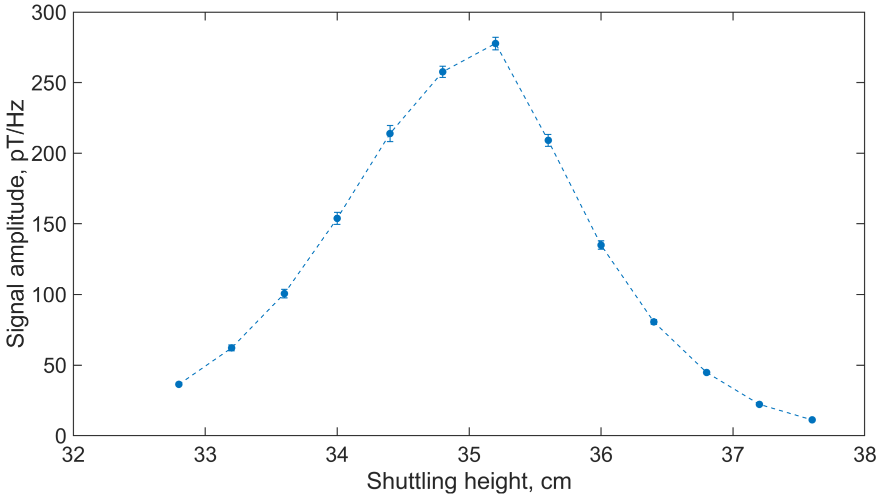

Figure 4.10: Amplitude of the Lorentzian fit to a 10 Hz water calibration signal (average of four scans) as a function of shuttling height above the polarizing magnet. The calibration sample was 1.5 mL of deionized (DI) water; height of the water column in the sample vial was approximately 2 cm. Error bars have been extracted from fit parameters; connecting dashed lines are a guide to the eye. Experimental settings: 10 s polarization time, 200 µs pulse, 10 s acquisition.

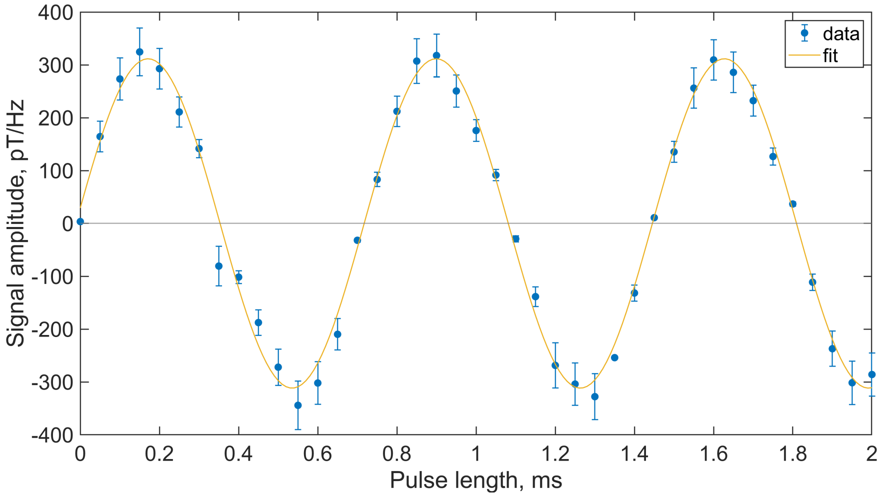

Figure 4.11: Measured nutation curve showing amplitude of the Lorentzian fit to a 10 Hz water calibration signal (2 mL of tap water, average of four scans) as a function of y-pulse duration with pulse amplitude 30 µT. A sinusoidal fit to the data is overlaid; error bars on the data points have been extracted from Lorentzian fit parameters. According to the fitted sine wave, maximum amplitude is reached at 171 ± 12 µs. Experimental settings: 10 s polarization time, shuttling height 35 cm, 3 s acquisition.

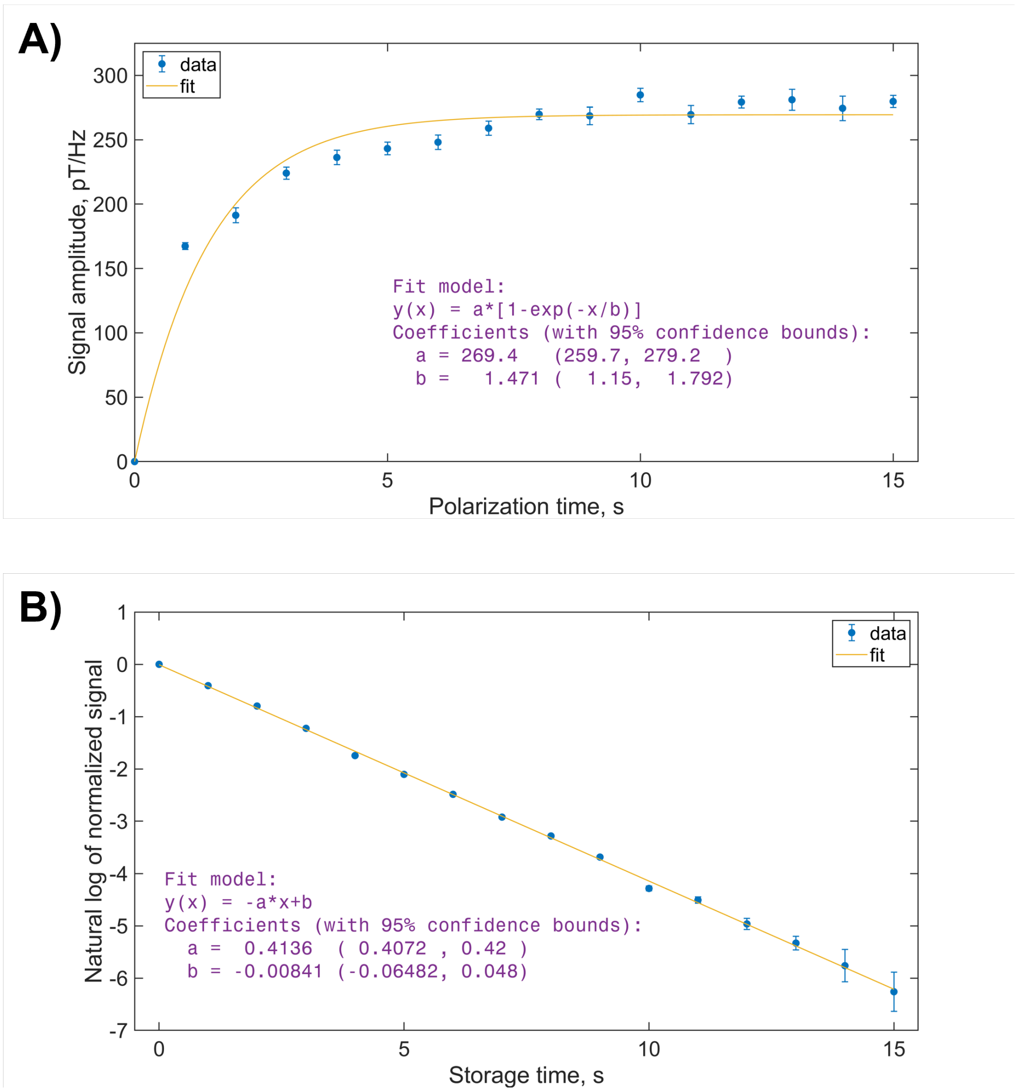

Figure 4.12: Investigation of polarization and storage times using the water calibration sample. **A)** Amplitude of the Lorentzian fit to a 10 Hz signal (average of three scans) as a function of polarization time t_p in the Halbach magnet prior to shuttling. Assuming a signal buildup $S(t) = S_\mathrm{p}\left[1 - \exp\left(-t_\mathrm{p}/T_{1,\mathrm{p}}\right)\right]$, where S_p is the maximal signal corresponding to the maximal achievable spin polarization, we find $T_{1,\mathrm{p}} = 1.47 \pm 0.16\,\mathrm{s}$. Error bars on the data points have been extracted from fit parameters. Experimental settings: shuttling height 35 cm, 200 µs pulse, 10 s acquisition. **B)** Alternative T_1 measurement based on varying the storage time in the solenoid, after shuttling and prior to pulse application. The signal decays exponentially from its maximum value at zero storage time, with a time constant of T_1. Taking the inverse slope of the fit, we find $T_1 = 2.42 \pm 0.01\,\mathrm{s}$. Polarization time was 10 s and four scans were averaged; all other experimental parameters were equivalent to those in the polarization-buildup measurement. Error bars on the data points have been extracted from the Lorentzian fit parameters.

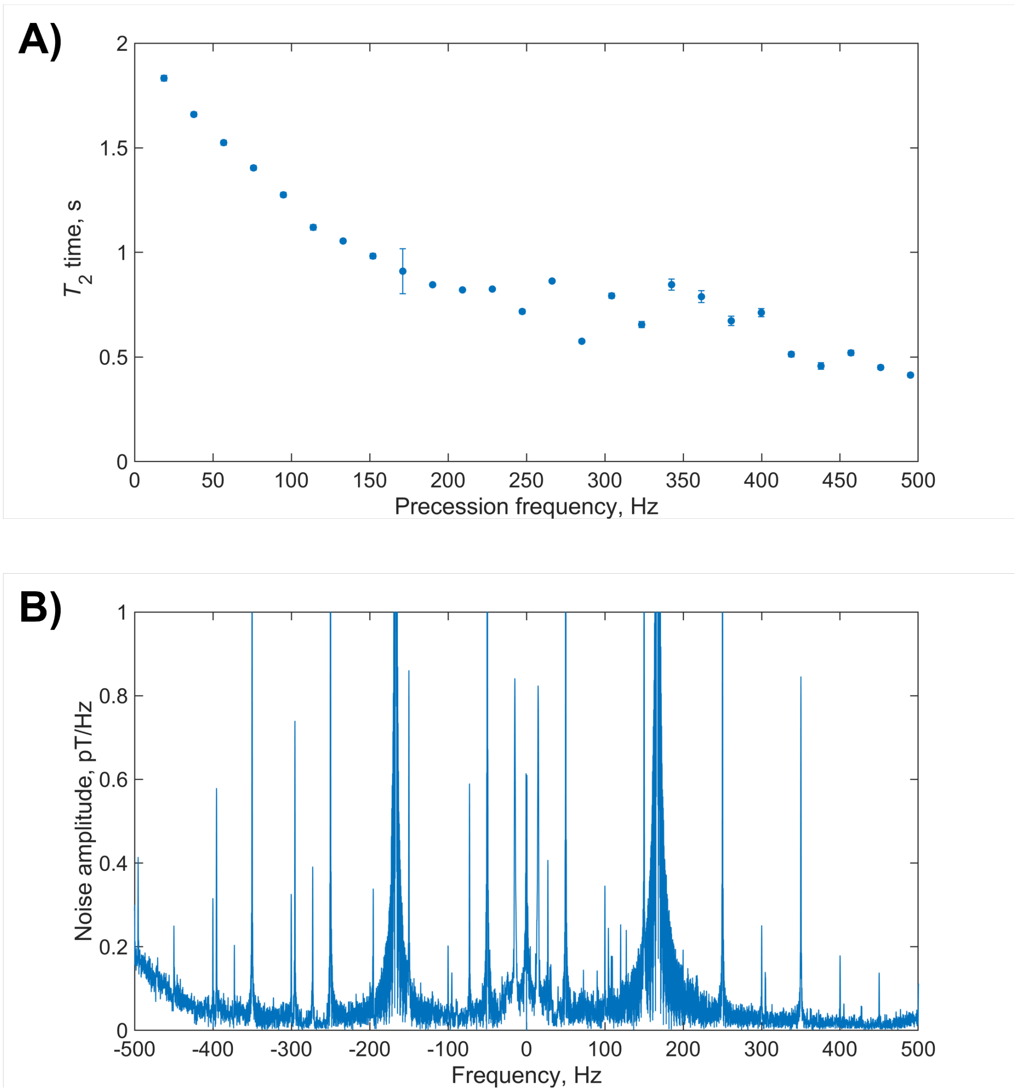

Figure 4.13: Frequency dependence of signal width and noise background. **A)** Evolution of measured proton T_2 time in the DI water sample as extracted from the width of the Lorentzian fit. Experimental settings: 10 s polarization time, shuttling height 35 cm, 200 µs pulse, 10 s acquisition, four scans. **B)** Amplitude FFT of the same data set as in Fig. 4.9 (average of four scans), zoomed in to the amplitude range below 1 pT. Because signals from leaves are typically three orders of magnitude smaller than those from water calibration signals at a given precession frequency, the relatively noise-free region between 250 and 300 Hz is selected as the best choice for leaf measurements, despite the reduction of T_2 due to lineshape broadening. Major background noise sources include 50 Hz power-line noise and harmonics thereof, as well as a large unidentified laboratory noise peak at 167 Hz. [The 167 Hz noise peak was later discovered to arise from electronic noise of one of the sensors, as the peak disappeared completely after replacing that sensor.] Given the sampling rate of 2 kHz and associated Nyquist frequency of 1 kHz, smaller noise peaks at 77 ± 50 Hz and harmonics are suspected to arise from interference of power-line noise and the 923 Hz internal modulation of the magnetometers.

with associated signal-to-noise ratio (SNR) enhancement. Note that T_1 times may depend on magnetic-field strength—see Fig. 4.12.

4.5.6 Leaf data

Figures 4.14–4.17 show fitted water-proton signals from all measured leaf samples, cf. Table 4.1. Oscillations in the spectral baseline are attributed to drifts in magnetometer response over the course of the 13 h data run, which lead to artifacts in the average time traces.

4.5.7 Data analysis

Processing of the experimental data is performed as follows. We begin with a discrete time series $S\left(j\right)$, a vector containing z data points, where z is a positive integer value usually chosen to be a power of 2. The DFT is carried out pointwise for each point j using a standard fast Fourier transform (FFT) algorithm in order to produce a new vector $S\left(k\right)$:

$$S\left(k\right)=\sum_{j=1}^{z}S\left(j\right)e^{[(-2\pi i)(j-1)(k-1)]/z}\,. \tag{4.9}$$

Note that because each point of $S\left(k\right)$ is a sum over all points in the time series, the amplitude scales with z and has units of magnetic field. This amplitude may be normalized by rescaling the vector as $S\left(k\right)/z$. Although Eq. (4.9) provides a measure of frequency, it is agnostic with respect to x-axis units, and the output vector $S\left(k\right)$ has the same length, z, as the input vector $S\left(j\right)$. In order to plot the spectrum as a function of frequency, we define a frequency axis from $-f_s$ to f_s, where f_s is the sampling rate of acquisition, with frequency spacing f_s/z between points. Furthermore, the zero-frequency components of $S\left(k\right)$ must be shifted to the center of the spectrum. Example code for carrying out these procedures in Matlab is provided.

According to NMR convention, the integral of a signal in frequency space should equal the initial amplitude of the FID and therefore have units of magnetic field; a convenient normalization sets the integral to 1, such that the mirrored peaks in non-quadrature spectra (Fig. 4.7) each have integral 0.5. This is only possible if the y-axis of the frequency spectrum has units of magnetic field per Hz. Such units do indeed arise in the analytical case of a continuous FT, in which an integral rather than a summation is performed over the time-domain signal. In order to approximate the continuous FT using a numerical DFT, we divide the frequency signal $S\left(k\right)$ by the frequency spacing or “bin size” f_s/z, which yields the desired units and integration properties.

Lineshape fitting of the gradiometric quadrature signal is performed using a three-parameter Lorentzian function

$$L\left(\nu\right)=\frac{p_1}{\left(\nu-p_2\right)^2+p_3}+c\,, \tag{4.10}$$

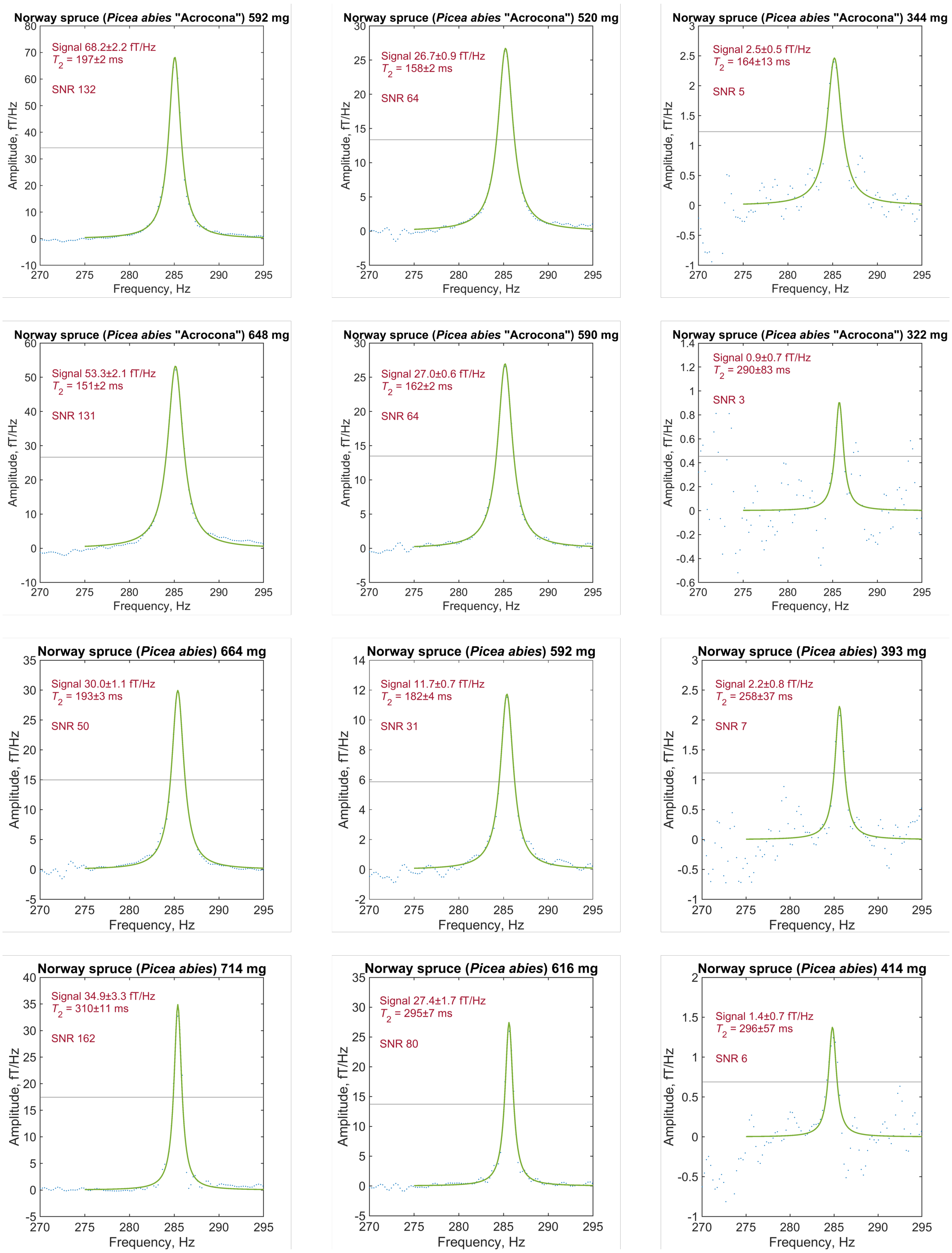

Figure 4.14: Spectra used in the **spruce** dehydration study; each row corresponds to a single sample.

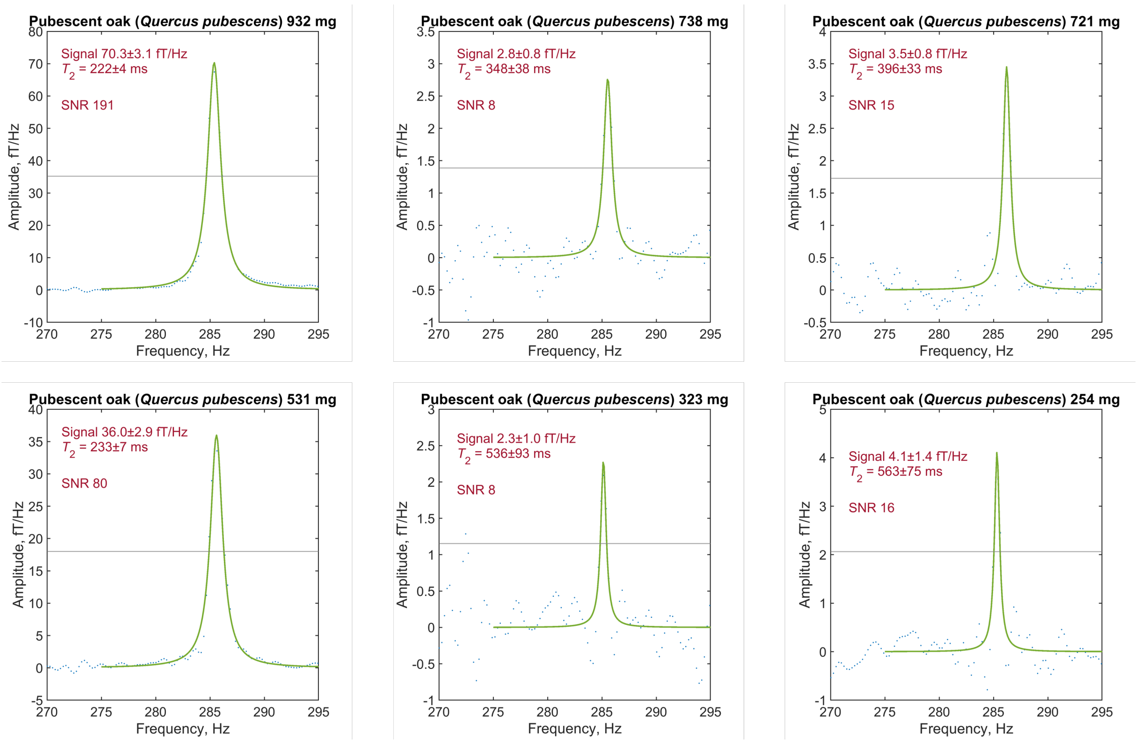

Figure 4.15: Spectra used in the **oak** dehydration study; each row corresponds to the same sample.

where ν is frequency, p_1, p_2, and p_3 are the fit parameters, and c is a constant. Spectral properties may be extracted from the fit parameters as follows: p_2 is the central peak position in Hz, p_1/p_3 is the fit amplitude, and $T_2 = 1/(2\pi\sqrt{p_3})$—equivalent to $1/(\pi\Delta)$, where Δ is the full width at half maximum (FWHM). In order to optimize phasing of the spectrum as described in Section 4.2.2, the phase ϕ is varied in steps of $\phi/20$ until the root mean square error (RMSE) calculated from fit residuals is minimized.

Further details of analysis steps may be found in the provided annotated Matlab analysis notebook 'AnalyzeLeaf.m' at the end of this document, which was used to produce the leaf spectra plotted in Figs. 4.14–4.17.

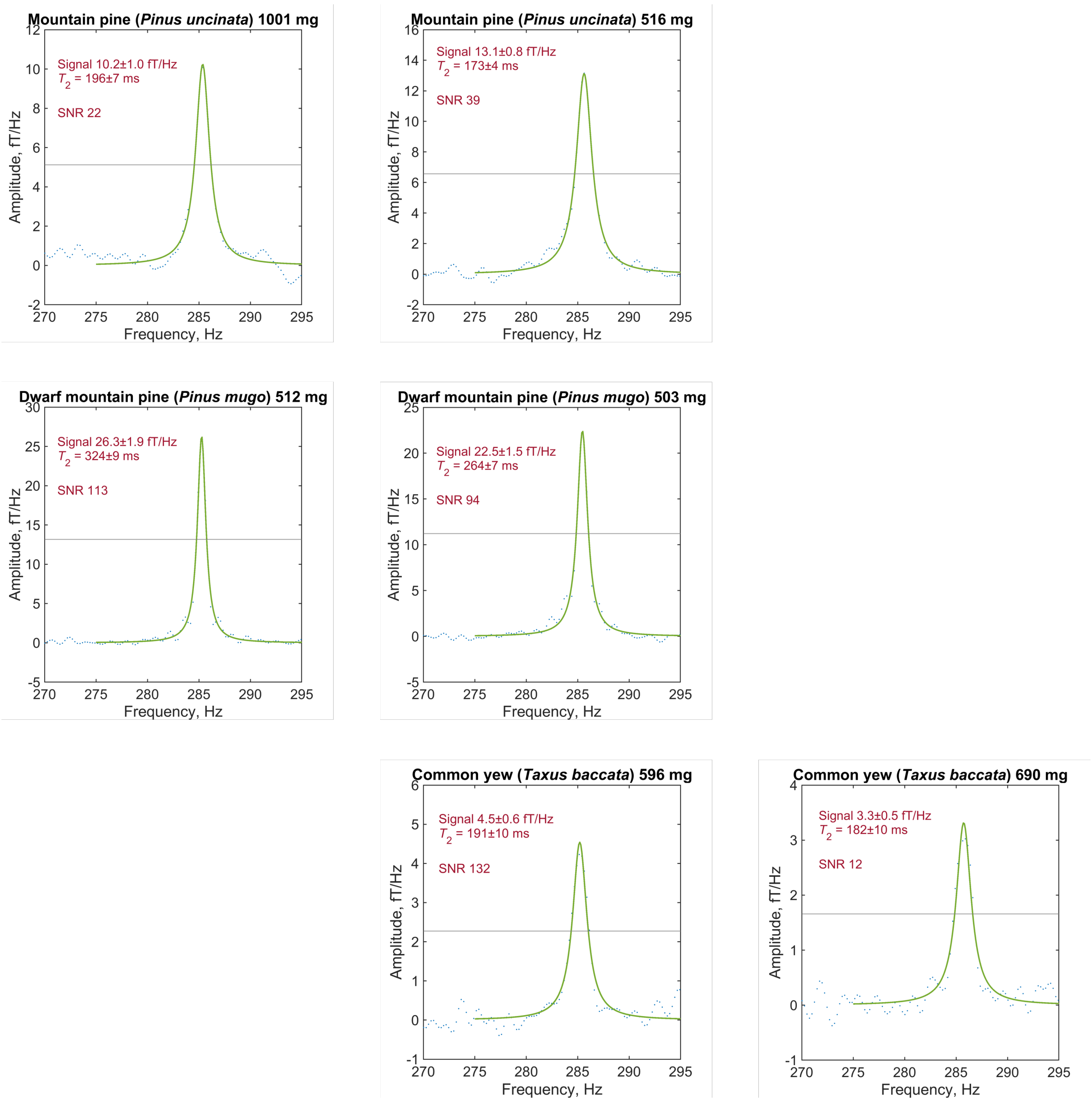

Figure 4.16: Spectra of leaves from evergreen trees including **pine** and **yew**; each plot corresponds to a different sample.

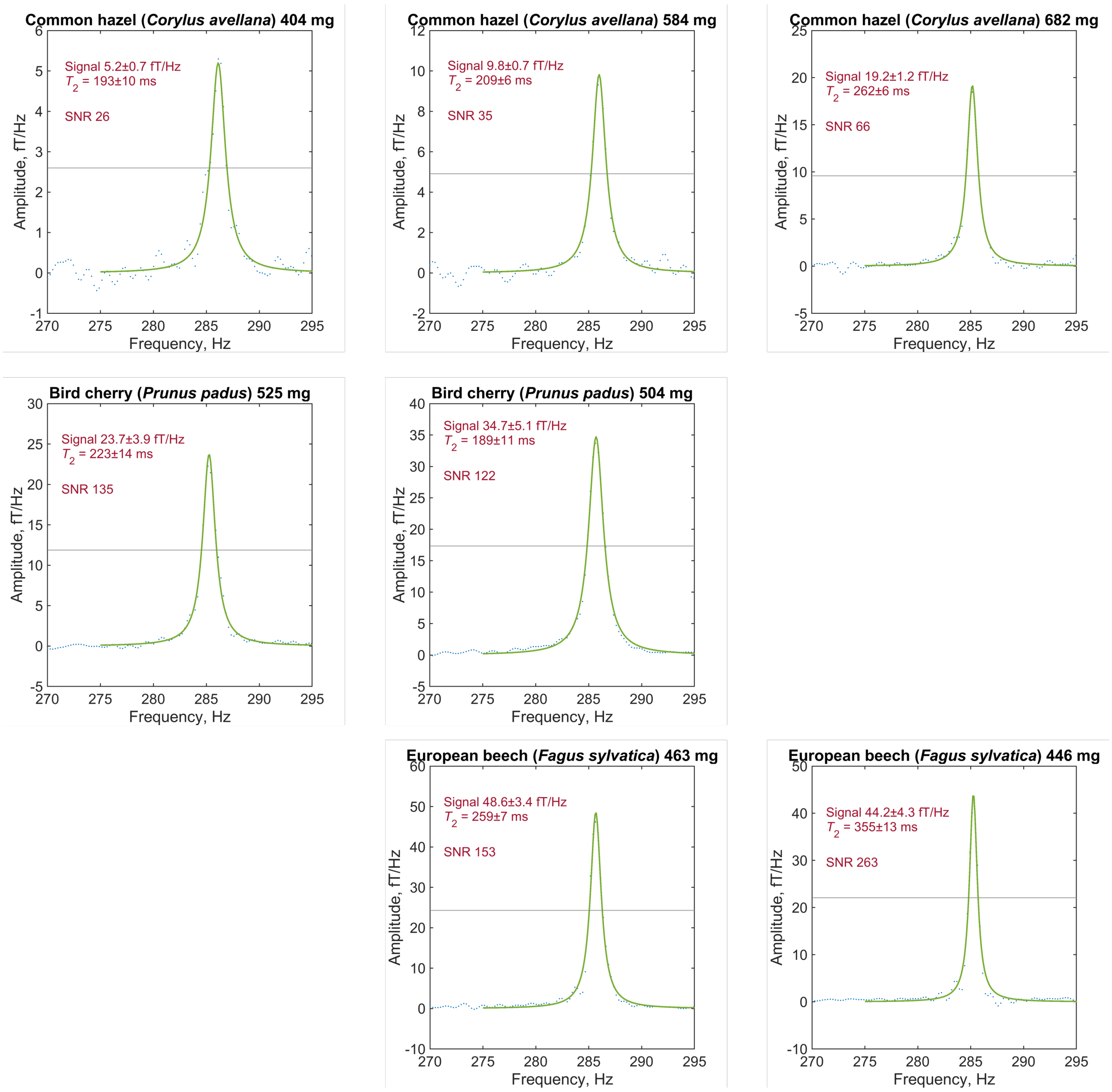

Common hazel (*Corylus avellana*) 404 mg

Common hazel (*Corylus avellana*) 584 mg

Common hazel (*Corylus avellana*) 682 mg

Bird cherry (*Prunus padus*) 525 mg

Bird cherry (*Prunus padus*) 504 mg

European beech (*Fagus sylvatica*) 463 mg

European beech (*Fagus sylvatica*) 446 mg

Figure 4.17: Spectra of leaves from deciduous trees including **hazel**, **cherry**, and **beech**; each plot corresponds to a different sample.

AnalyzeLeaf.m

```
%% Analyze leaf data
% need lorentzfit.m in same folder

% initialize magnetization along -x
% precession field along z (clockwise precession as seen from above)

% sensor channels: ACy,ACz,Q8y,Q8z (DAQ channels #2,3,4,5)
% rename using lab coordinate system: -y2,x2,x1,y1

% polarization time 5s
% z solenoid field for guiding/precession -1500uA = 7uT = 285Hz
% shuttling time 100ms
% shuttling height 440 steps = 35cm
% no waiting (storage) time
% y pulse 30uT, 200us
% acquisition time 2s

clearvars
close('all')

%% Time domain

% Load data file from notebook directory
Fs = 2000; %sampling frequency, Hz
T = 2; %acquisition time, s
nscans = 4096; %number of scans
data = zeros(Fs*T,5,nscans); %preallocate matrix
for i = 1:1:nscans
    a_i = load(['Folder\Filename_' num2str(i) '.dat']);
    data(:,:,i) = a_i; %create array with all data
end

% save('data_leaf.mat','data')
% load('data_leaf.mat');

% Define variables
t0 = data(:,1,1); %time (s)
L0 = length(t0); %length of signal
x1_0 = (data(:,4,:))*(1000/2.7); %convert V to pT
y1_0 = (data(:,5,:))*(1000/2.7);
x2_0 = (data(:,3,:))*(1000/2.7);
y2_0 = -(data(:,2,:))*(1000/2.7);

% Discard some initial and/or end points
n = 50; %number of initial points to discard
m = 0; %number of end points to discard
t = t0(n+1:L0-m);
x1 = x1_0((n+1:L0-m),:,:);
x2 = x2_0((n+1:L0-m),:,:);
y1 = y1_0((n+1:L0-m),:,:);
y2 = y2_0((n+1:L0-m),:,:);

% Plot raw time traces from single scan
figure('Name','Raw time traces offset') %figure 1
plot(t,x1(:,:,1))
ylabel('Magnetic field, pT'), xlabel('Time, s')
```

```
title('Raw time traces, single scan'), ax = gca; ax.FontSize = 20;
hold on
off = 200; %offset, pT
plot(t,y1(:,:,1)+off), plot(t,x2(:,:,1)+2*off), plot(t,y2(:,:,1)+3*off)
legend('sensor 1, x-axis','sensor 1, y-axis','sensor 2, x-axis','sensor 2, y-axis')

% Remove background
x1_d = detrend(x1); %remove linear trend
y1_d = detrend(y1);
x2_d = detrend(x2);
y2_d = detrend(y2);

% Plot detrended time traces from single scan
figure('Name','Time traces detrended') %figure 2
subplot(2,2,1), plot(t,x1_d(:,:,1))
yline(0);
ylabel('Magnetic field, pT'), title('Sensor 1, x-axis (x1)'), ax = gca; ax.FontSize = 16;
ylim([-100 100])
subplot(2,2,2), plot(t,y1_d(:,:,1))
yline(0);
title('Sensor 1, y-axis (y1)'), ax = gca; ax.FontSize = 16;
ylim([-100 100])
subplot(2,2,3), plot(t,x2_d(:,:,1))
yline(0);
ylabel('Magnetic field, pT'), xlabel('Time, s')
title('Sensor 2, x-axis (x2)'), ax = gca; ax.FontSize = 16;
ylim([-100 100])
subplot(2,2,4), plot(t,y2_d(:,:,1))
yline(0);
xlabel('Time, s'), title('Sensor 2, y-axis (y2)'), ax = gca; ax.FontSize = 16;
ylim([-100 100])
sgtitle('Detrended time traces, single scan')

% Gradiometry
x = x1_d-x2_d;
y = y1_d-y2_d;

figure('Name','Gradiometric time traces') %figure 3
subplot(1,2,1), plot(t,x(:,:,1),'Linewidth',1)
ylabel('Magnetic field, pT'), xlabel('Time, s')
title('x-axis (x = x1 - x2)'), ax = gca; ax.FontSize = 18;
ylim([-100 100])
subplot(1,2,2), plot(t,y(:,:,1),'Linewidth',1)
xlabel('Time, s'), title('y-axis (y = y1 - y2)'), ax = gca; ax.FontSize = 18;
ylim([-100 100])
sgtitle('Gradiometric time traces, single scan')

% Quadrature
phi = 0; %choose phase to minimize fit residuals
%phi = 1*pi/20;
lambda = 0; %apodization factor
S = exp(1i*phi-lambda*t).*complex(x,y);
S_avg = mean(S,3);

%% Frequency domain

% Quadrature
z=2^13; %add zeros to end of time series (zero-filling)
```

```
fS = fft(S(:,:,1),z);
f = (-z/2:z/2-1)*(Fs/z);
PS = 1000*fftshift(fS)/Fs; %convert to fT/Hz
fSa = fft(S_avg,z);
PSa = 1000*fftshift(fSa)/Fs;

figure('Name','Phased quadrature FFT single') %figure 4
plot(f,real(PS),'Linewidth',1)
hold on
plot(f,imag(PS))
legend('Re','Im'), ax = gca; ax.FontSize = 18;
ylabel('Amplitude, fT'), xlabel('Frequency, Hz')
title('Leaf, phased gradiometric quadrature signal, single scan'), ax = gca; ax.FontSize = 20;
xlim([270 295])

figure('Name','Phased quadrature FFT average') %figure 5
plot(f,real(PSa),'Linewidth',1)
hold on
plot(f,imag(PSa))
legend('Re','Im'), ax = gca; ax.FontSize = 18;
ylabel('Amplitude, fT'), xlabel('Frequency, Hz')
title('Leaf, phased gradiometric quadrature signal, 4096 scans'), ax = gca; ax.FontSize = 20;
xlim([270 295])

% Lorentzian fit
a = 5161; %260 Hz
b = 5223; %275 Hz
c = 5306; %295 Hz
d = 5408; %320 Hz
fp = f(a:d);
PSp = real(PSa(a:d));
PSp_d = detrend(PSp);
Z = transpose(PSp_d);
Zf = lowpass(Z,300,Fs); %low-pass filter
[yprime1 params1 resnorm1 residual1 jacobian1] = lorentzfit(fp(b-a:c-a),Zf(b-a:c-a),[],[],'3c');

figure('Name','Fitted spectrum') %figure 6
plot(fp,Zf,'b.','LineWidth',2)
hold on
plot(fp(b-a:c-a),yprime1,'r-','LineWidth',2)
ylabel('Amplitude, fT'), xlabel('Frequency, Hz')
title('Leaf, fitted spectrum'), ax = gca; ax.FontSize = 20;
xlim([270 295])

% Goodness of fit
sqres = residual1.^2;
Lres = length(residual1);
rmse = sqrt(sum(sqres)/Lres) %root mean square error

% [DEFAULT] '3c'    - Three parameter Lorentzian (with constant term)
%                     L3C(X) = P1./((X - P2).^2 + P3) + C
freq = 275:0.1:295;
p1 = params1(:,1);
p2 = params1(:,2);
p3 = params1(:,3);
c = params1(:,4);
y = p1./((freq - p2).^2 + p3) + c;
figure('Name','Fitted spectrum smooth') %figure 7
```

```
plot(fp,Zf-c,‘b.’,‘LineWidth’,3)
hold on
plot(freq,y-c,‘r-’,‘LineWidth’,2)
ylabel(‘Amplitude, fT’), xlabel(‘Frequency, Hz’)
title(‘Leaf common name (Scientific name) XXX mg’), ax = gca; ax.FontSize = 20;
xlim([270 295])

% Calculate peak parameters
peak_pos = p2 %peak position, Hz
amp = p1/p3 %fit amplitude, fT/Hz
hold on
yline(amp/2); %half maximum, fT/Hz
T2 = 1/(2*pi*sqrt(p3)) %T2, s

% Calculate SNR
sig = max(Zf-c); %signal amplitude
back = Zf(22:64); %noise region 265-275Hz
noise = std(back); %standard deviation of noise
SNR = sig/noise %signal-to-noise ratio

% Calculate errors on parameters
xCovariance = inv(jacobian1.’*jacobian1)*var(residual1);
%compute parameter covariance estimates from Jacobian and residuals
[R,sigma] = corrcov(xCovariance); %compute correlation matrix R & vector of standard deviations sigma
errT2 = sqrt( sigma(3,:)^2 / (16*pi^2*p3^3) ) %propagate errors
erramp = sqrt( sigma(1,:)^2/p3^2 + (p1*sigma(3,:))^2/p3^4 )
```

Author contributions

A.M.F.: Conceptualization, Data curation, Formal Analysis, Investigation, Methodology, Software, Visualization, Writing—original draft, Writing—review & editing. P.P.: Investigation, Methodology, Software, Writing—review & editing. D.A.B.: Conceptualization, Funding acquisition, Investigation, Methodology, Resources, Supervision, Writing—review & editing.

Acknowledgments

We thank Prof. Dmitry Budker and Erik Van Dyke for stimulating discussions and feedback, and acknowledge contributions from Dr. Kirill F. Sheberstov, Liubov Chuchkova, Oleg Tretiak, and Dr. Raphael Kircher in initial development of the experimental setup. The Halbach magnet used for spin polarization was designed by Dr. Peter Blümler. We thank the Mainz Botanical Garden Arboretum for providing samples for this study. Work was supported by the Alexander von Humboldt Foundation in the framework of the Sofja Kovalevskaja Award.

Chapter 5

Conclusion and outlook

This thesis has endeavored to demystify the technology of atomic magnetometry and showcase its power through measurements of tiny (femtotesla to picotesla) biomagnetic and magnetic resonance signals from plants—addressing some unanswered questions of plant biology in the process. Here we briefly summarize the main experimental accomplishments:

- Detection of plant biomagnetism with atomic magnetometers.
- Demonstration of biomagnetism in the Venus flytrap, *Dionaea muscipula*, confirming the existence of bulk currents in the trap, as well as demonstration of autonomous heat-induced action potentials.
- Nondestructive proton-NMR relaxation study of evergreen and deciduous tree leaves at hypogeomagnetic field, indicating a general decrease in water-proton spin-relaxation rates with dehydration.
- Development of a "gradiometric quadrature" detection geometry and analysis method for optimization of ZULF-NMR spectra.

For the proof-of-principle experiments reported here, we chose to employ commercially available atomic magnetometers, originally developed for measurements of the human brain. This choice was motivated by the fact that unknown biological mechanisms and fragile systems were under study, and reducing the number of experimental components which needed to be tuned and troubleshooted was the most efficient route to experimental success. As the magnetic signals from plants and plant parts become better understood, future experiments may benefit from development of customized plant-friendly sensors. In particular, reducing both the sensor footprint and offset distance from the sample will significantly improve the spatial resolution and SNR of measured signals, respectively. Improved sensor biocompatibility is achievable through reduction of elevated surface temperature due to heat transfer from the thermal atomic sensing volume—since plant systems are more heat-sensitive than animal systems, this will serve to boost plant health and longevity for more robust signals. Finally, optimizing the Size, Weight, and Power (SWaP) of devices will facilitate portability and operation "in the field".

To close the thesis, the remainder of this chapter provides a (largely pictorial) overview of current research activities building upon the results and instrumentation already presented.

5.1 The secret (magnetic) life of plants

Following up on the initial work conducted on Venus flytrap, further biomagnetometry efforts are focused on agricultural plants, fungi, and the forest floor (Fig. 5.1). It of great value to understand and protect our food systems, and studying high-value crop and greenhouse plants is of particular interest. One hot topic is the stress and defense response of plant systems to wounding stimuli, such as extreme weather, mechanical damage, or biotic attack. Wounding is known to unleash a multifaceted systemic reaction including chemical (calcium waves and the release of volatile organic compounds), hydraulic, genetic, hormonal, and electrical components [278]—the last remains the least understood, and lends itself to investigation with magnetometry (Fig. 5.2). Recently, the transfer of electrical wounding signals between different plants through a fungal mycelial network was also demonstrated [279], a milestone in the field of fungal electrophysiology [280]. Fungal networks are themselves electrically responsive to external stimuli such as wounding and the presence of food sources [281]. A related subject made famous by a groundbreaking publication [282] and a bestselling popular-science book [283] is the so-called Wood Wide Web: the sharing of resources among interconnected forest trees via ectomycorrhizal networks, a symbiosis between tree roots and beneficial fungus (which is how most plants are able to take up nutrients) [284]. Due to the difficulty of isolating such networks from the conductive soil of the forest floor, magnetometry may offer unique advantages in studying electrical activity within forest ecosystems.

5.2 From plants to batteries and beyond

The versatility of the ZULF-NMR spectrometer presented in Ch. 4 has enabled diverse studies not limited to the world of plants. Another application is the detection of electrolyte inside metallic battery housing—of great relevance to battery diagnostics but generally impossible with commercial NMR instruments due to skin-depth limitations of the higher-frequency electromagnetic fields involved [285]. As in the tree-leaf work, where trace amounts of water in dehydrating leaves were measured, the gradiometric quadrature detection scheme enabled signal enhancement to a point that signatures from tens of μL of electrolyte could be recorded with relatively high SNR (Fig. 5.3). Moreover, as we saw in Ch. 4, ZULF quadrature detection is able to distinguish between positive and negative resonance frequencies and thereby determine the absolute sign of gyromagnetic ratios. Fundamental studies of ^{13}C-labeled molecules in solution (Fig. 5.4) demonstrate the power of quadrature detection to simplify ZULF spectra and offer richer information about spin systems and their evolution [268]. Of course, there is still much to explore in the realm of plant-based (ZULF) NMR, not limited to experiments involving thermal

Figure 5.1: Photo collage showcasing exploratory work in plant and fungal bioelectromagnetism. Clockwise from top center: monitoring the electrical response in the stem of sunflower (*Helianthus annuus*) after leaf burning; simultaneous electrode and magnetic monitoring of a tomato plant (*Solanum pseudocapsicum*) prior to leaf cutting, inside a magnetically shielded room at University College London (OPM-MEG helmet also pictured); simultaneous electrode and magnetic monitoring of a paprika plant (*Capsicum annuum*) inside a tabletop magnetic shield (Fig. 5.2); electrophysiological study of oyster-mushroom (*Pleurotus ostreatus*) mycelium subjected to hydrochloric acid and flames; measuring the roots of beech trees (*Fagus sylvatica*) in the Bavarian forest with an atomic gradiometer (Twinleaf OMG).

polarization. Hyperpolarization techniques, already generating excitement in fields such as materials science and biomedicine [286], may eventually enable metabolic imaging of various biochemical processes in living plants. The sun is only just rising on the twin empires of plant biomagnetism and magnetic resonance, and the best is yet to come!

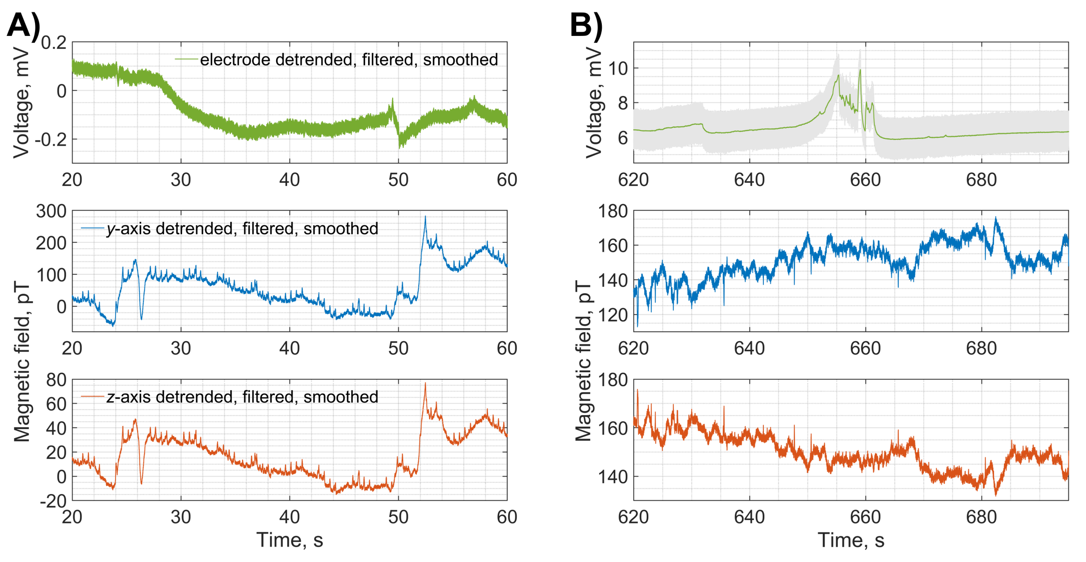

Figure 5.2: Preliminary Mainz data displaying simultaneous electrode (green) and magnetometer time traces (blue and orange) from a paprika plant (*Capsicum annuum*) inside a tabletop magnetic shield (Twinleaf MS-2) open at one end, as pictured in Fig. 5.2. Under the hypothesis that electrical signals propagate along the plant stems, the live electrode was attached to a stem and the ground electrode inserted into the soil; the y- and z- sensitive axes of the QuSpin magnetometer were transverse and radial to the stem, respectively. Efforts were made to avoid mechanical coupling of the plant and magnetometer. All time traces were acquired at approximately 2 kHz sampling rate and processed equivalently, with removal of a linear trend and application of a 50 Hz low-pass filter and 60 ms moving average; the gray trace shows an example of raw data without filtering or smoothing. Note different scalings of the vertical axis in each plot. **A)** Time traces recorded after placing the plant into the magnetic shield and setting up sensors. Magnetometer data appears to show repetitive physiological spiking activity, possibly a stress response, on top of a noise background, but this remains to be confirmed through repeated measurements. **B)** Time traces recorded five minutes after burning the tip of the leaf attached to the measured stem with an open flame. Although the magnetic trace appears to register larger overall variations than before the wounding event, it is difficult to distinguish possible physiological signatures from mechanical and environmental noise. We zoom in on a time window centered on a packet of higher-frequency oscillations in the electrode trace, a characteristic post-wounding response. Interestingly, a simultaneous higher-frequency region is observed in both magnetic traces. Conducting this type of measurement inside a shielded room, rather than a tabletop shield, should enable more conclusive results through suppression of noise sources.

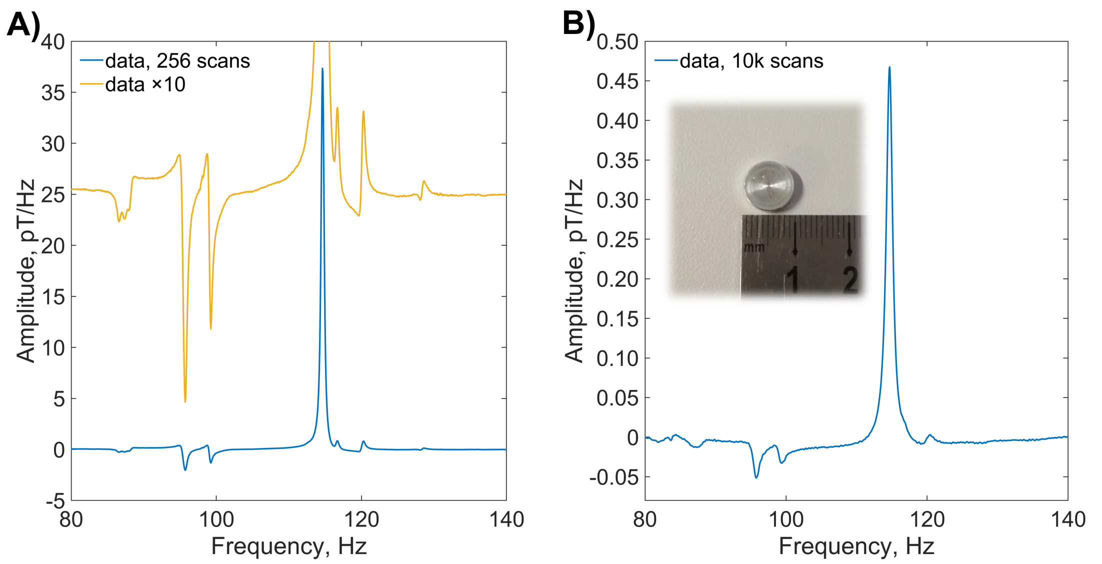

Figure 5.3: Ultralow-field NMR spectra of a common electrolyte used in lithium-ion batteries, $LiPF_6$ salt dissolved in ethylene carbonate (EC) and dimethyl carbonate (DMC), measured at a 2.7 µT background magnetic field. **A)** Measured electrolyte signature from a 1.5 mL vial of 2 M $LiPF_6$ in 50:50 EC/DMC. The largest peak at 115 Hz is due to Larmor precession of solvent protons. The other six peaks/manifolds arise from transitions between PF_6^- energy levels defined both by J-couplings (indirect spin-spin couplings mediated by the electrons shared in chemical bonds) and by Zeeman interactions with the external field [285]. **B)** Measured electrolyte signature from an aluminum battery enclosure (inset) containing approximately 70 µL of a $\sim$ 2.5 M solution of $LiPF_6$ in 50:50 EC/DMC. A method for precise quantification of electrolyte concentrations using recorded battery spectra is described in [285].

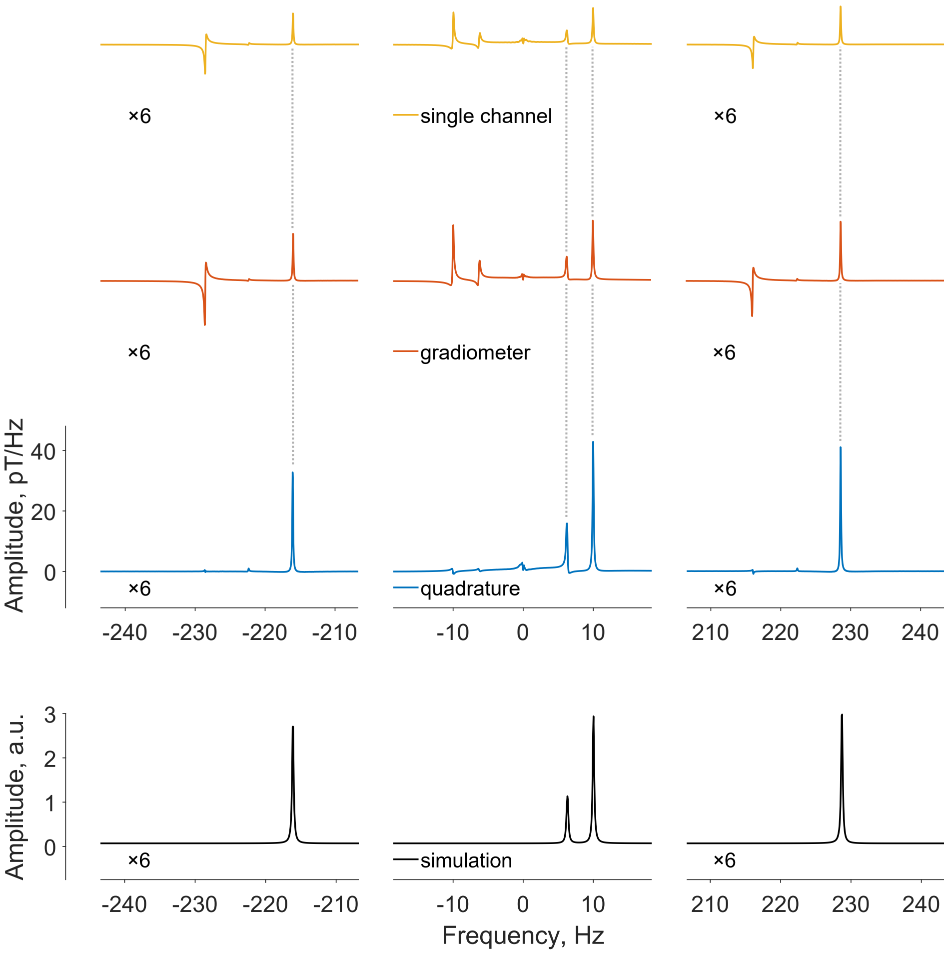

Figure 5.4: Example experimental (colored traces) and simulated (black traces) ULF-NMR spectra of ^{13}C-labeled formic acid ($^{13}CH_2O_2$) for multiple detection geometries, see Figs. 4.1–4.2. The central column shows the near-zero-frequency spectrum arising from Larmor precession of the CH and OH groups in the 230 nT background field; peaks appear at positive frequencies in the quadrature traces due to the positive gyromagnetic ratios of the spin systems. The left and right columns show the J-spectrum arising from J-coupling of the ^{13}C and ^{1}H spins, split due to the nonzero field into a counterrotating doublet centered around ±222 Hz. Application of different magnetic-field pulses allows for creation of various magnetization states with unique spectral signatures [268].

Bibliography

[1] Dmitry Budker and Michael Romalis. “Optical magnetometry”. In: *Nature Physics* 3 (4 Apr. 2007), pp. 227–234. ISSN: 1745-2473. DOI: 10.1038/nphys566.

[2] Evgenii B. Aleksandrov and Anton K. Vershovskii. “Modern radio-optical methods in quantum magnetometry”. In: *Physics-Uspekhi* 52 (6 June 2009), pp. 573–601. ISSN: 1063-7869. DOI: 10.3367/UFNe.0179.200906f.0605.

[3] Dmitry Budker and Derek F. Jackson Kimball, eds. *Optical Magnetometry*. Cambridge University Press, Mar. 2013. ISBN: 9781107010352. DOI: 10.1017/CBO9780511846380.

[4] Antoine Weis, Georg Bison, and Zoran D. Grujić. “Magnetic resonance based atomic magnetometers”. In: *High Sensitivity Magnetometers. Smart Sensors, Measurement and Instrumentation*. Ed. by Asaf Grosz, Michael J. Haji-Sheikh, and Subhas C. Mukhopadhyay. Vol. 19. Springer International Publishing, 2017. Chap. 13, pp. 361–424. ISBN: 9783319340685. DOI: 10.1007/978-3-319-34070-8_13.

[5] Tim M. Tierney et al. “Optically pumped magnetometers: From quantum origins to multi-channel magnetoencephalography”. In: *NeuroImage* 199 (Oct. 2019), pp. 598–608. ISSN: 10538119. DOI: 10.1016/j.neuroimage.2019.05.063.

[6] Kai-Mei C. Fu et al. “Sensitive magnetometry in challenging environments”. In: *AVS Quantum Science* 2 (4 Dec. 2020), p. 044702. ISSN: 2639-0213. DOI: 10.1116/5.0025186.

[7] Michael V. Romalis. “Optically pumped magnetometers for biomagnetic measurements”. In: *Flexible High Performance Magnetic Field Sensors*. Ed. by Etienne Labyt, Tilmann Sander, and Ronald Wakai. Springer International Publishing, Aug. 2022. Chap. 1, pp. 3–15. ISBN: 9783031053634. DOI: 10.1007/978-3-031-05363-4_1.

[8] Roswitha Wiltschko, Christine Nießner, and Wolfgang Wiltschko. “The magnetic compass of birds: The role of cryptochrome”. In: *Frontiers in Physiology* 12 (May 2021), p. 667000. ISSN: 1664-042X. DOI: 10.3389/fphys.2021.667000.

[9] Jingjing Xu et al. “Magnetic sensitivity of cryptochrome 4 from a migratory songbird”. In: *Nature* 594 (7864 June 2021), pp. 535–540. ISSN: 0028-0836. DOI: 10.1038/s41586-021-03618-9.

[10] James L. Gould. “Animal navigation: The evolution of magnetic orientation”. In: *Current Biology* 18 (11 June 2008), R482–R484. ISSN: 09609822. DOI: 10.1016/j.cub.2008.03.052.

[11] Hans Aschenbrenner and Georg Goubau. “Eine Anordnung zur Registrierung rascher Magnetischer Störungen”. In: *Hochfreq. Electroakustik* 47 (6 1936), pp. 177–181.

[12] Michal Janosek. "Parallel fluxgate magnetometers". In: *High Sensitivity Magnetometers. Smart Sensors, Measurement and Instrumentation.* Ed. by Asaf Grosz, Michael J. Haji-Sheikh, and Subhas C. Mukhopadhyay. Vol. 19. Springer International Publishing, 2017. Chap. 17, pp. 41–61. ISBN: 9783319340685. DOI: `10.1007/978-3-319-34070-8_2`.

[13] Nikolay Koshev et al. "Evolution of MEG: A first MEG-feasible fluxgate magnetometer". In: *Human Brain Mapping* 42 (15 Oct. 2021), pp. 4844–4856. ISSN: 1065-9471. DOI: `10.1002/hbm.25582`.

[14] G. S. Waters and P. D. Francis. "A nuclear magnetometer". In: *Journal of Scientific Instruments* 35 (3 Mar. 1958), pp. 88–93. ISSN: 09507671. DOI: `10.1088/0950-7671/35/3/302`.

[15] Arnold L. Bloom. "Principles of operation of the rubidium vapor magnetometer". In: *Applied Optics* 1 (1 Jan. 1962), p. 61. ISSN: 0003-6935. DOI: `10.1364/AO.1.000061`.

[16] R. C. Jaklevic et al. "Quantum interference effects in Josephson tunneling". In: *Physical Review Letters* 12 (7 Feb. 1964), pp. 159–160. ISSN: 0031-9007. DOI: `10.1103/PhysRevLett.12.159`.

[17] C. N. Owston. "A Hall effect magnetometer for small magnetic fields". In: *Journal of Scientific Instruments* 44 (9 Sept. 1967), pp. 798–800. ISSN: 0950-7671. DOI: `10.1088/0950-7671/44/9/441`.

[18] H. Hoffmann, F. Hofmann, and W. Schoepe. "Magnetoresistance and non-Ohmic conductivity of thin platinum films at low temperatures". In: *Physical Review B* 25 (8 Apr. 1982), pp. 5563–5565. ISSN: 0163-1829. DOI: `10.1103/PhysRevB.25.5563`.

[19] Asaf Grosz, Michael J. Haji-Sheikh, and Subhas C. Mukhopadhyay, eds. *High Sensitivity Magnetometers.* Vol. 19. Springer International Publishing, 2017. ISBN: 9783319340685. DOI: `10.1007/978-3-319-34070-8`.

[20] Kasper Jensen, Pauli Kehayias, and Dmitry Budker. "Magnetometry with nitrogen-vacancy centers in diamond". In: *High Sensitivity Magnetometers. Smart Sensors, Measurement and Instrumentation.* Ed. by Asaf Grosz, Michael J. Haji-Sheikh, and Subhas C. Mukhopadhyay. Vol. 19. Springer International Publishing, 2017. Chap. 18, pp. 553–576. ISBN: 9783319340685. DOI: `10.1007/978-3-319-34070-8_18`.

[21] Tilmann Sander et al. "Optically pumped magnetometers enable a new level of biomagnetic measurements". In: *Advanced Optical Technologies* 9 (5 Nov. 2020), pp. 247–251. ISSN: 2192-8584. DOI: `10.1515/aot-2020-0027`.

[22] Margo Batie et al. "Detection of fetal arrhythmia by using optically pumped magnetometers". In: *JACC: Clinical Electrophysiology* 4 (2 Feb. 2018), pp. 284–287. ISSN: 2405500X. DOI: `10.1016/j.jacep.2017.08.009`.

[23] N. V. Nardelli et al. "A conformal array of microfabricated optically-pumped first-order gradiometers for magnetoencephalography". In: *EPJ Quantum Technology* 7 (1 Dec. 2020), p. 11. ISSN: 2662-4400. DOI: `10.1140/epjqt/s40507-020-00086-4`.

[24] Kasper Jensen et al. "Magnetocardiography on an isolated animal heart with a room-temperature optically pumped magnetometer". In: *Scientific Reports* 8 (1 Nov. 2018), p. 16218. ISSN: 2045-2322. DOI: `10.1038/s41598-018-34535-z`.

[25] W. Gawlik and J. M. Higbie. “Magnetometry with cold atoms”. In: *Optical Magnetometry*. Ed. by Dmitry Budker and Derek F. Jackson Kimball. Cambridge University Press, Mar. 2013. Chap. 9, pp. 167–189. ISBN: 9780511846380. DOI: 10.1017/CBO9780511846380.010.

[26] Yuval Cohen et al. “A cold atom radio-frequency magnetometer”. In: *Applied Physics Letters* 114 (7 Feb. 2019), p. 073505. ISSN: 0003-6951. DOI: 10.1063/1.5084004.

[27] Werner Heil. “Helium magnetometers”. In: *High Sensitivity Magnetometers. Smart Sensors, Measurement and Instrumentation.* Ed. by A. Grosz, M. Haji-Sheikh, and S. Mukhopadhyay. Vol. 19. Springer, 2017. Chap. 16, pp. 493–521. ISBN: 9783319340685. DOI: 10.1007/978-3-319-34070-8_16.

[28] William Fourcault et al. “Helium-4 magnetometers for room-temperature biomedical imaging: toward collective operation and photon-noise limited sensitivity”. In: *Optics Express* 29 (10 May 2021), p. 14467. ISSN: 1094-4087. DOI: 10.1364/OE.420031.

[29] F. Bertrand et al. “A ^{4}He vector zero-field optically pumped magnetometer operated in the Earth-field”. In: *Review of Scientific Instruments* 92 (10 Oct. 2021), p. 105005. ISSN: 0034-6748. DOI: 10.1063/5.0062791.

[30] Gwenael Le Gal, Laure-Line Rouve, and Agustin Palacios-Laloy. “Parametric resonance magnetometer based on elliptically polarized light yielding three-axis measurement with isotropic sensitivity”. In: *Applied Physics Letters* 118 (25 June 2021), p. 254001. ISSN: 0003-6951. DOI: 10.1063/5.0047124.

[31] Jean-Michel Léger et al. “In-flight performance of the Absolute Scalar Magnetometer vector mode on board the Swarm satellites”. In: *Earth, Planets and Space* 67 (1 Dec. 2015), p. 57. ISSN: 1880-5981. DOI: 10.1186/s40623-015-0231-1.

[32] A. Maul et al. “Nuclear hyperpolarization of ^{3}He by magnetized plasmas”. In: *Physical Review A* 98 (6 Dec. 2018), p. 063405. ISSN: 2469-9926. DOI: 10.1103/PhysRevA.98.063405.

[33] Anna Nikiel et al. “Ultrasensitive ^{3}He magnetometer for measurements of high magnetic fields”. In: *The European Physical Journal D* 68 (11 Nov. 2014), p. 330. ISSN: 1434-6060. DOI: 10.1140/epjd/e2014-50401-3.

[34] M. E. Limes, D. Sheng, and M. V. Romalis. “^{3}He-^{129}Xe comagnetometery using ^{87}Rb detection and decoupling”. In: *Physical Review Letters* 120 (3 Jan. 2018), p. 033401. ISSN: 0031-9007. DOI: 10.1103/PhysRevLett.120.033401.

[35] Min Jiang et al. “Floquet maser”. In: *Science Advances* 7 (8 Feb. 2021), pp. 719–736. ISSN: 2375-2548. DOI: 10.1126/sciadv.abe0719.

[36] A. Palacios-Laloy, M. Le Prado, and E. Labyt. *Flexible High Performance Magnetic Field Sensors*. Ed. by Etienne Labyt, Tilmann Sander, and Ronald Wakai. Springer International Publishing, 2022, pp. 79–110. ISBN: 978-3-031-05362-7. DOI: 10.1007/978-3-031-05363-4.

[37] Sun Yool Park. “Construction of a Single Beam SERF Magnetometer using Potassium Atoms for GNOME”. Oberlin College, Apr. 2019. URL: https://www.oberlin.edu/sites/default/files/content/arts-and-sciences/departments/physics/student_projects/sunyool-park_thesis_3.0.pdf.

[38] W. A. Terrano and M. V. Romalis. “Comagnetometer probes of dark matter and new physics”. In: *Quantum Science and Technology* 7 (1 Jan. 2022), p. 014001. ISSN: 2058-9565. DOI: 10.1088/2058-9565/ac1ae0.

[39] Mikhail Padniuk et al. “Response of atomic spin-based sensors to magnetic and nonmagnetic perturbations”. In: *Scientific Reports* 12 (1 Jan. 2022), p. 324. ISSN: 2045-2322. DOI: 10.1038/s41598-021-03609-w.

[40] Haowen Su et al. “Search for exotic spin-dependent interactions with a spin-based amplifier”. In: *Science Advances* 7 (47 Nov. 2021), p. 9535. ISSN: 2375-2548. DOI: 10.1126/sciadv.abi9535.

[41] Dmitry Budker, Derek F. Kimball, and David P. Demille. *Atomic Physics: An Exploration Through Problems and Solutions*. 2nd ed. Oxford University Press, July 2008. ISBN: 9780199532414. URL: https://global.oup.com/academic/product/atomic-physics-9780199532414.

[42] Marcis Auzinsh, Dmitry Budker, and Simon Rochester. *Optically Polarized Atoms: Understanding Light-Atom Interactions*. Oxford University Press, July 2010. ISBN: 9780199565122. URL: https://global.oup.com/academic/product/optically-polarized-atoms-9780199565122.

[43] Hans Marin Florez and Tadas Pyragius. “Floquet description of optically pumped magnetometers”. In: *Physical Review A* 103 (3 Mar. 2021), p. 033113. ISSN: 2469-9926. DOI: 10.1103/PhysRevA.103.033113.

[44] Brian Julsgaard. “Entanglement and Quantum Interactions with Macroscopic Gas Samples”. PhD thesis. Center for Quantum Optics (QUANTOP), University of Aarhus, Oct. 2003. URL: https://phys.au.dk/fileadmin/site_files/publikationer/phd/Brian_Julsgaard.pdf.

[45] C. Cohen-Tannoudji et al. “Detection of the static magnetic field produced by the oriented nuclei of optically pumped ^{3}He gas”. In: *Physical Review Letters* 22 (15 Apr. 1969), pp. 758–760. ISSN: 0031-9007. DOI: 10.1103/PhysRevLett.22.758.

[46] G. G. Scott. “Review of gyromagnetic ratio experiments”. In: *Reviews of Modern Physics* 34 (1 Jan. 1962), pp. 102–109. ISSN: 0034-6861. DOI: 10.1103/RevModPhys.34.102.

[47] S. M. Rochester et al. “Orientation-to-alignment conversion and spin squeezing”. In: *Physical Review A* 85 (2 Feb. 2012), p. 022125. ISSN: 1050-2947. DOI: 10.1103/PhysRevA.85.022125.

[48] William Happer. “Optical pumping”. In: *Reviews of Modern Physics* 44 (2 Apr. 1972), pp. 169–249. ISSN: 0034-6861. DOI: 10.1103/RevModPhys.44.169.

[49] M. Auzinsh et al. “F-resolved magneto-optical resonances in the D_1 excitation of cesium: Experiment and theory”. In: *Physical Review A* 78 (1 July 2008), p. 013417. ISSN: 1050-2947. DOI: 10.1103/PhysRevA.78.013417.

[50] Alexander Pouliot et al. “Investigations of optical pumping for magnetometry using an auto-locking laser system”. In: *Laser Technology for Defense and Security XIV*. Ed. by Mark Dubinskiy and Timothy C. Newell. Vol. 10637. SPIE, May 2018, p. 9. ISBN: 9781510617858. DOI: 10.1117/12.2304598.

[51] Daniel A. Steck. *Alkali D Line Data*. 2021. URL: https://steck.us/alkalidata/.

[52] Karl Blum. *Density Matrix Theory and Applications*. Vol. 64. Springer Berlin Heidelberg, 2012. ISBN: 978-3-642-20560-6. DOI: 10.1007/978-3-642-20561-3.

[53] Peter W. Milonni and Joseph H. Eberly. *Laser Physics*. Wiley, Mar. 2010. ISBN: 9780470387719. DOI: 10.1002/9780470409718.

[54] I. K. Kominis et al. “A subfemtotesla multichannel atomic magnetometer”. In: *Nature* 422 (6932 Apr. 2003), pp. 596–599. ISSN: 0028-0836. DOI: 10.1038/nature01484.

[55] A. Kuzmich, Klaus Mølmer, and E. S. Polzik. “Spin squeezing in an ensemble of atoms illuminated with squeezed Light”. In: *Physical Review Letters* 79 (24 Dec. 1997), pp. 4782–4785. ISSN: 0031-9007. DOI: 10.1103/PhysRevLett.79.4782.

[56] M. Auzinsh et al. “Can a quantum nondemolition measurement improve the sensitivity of an atomic magnetometer?” In: *Physical Review Letters* 93 (17 Oct. 2004), p. 173002. ISSN: 0031-9007. DOI: 10.1103/PhysRevLett.93.173002.

[57] Florian Wolfgramm et al. “Squeezed-light optical magnetometry”. In: *Physical Review Letters* 105 (5 July 2010), p. 053601. ISSN: 0031-9007. DOI: 10.1103/PhysRevLett.105.053601.

[58] R. J. Sewell et al. “Magnetic sensitivity beyond the projection noise limit by spin squeezing”. In: *Physical Review Letters* 109 (25 Dec. 2012), p. 253605. ISSN: 0031-9007. DOI: 10.1103/PhysRevLett.109.253605.

[59] Travis Horrom et al. “Quantum-enhanced magnetometer with low-frequency squeezing”. In: *Physical Review A* 86 (2 Aug. 2012), p. 023803. ISSN: 1050-2947. DOI: 10.1103/PhysRevA.86.023803.

[60] C. Troullinou et al. “Squeezed-light enhancement and backaction evasion in a high sensitivity optically pumped magnetometer”. In: *Physical Review Letters* 127 (19 Nov. 2021), p. 193601. ISSN: 0031-9007. DOI: 10.1103/PhysRevLett.127.193601. URL: https://link.aps.org/doi/10.1103/PhysRevLett.127.193601.

[61] Jiahui Li and Irina Novikova. “Improving sensitivity of an amplitude-modulated magneto-optical atomic magnetometer using squeezed light”. In: *Journal of the Optical Society of America B* 39 (11 Nov. 2022), p. 2998. ISSN: 0740-3224. DOI: 10.1364/JOSAB.471677.

[62] W. Wasilewski et al. “Quantum noise limited and entanglement-assisted magnetometry”. In: *Physical Review Letters* 104 (13 Mar. 2010), p. 133601. ISSN: 0031-9007. DOI: 10.1103/PhysRevLett.104.133601.

[63] G. Vasilakis, V. Shah, and M. V. Romalis. “Stroboscopic backaction evasion in a dense alkali-metal vapor”. In: *Physical Review Letters* 106 (14 Apr. 2011), p. 143601. ISSN: 0031-9007. DOI: 10.1103/PhysRevLett.106.143601.

[64] Mark Fox. *Quantum Optics: An Introduction.* Oxford University Press, Apr. 2006. ISBN: 9780198566724. URL: https://global.oup.com/academic/product/quantum-optics-9780198566724.

[65] M. A. Bouchiat and J. Brossel. “Relaxation of optically pumped Rb atoms on paraffin-coated walls”. In: *Physical Review* 147 (1 July 1966), pp. 41–54. ISSN: 0031-899X. DOI: 10.1103/PhysRev.147.41.

[66] Theo Scholtes et al. “Intrinsic relaxation rates of polarized Cs vapor in miniaturized cells”. In: *Applied Physics B* 117 (1 Oct. 2014), pp. 211–218. ISSN: 0946-2171. DOI: 10.1007/s00340-014-5824-z.

[67] D. Sheng et al. “Subfemtotesla scalar atomic magnetometry using multipass cells”. In: *Physical Review Letters* 110 (16 Apr. 2013), p. 160802. ISSN: 0031-9007. DOI: 10.1103/PhysRevLett.110.160802.

[68] G. Vasilakis et al. "Cavity enhanced quantum limited magnetometry". In: *Research in Optical Sciences*. OSA, Mar. 2014, QTu3B.6. ISBN: 978-1-55752-995-4. DOI: `10.1364/QIM.2014.QTu3B.6`.

[69] B. Cai et al. "Herriott-cavity-assisted all-optical atomic vector magnetometer". In: *Physical Review A* 101 (5 May 2020), p. 053436. ISSN: 2469-9926. DOI: `10.1103/PhysRevA.101.053436`.

[70] V. G. Lucivero et al. "Femtotesla direct magnetic gradiometer using a single multipass cell". In: *Physical Review Applied* 15 (1 Jan. 2021), p. 014004. ISSN: 2331-7019. DOI: `10.1103/PhysRevApplied.15.014004`.

[71] David W. Allan. *The Allan Variance*. URL: `http://www.allanstime.com/AllanVariance/index.html`.

[72] Jason Mora et al. "Measurement of the Ratio between g-Factors of the Ground States of ^{87}Rb and ^{85}Rb". In: *Annalen der Physik* 531 (5 May 2019), p. 1800281. ISSN: 0003-3804. DOI: `10.1002/andp.201800281`.

[73] Evgeny B. Alexandrov. "Optically pumped atomic magnetometers after three decades". In: *Optical Engineering* 31 (4 Apr. 1992), p. 711. ISSN: 00913286. DOI: `10.1117/12.56132`.

[74] S. Groeger et al. "A high-sensitivity laser-pumped M$_x$ magnetometer". In: *The European Physical Journal D* 38 (2 May 2006), pp. 239–247. ISSN: 1434-6060. DOI: `10.1140/epjd/e2006-00037-y`.

[75] E. B. Aleksandrov et al. "Laser pumping in the scheme of an Mx-magnetometer". In: *Optics and Spectroscopy (English translation of Optika i Spektroskopiya)* 78 (2 1995), pp. 292–298. ISSN: 0030400X.

[76] Valentina Tiporlini and Kamal Alameh. "High sensitivity optically pumped quantum magnetometer". In: *The Scientific World Journal* 2013 (2013), pp. 1–8. ISSN: 1537-744X. DOI: `10.1155/2013/858379`.

[77] J. C. Allred et al. "High-sensitivity atomic magnetometer unaffected by spin-exchange relaxation". In: *Physical Review Letters* 89 (13 Sept. 2002), p. 130801. ISSN: 0031-9007. DOI: `10.1103/PhysRevLett.89.130801`.

[78] William E. Bell and Arnold L. Bloom. "Optically driven spin precession". In: *Physical Review Letters* 6 (6 Mar. 1961), pp. 280–281. ISSN: 0031-9007. DOI: `10.1103/PhysRevLett.6.280`.

[79] Jundi Li et al. "SERF atomic magnetometer-Recent advances and applications: A review". In: *IEEE Sensors Journal* 18 (20 Oct. 2018), pp. 8198–8207. ISSN: 1530-437X. DOI: `10.1109/JSEN.2018.2863707`.

[80] D. Budker et al. "Sensitive magnetometry based on nonlinear magneto-optical rotation". In: *Physical Review A* 62 (4 Sept. 2000), p. 043403. ISSN: 1050-2947. DOI: `10.1103/PhysRevA.62.043403`.

[81] D. Budker et al. "Resonant nonlinear magneto-optical effects in atoms". In: *Reviews of Modern Physics* 74 (4 Nov. 2002), pp. 1153–1201. ISSN: 0034-6861. DOI: `10.1103/RevModPhys.74.1153`.

[82] M. Rosner et al. "A highly drift-stable atomic magnetometer for fundamental physics experiments". In: *Applied Physics Letters* 120 (16 Apr. 2022), p. 161102. ISSN: 0003-6951. DOI: `10.1063/5.0083854`.

[83] D. Budker et al. "Nonlinear magneto-optical rotation with frequency-modulated light". In: *Physical Review A* 65 (5 May 2002), p. 055403. ISSN: 1050-2947. DOI: `10.1103/PhysRevA.65.055403`.

[84] W. Gawlik et al. "Nonlinear magneto-optical rotation with amplitude modulated light". In: *Applied Physics Letters* 88 (13 Mar. 2006), p. 131108. ISSN: 0003-6951. DOI: `10.1063/1.2190457`.

[85] A. Nagel et al. "Experimental realization of coherent dark-state magnetometers". In: *Europhysics Letters (EPL)* 44 (1 Oct. 1998), pp. 31–36. ISSN: 0295-5075. DOI: `10.1209/epl/i1998-00430-0`.

[86] M. Stähler et al. "Picotesla magnetometry with coherent dark states". In: *Europhysics Letters (EPL)* 54 (3 May 2001), pp. 323–328. ISSN: 0295-5075. DOI: `10.1209/epl/i2001-00245-y`.

[87] Volkmar Schultze et al. "An Optically Pumped Magnetometer Working in the Light-Shift Dispersed M_z Mode". In: *Sensors* 17 (3 Mar. 2017), p. 561. ISSN: 1424-8220. DOI: `10.3390/s17030561`.

[88] Giuseppe Bevilacqua et al. "Self-adaptive loop for external-disturbance reduction in a differential measurement setup". In: *Physical Review Applied* 11 (1 Jan. 2019), p. 014029. ISSN: 2331-7019. DOI: `10.1103/PhysRevApplied.11.014029`.

[89] Rui Zhang et al. "Recording brain activities in unshielded Earth's field with optically pumped atomic magnetometers". In: *Science Advances* 6 (24 June 2020), pp. 8792–8804. ISSN: 2375-2548. DOI: `10.1126/sciadv.aba8792`.

[90] Yucheng Yang et al. "All-optical single-species cesium atomic comagnetometer with optical free induction decay detection". In: *Applied Physics B: Lasers and Optics* 127 (3 Mar. 2021), pp. 1–11. ISSN: 09462171. DOI: `10.1007/s00340-021-07594-w`.

[91] H. B. Dang, A. C. Maloof, and M. V. Romalis. "Ultrahigh sensitivity magnetic field and magnetization measurements with an atomic magnetometer". In: *Applied Physics Letters* 97 (15 Oct. 2010), p. 151110. ISSN: 0003-6951. DOI: `10.1063/1.3491215`.

[92] Vito Giovanni Lucivero et al. "Shot-noise-limited magnetometer with sub-picotesla sensitivity at room temperature". In: *Review of Scientific Instruments* 85 (11 Nov. 2014), p. 113108. ISSN: 0034-6748. DOI: `10.1063/1.4901588`.

[93] Andrey B. Matsko, Dmitry Strekalov, and Lute Maleki. "Magnetometer based on the opto-electronic microwave oscillator". In: *Optics Communications* 247 (1-3 Mar. 2005), pp. 141–148. ISSN: 00304018. DOI: `10.1016/j.optcom.2004.11.047`.

[94] S. Groeger et al. "Laser-pumped cesium magnetometers for high-resolution medical and fundamental research". In: *Sensors and Actuators A: Physical* 129 (1-2 May 2006), pp. 1–5. ISSN: 09244247. DOI: `10.1016/j.sna.2005.09.036`.

[95] V. Shah, G. Vasilakis, and M. V. Romalis. "High bandwidth atomic magnetometery with continuous quantum nondemolition measurements". In: *Physical Review Letters* 104 (1 Jan. 2010), p. 013601. ISSN: 0031-9007. DOI: `10.1103/PhysRevLett.104.013601`.

[96] Vishal Shah et al. "Subpicotesla atomic magnetometry with a microfabricated vapour cell". In: *Nature Photonics* 1 (11 Nov. 2007), pp. 649–652. ISSN: 1749-4885. DOI: `10.1038/nphoton.2007.201`.

[97] Rujie Li et al. “Continuous high-sensitivity and high-bandwidth atomic magnetometer”. In: *Physical Review Applied* 14 (6 Dec. 2020), p. 064067. ISSN: 2331-7019. DOI: `10.1103/PhysRevApplied.14.064067`.

[98] J. Belfi et al. “Cesium coherent population trapping magnetometer for cardiosignal detection in an unshielded environment”. In: *Journal of the Optical Society of America B* 24 (9 Sept. 2007), p. 2357. ISSN: 0740-3224. DOI: `10.1364/JOSAB.24.002357`.

[99] Kiyoshi Ishikawa. “High-temperature lithium atomic magnetometry by symmetric hyperfine coherent population trapping resonances”. In: *Journal of the Optical Society of America B* 38 (7 July 2021), p. 2155. ISSN: 0740-3224. DOI: `10.1364/JOSAB.423749`.

[100] Hongying Yang et al. “High bandwidth three-axis magnetometer based on optically polarized ^{8}5Rb under unshielded environment”. In: *Journal of Physics D: Applied Physics* 53 (6 Feb. 2020), p. 065002. ISSN: 0022-3727. DOI: `10.1088/1361-6463/ab541a`.

[101] H. C. Huang et al. “Three-axis atomic magnetometer based on spin precession modulation”. In: *Applied Physics Letters* 107 (18 Nov. 2015), p. 182403. ISSN: 0003-6951. DOI: `10.1063/1.4935096`.

[102] Zhichao Ding, Jie Yuan, and Xingwu Long. “Response of a Bell-Bloom magnetometer to a magnetic field of arbitrary direction”. In: *Sensors* 18 (5 May 2018), p. 1401. ISSN: 1424-8220. DOI: `10.3390/s18051401`.

[103] S. J. Seltzer and M. V. Romalis. “Unshielded three-axis vector operation of a spin-exchange-relaxation-free atomic magnetometer”. In: *Applied Physics Letters* 85 (20 Nov. 2004), pp. 4804–4806. ISSN: 0003-6951. DOI: `10.1063/1.1814434`.

[104] Aram Papoyan et al. “Magnetic-field-compensation optical vector magnetometer”. In: *Applied Optics* 55 (4 Feb. 2016), p. 892. ISSN: 0003-6935. DOI: `10.1364/AO.55.000892`.

[105] B. Patton et al. “All-optical vector atomic magnetometer”. In: *Physical Review Letters* 113 (1 July 2014), p. 013001. ISSN: 0031-9007. DOI: `10.1103/PhysRevLett.113.013001`.

[106] Tadas Pyragius, Hans Marin Florez, and Thomas Fernholz. “Voigt-effect-based three-dimensional vector magnetometer”. In: *Physical Review A* 100 (2 Aug. 2019), p. 023416. ISSN: 2469-9926. DOI: `10.1103/PhysRevA.100.023416`.

[107] V. I. Yudin et al. “Vector magnetometry based on electromagnetically induced transparency in linearly polarized light”. In: *Physical Review A* 82 (3 Sept. 2010), p. 033807. ISSN: 1050-2947. DOI: `10.1103/PhysRevA.82.033807`.

[108] Haje Korth et al. “Miniature atomic scalar magnetometer for space based on the rubidium isotope ^{87}Rb”. In: *Journal of Geophysical Research: Space Physics* 121 (8 Aug. 2016), pp. 7870–7880. ISSN: 2169-9380. DOI: `10.1002/2016JA022389`.

[109] G. Oelsner et al. “Integrated optically pumped magnetometer for measurements within Earth’s magnetic field”. In: *Physical Review Applied* 17 (2 Feb. 2022), p. 024034. ISSN: 2331-7019. DOI: `10.1103/PhysRevApplied.17.024034`.

[110] Peter D. D. Schwindt et al. “Chip-scale atomic magnetometer with improved sensitivity by use of the M_x technique”. In: *Applied Physics Letters* 90 (8 Feb. 2007), p. 081102. ISSN: 0003-6951. DOI: `10.1063/1.2709532`.

[111] R. Jimenez-Martinez et al. “Sensitivity comparison of Mx and frequency-modulated Bell-Bloom Cs magnetometers in a microfabricated cell”. In: *IEEE Transactions on Instrumentation and Measurement* 59 (2 Feb. 2010), pp. 372–378. ISSN: 0018-9456. DOI: `10.1109/TIM.2009.2023829`.

[112] Vladislav Gerginov, Sean Krzyzewski, and Svenja Knappe. “Pulsed operation of a miniature scalar optically pumped magnetometer”. In: *Journal of the Optical Society of America B* 34 (7 July 2017), p. 1429. ISSN: 0740-3224. DOI: `10.1364/JOSAB.34.001429`.

[113] Vladislav Gerginov, Marco Pomponio, and Svenja Knappe. “Scalar magnetometry below $100\,\mathrm{fT}/\mathrm{Hz}^{1/2}$ in a microfabricated cell”. In: *IEEE Sensors Journal* 20 (21 Nov. 2020), pp. 12684–12690. ISSN: 1530-437X. DOI: `10.1109/JSEN.2020.3002193`.

[114] Jin Zhang et al. “Magnetocardiography measurements by microfabricated atomic magnetometer with a 3-D spherical alkali vapor cell”. In: *IEEE Transactions on Instrumentation and Measurement* 70 (2021), pp. 1–7. ISSN: 0018-9456. DOI: `10.1109/TIM.2021.3120375`.

[115] Yoel Sebbag et al. “Demonstration of an integrated nanophotonic chip-scale alkali vapor magnetometer using inverse design”. In: *Light: Science & Applications* 10 (1 Mar. 2021), p. 54. ISSN: 2047-7538. DOI: `10.1038/s41377-021-00499-5`.

[116] Peter D. D. Schwindt et al. “Chip-scale atomic magnetometer”. In: *Applied Physics Letters* 85 (26 Dec. 2004), pp. 6409–6411. ISSN: 0003-6951. DOI: `10.1063/1.1839274`.

[117] Hyun-Gue Hong et al. “Chip-scale ultra-low field atomic magnetometer based on coherent population trapping”. In: *Sensors* 21 (4 Feb. 2021), p. 1517. ISSN: 1424-8220. DOI: `10.3390/s21041517`.

[118] Jean Brossel and Francis Bitter. “A new "double resonance" method for investigating atomic energy levels. Application to Hg $^3\mathrm{P}_1$”. In: *Physical Review* 86 (3 May 1952), pp. 308–316. ISSN: 0031-899X. DOI: `10.1103/PhysRev.86.308`.

[119] Alan Corney. *Atomic and Laser Spectroscopy.* Oxford University Press, 2006. ISBN: 9780199211456.

[120] J. H. Allen and P. L. Bender. “Narrow line rubidium magnetometer for high accuracy field measurements”. In: *Journal of geomagnetism and geoelectricity* 24 (1 1972), pp. 105–125. ISSN: 0022-1392. DOI: `10.5636/jgg.24.105`.

[121] E. Pulz, K.-H. Jäckel, and H.-J. Linthe. “A new optically pumped tandem magnetometer: principles and experiences”. In: *Measurement Science and Technology* 10 (11 Nov. 1999), pp. 1025–1031. ISSN: 0957-0233. DOI: `10.1088/0957-0233/10/11/309`.

[122] W. Chalupczak et al. “Room temperature femtotesla radio-frequency atomic magnetometer”. In: *Applied Physics Letters* 100 (24 June 2012), p. 242401. ISSN: 0003-6951. DOI: `10.1063/1.4729016`.

[123] Zoran D. Grujić et al. “A sensitive and accurate atomic magnetometer based on free spin precession”. In: *The European Physical Journal D* 69 (5 May 2015), p. 135. ISSN: 1434-6060. DOI: `10.1140/epjd/e2015-50875-3`.

[124] J. Belfi et al. “Dual channel self-oscillating optical magnetometer”. In: *Journal of the Optical Society of America B* 26 (5 May 2009), p. 910. ISSN: 0740-3224. DOI: `10.1364/JOSAB.26.000910`.

[125] James Osborne et al. "Fully integrated, standalone zero field optically pumped magnetometer for biomagnetism". In: *Steep Dispersion Engineering and Opto-Atomic Precision Metrology XI*. Ed. by Selim M. Shahriar and Jacob Scheuer. Vol. 10548. SPIE, Feb. 2018, p. 51. ISBN: 9781510615816. DOI: 10.1117/12.2299197.

[126] Volkmar Schultze et al. "Characteristics and performance of an intensity-modulated optically pumped magnetometer in comparison to the classical M_x magnetometer". In: *Optics Express* 20 (13 June 2012), p. 14201. ISSN: 1094-4087. DOI: 10.1364/OE.20.014201.

[127] Ricardo Jiménez-Martínez et al. "High-bandwidth optical magnetometer". In: *Journal of the Optical Society of America B* 29 (12 Dec. 2012), p. 3398. ISSN: 0740-3224. DOI: 10.1364/JOSAB.29.003398.

[128] G. Bison, R. Wynands, and A. Weis. "Dynamical mapping of the human cardiomagnetic field with a room-temperature, laser-optical sensor". In: *Optics Express* 11 (8 Apr. 2003), p. 904. ISSN: 1094-4087. DOI: 10.1364/OE.11.000904.

[129] Jingwei Sheng et al. "Magnetoencephalography with a Cs-based high-sensitivity compact atomic magnetometer". In: *Review of Scientific Instruments* 88 (9 Sept. 2017). ISSN: 0034-6748. DOI: 10.1063/1.5001730.

[130] Mikhail V. Petrenko et al. "Towards the non-zero field cesium magnetic sensor array for magnetoencephalography". In: *IEEE Sensors Journal* 21 (17 Sept. 2021), pp. 18626–18632. ISSN: 1530-437X. DOI: 10.1109/JSEN.2021.3089455.

[131] Victor Lebedev, Stefan Hartwig, and Thomas Middelmann. "Fast and robust optically pumped cesium magnetometer". In: *Advanced Optical Technologies* 9 (5 Nov. 2020), pp. 275–286. ISSN: 2192-8584. DOI: 10.1515/aot-2020-0024.

[132] Simone Colombo et al. "Towards a mechanical MPI scanner based on atomic magnetometry". In: *International Journal on Magnetic Particle Imaging* 3 (1 2016).

[133] Michael C. D. Tayler et al. "Invited Review Article: Instrumentation for nuclear magnetic resonance in zero and ultralow magnetic field". In: *Review of Scientific Instruments* 88 (9 Sept. 2017), p. 091101. ISSN: 0034-6748. DOI: 10.1063/1.5003347.

[134] Sven Bodenstedt, Morgan W. Mitchell, and Michael C. D. Tayler. "Fast-field-cycling ultralow-field nuclear magnetic relaxation dispersion". In: *Nature Communications* 12 (1 June 2021), p. 4041. ISSN: 2041-1723. DOI: 10.1038/s41467-021-24248-9.

[135] Ethan J. Pratt et al. "Kernel Flux: A whole-head 432-magnetometer optically-pumped magnetoencephalography (OP-MEG) system for brain activity imaging during natural human experiences". In: *Optical and Quantum Sensing and Precision Metrology*. Ed. by Selim M. Shahriar and Jacob Scheuer. Vol. 11700. SPIE, Mar. 2021, p. 101. ISBN: 9781510642355. DOI: 10.1117/12.2581794.

[136] Anna U. Kowalczyk et al. "Detection of human auditory evoked brain signals with a resilient nonlinear optically pumped magnetometer". In: *NeuroImage* 226 (Feb. 2021), p. 117497. ISSN: 10538119. DOI: 10.1016/j.neuroimage.2020.117497.

[137] Amir Borna et al. "A 20-channel magnetoencephalography system based on optically pumped magnetometers". In: *Physics in Medicine & Biology* 62 (23 Nov. 2017), pp. 8909–8923. ISSN: 1361-6560. DOI: 10.1088/1361-6560/aa93d1.

[138] Stuart Ingleby et al. "A digital alkali spin maser". In: *Scientific Reports* 12 (1 July 2022), p. 12888. ISSN: 2045-2322. DOI: 10.1038/s41598-022-16910-z.

[139] G. Oelsner et al. "Sources of heading errors in optically pumped magnetometers operated in the Earth's magnetic field". In: *Physical Review A* 99 (1 Jan. 2019), p. 013420. ISSN: 2469-9926. DOI: `10.1103/PhysRevA.99.013420`.

[140] W. Lee et al. "Heading errors in all-optical alkali-metal-vapor magnetometers in geomagnetic fields". In: *Physical Review A* 103 (6 June 2021), p. 063103. ISSN: 2469-9926. DOI: `10.1103/PhysRevA.103.063103`.

[141] Guzhi Bao et al. "Suppression of the nonlinear zeeman effect and heading error in Earth-field-range alkali-vapor magnetometers". In: *Physical Review Letters* 120 (3 Jan. 2018), p. 033202. ISSN: 0031-9007. DOI: `10.1103/PhysRevLett.120.033202`.

[142] Ricardo Jiménez-Martínez et al. "Signal tracking beyond the time resolution of an atomic sensor by Kalman filtering". In: *Physical Review Letters* 120 (4 Jan. 2018), p. 040503. ISSN: 0031-9007. DOI: `10.1103/PhysRevLett.120.040503`.

[143] Cameron Deans, Luca Marmugi, and Ferruccio Renzoni. "Active underwater detection with an array of atomic magnetometers". In: *Applied Optics* 57 (10 Apr. 2018), p. 2346. ISSN: 1559-128X. DOI: `10.1364/AO.57.002346`.

[144] Armen Sargsyan et al. "Selective reflection from an Rb layer with a thickness below $\lambda/12$ and applications". In: *Optics Letters* 42 (8 Apr. 2017), p. 1476. ISSN: 0146-9592. DOI: `10.1364/OL.42.001476`.

[145] Seth DeVore et al. "Improving student understanding of lock-in amplifiers". In: *American Journal of Physics* 84 (1 Jan. 2016), pp. 52–56. ISSN: 0002-9505. DOI: `10.1119/1.4934957`.

[146] Wenhao Li et al. "Characterization of high-temperature performance of cesium vapor cells with anti-relaxation coating". In: *Journal of Applied Physics* 121 (6 Feb. 2017), p. 063104. ISSN: 0021-8979. DOI: `10.1063/1.4976017`.

[147] A. B. Matsko et al. "Radiation trapping in coherent media". In: *Physical Review Letters* 87 (13 Sept. 2001), p. 133601. ISSN: 0031-9007. DOI: `10.1103/PhysRevLett.87.133601`.

[148] Runqi Han et al. "Is light narrowing possible with dense-vapor paraffin coated cells for atomic magnetometers?" In: *AIP Advances* 7 (12 Dec. 2017), p. 125224. ISSN: 2158-3226. DOI: `10.1063/1.4997691`.

[149] M. P. Ledbetter et al. "Zero-field remote detection of NMR with a microfabricated atomic magnetometer". In: *Proceedings of the National Academy of Sciences* 105 (7 Feb. 2008), pp. 2286–2290. ISSN: 0027-8424. DOI: `10.1073/pnas.0711505105`.

[150] D. V. Brazhnikov et al. "Level-crossing resonances on open atomic transitions in a buffered Cs vapor cell: Linewidth narrowing, high contrast, and atomic magnetometry applications". In: *Physical Review A* 106 (1 July 2022), p. 013113. ISSN: 2469-9926. DOI: `10.1103/PhysRevA.106.013113`.

[151] Kaleb Campbell et al. "Intrinsic Pulsed Magnetic Gradiometer in Earth's Field". In: *arXiv* (Nov. 2021). DOI: `10.48550/arxiv.2111.12310`.

[152] S. Woetzel et al. "Microfabricated atomic vapor cell arrays for magnetic field measurements". In: *Review of Scientific Instruments* 82 (3 Mar. 2011), p. 033111. ISSN: 0034-6748. DOI: `10.1063/1.3559304`.

[153] Sylvain Karlen et al. "Lifetime assessment of RbN_3-filled MEMS atomic vapor cells with Al_2O_3 coating". In: *Optics Express* 25 (3 Feb. 2017), p. 2187. ISSN: 1094-4087. DOI: `10.1364/OE.25.002187`.

[154] R. Vicarini et al. “Demonstration of the mass-producible feature of a Cs vapor microcell technology for miniature atomic clocks”. In: *Sensors and Actuators A: Physical* 280 (Sept. 2018), pp. 99–106. ISSN: 09244247. DOI: `10.1016/j.sna.2018.07.032`.

[155] Kasper Jensen et al. “Non-invasive detection of animal nerve impulses with an atomic magnetometer operating near quantum limited sensitivity”. In: *Scientific Reports* 6 (1 July 2016), p. 29638. ISSN: 2045-2322. DOI: `10.1038/srep29638`.

[156] Eric D. Black. “An introduction to Pound–Drever–Hall laser frequency stabilization”. In: *American Journal of Physics* 69 (1 Jan. 2001), pp. 79–87. ISSN: 0002-9505. DOI: `10.1119/1.1286663`.

[157] Silvia Knappe-Grueneberg et al. “Influence of demagnetization coil configuration on residual field in an extremely magnetically shielded room: Model and measurements”. In: *Journal of Applied Physics* 103 (7 Apr. 2008), 07E925. ISSN: 0021-8979. DOI: `10.1063/1.2837876`.

[158] Niall Holmes et al. “Naturalistic hyperscanning with wearable magnetoencephalography”. In: *Sensors* 23 (12 June 2023), p. 5454. ISSN: 1424-8220. DOI: `10.3390/s23125454`.

[159] L. M. Rushton et al. “Unshielded portable optically pumped magnetometer for the remote detection of conductive objects using eddy current measurements”. In: *Review of Scientific Instruments* 93 (12 Dec. 2022), p. 125103. ISSN: 0034-6748. DOI: `10.1063/5.0102402`.

[160] Daryl W. Preston. “Doppler-free saturated absorption: Laser spectroscopy”. In: *American Journal of Physics* (11 Nov. 1996), pp. 1432–1436. ISSN: 0002-9505. DOI: `10.1119/1.18457`.

[161] Hanna Krauter. “Generation and Application of Entanglement of Room Temperature Ensembles of Atoms”. PhD thesis. Center for Quantum Optics (QUANTOP), Niels Bohr Institute, University of Copenhagen, Feb. 2011.

[162] Irina Novikova, Andrey B. Matsko, and George R. Welch. “Influence of a buffer gas on nonlinear magneto-optical polarization rotation”. In: *Journal of the Optical Society of America B* 22 (1 Jan. 2005), p. 44. ISSN: 0740-3224. DOI: `10.1364/JOSAB.22.000044`.

[163] *GEM GSMP Potassium Magnetometer for High Precision and Accuracy-GEM Systems.* URL: `https://www.gemsys.ca/ultra-high-sensitivity-potassium`.

[164] M. T. Graf et al. “Relaxation of atomic polarization in paraffin-coated cesium vapor cells”. In: *Physical Review A* 72 (2 Aug. 2005), p. 023401. ISSN: 1050-2947. DOI: `10.1103/PhysRevA.72.023401`.

[165] M. V. Balabas et al. “Polarized alkali-metal vapor with minute-long transverse spin-relaxation time”. In: *Physical Review Letters* 105 (7 Aug. 2010), p. 070801. ISSN: 0031-9007. DOI: `10.1103/PhysRevLett.105.070801`.

[166] S. J. Seltzer et al. “Investigation of antirelaxation coatings for alkali-metal vapor cells using surface science techniques”. In: *The Journal of Chemical Physics* 133 (14 Oct. 2010), p. 144703. ISSN: 0021-9606. DOI: `10.1063/1.3489922`.

[167] N. Castagna et al. “A large sample study of spin relaxation and magnetometric sensitivity of paraffin-coated Cs vapor cells”. In: *Applied Physics B* 96 (4 Sept. 2009), pp. 763–772. ISSN: 0946-2171. DOI: `10.1007/s00340-009-3464-5`.

[168] Dmitry Budker, Donald J. Orlando, and Valeriy Yashchuk. “Nonlinear laser spectroscopy and magneto-optics”. In: *American Journal of Physics* 67 (7 July 1999), pp. 584–592. ISSN: 0002-9505. DOI: `10.1119/1.19328`.

[169] S. Groeger et al. "A sound card based multi-channel frequency measurement system". In: *The European Physical Journal Applied Physics* 33 (3 Mar. 2006), pp. 221–224. ISSN: 1286-0042. DOI: `10.1051/epjap:2006020`.

[170] G. Bison et al. "Sensitive and stable vector magnetometer for operation in zero and finite fields". In: *Optics Express* 26 (13 June 2018), p. 17350. ISSN: 1094-4087. DOI: `10.1364/OE.26.017350`.

[171] Philip J. Broser et al. "Optically pumped magnetometers for magneto-myography to study the innervation of the hand". In: *IEEE Transactions on Neural Systems and Rehabilitation Engineering* 26 (11 Nov. 2018), pp. 2226–2230. ISSN: 1534-4320. DOI: `10.1109/TNSRE.2018.2871947`.

[172] H. Xia et al. "Magnetoencephalography with an atomic magnetometer". In: *Applied Physics Letters* 89 (21 Nov. 2006), p. 211104. ISSN: 0003-6951. DOI: `10.1063/1.2392722`.

[173] Aikaterini Gialopsou et al. "Improved spatio-temporal measurements of visually evoked fields using optically-pumped magnetometers". In: *Scientific Reports* 11 (1 Nov. 2021), p. 22412. ISSN: 2045-2322. DOI: `10.1038/s41598-021-01854-7`.

[174] Elena Boto et al. "Moving magnetoencephalography towards real-world applications with a wearable system". In: *Nature* 555 (7698 Mar. 2018), pp. 657–661. ISSN: 0028-0836. DOI: `10.1038/nature26147`.

[175] M. E. Limes et al. "Portable magnetometry for detection of biomagnetism in ambient environments". In: *Physical Review Applied* 14 (1 July 2020), p. 011002. ISSN: 2331-7019. DOI: `10.1103/PhysRevApplied.14.011002`.

[176] Amir Borna et al. "Non-invasive functional-brain-imaging with an OPM-based magnetoencephalography system". In: *PLOS ONE* 15 (1 Jan. 2020). Ed. by Christos Papadelis, e0227684. ISSN: 1932-6203. DOI: `10.1371/journal.pone.0227684`.

[177] I. A. Sulai et al. "Characterizing atomic magnetic gradiometers for fetal magnetocardiography". In: *Review of Scientific Instruments* 90 (8 Aug. 2019), p. 085003. ISSN: 0034-6748. DOI: `10.1063/1.5091007`.

[178] G. Lembke et al. "Optical multichannel room temperature magnetic field imaging system for clinical application". In: *Biomedical Optics Express* 5 (3 Mar. 2014), p. 876. ISSN: 2156-7085. DOI: `10.1364/BOE.5.000876`.

[179] Cort Johnson et al. "Magnetic relaxometry with an atomic magnetometer and SQUID sensors on targeted cancer cells". In: *Journal of Magnetism and Magnetic Materials* 324 (17 Aug. 2012), pp. 2613–2619. ISSN: 03048853. DOI: `10.1016/j.jmmm.2012.03.015`.

[180] Lykourgos Bougas et al. "Nondestructive in-line sub-picomolar detection of magnetic nanoparticles in flowing complex fluids". In: *Scientific Reports* 8 (1 Feb. 2018), p. 3491. ISSN: 2045-2322. DOI: `10.1038/s41598-018-21802-2`.

[181] Xin Bi et al. "Quantitative analysis of magnetic cobalt particles with an optically pumped atomic magnetometer". In: *Applied Physics Letters* 118 (8 Feb. 2021), p. 084101. ISSN: 0003-6951. DOI: `10.1063/5.0039565`.

[182] Aaron Jaufenthaler et al. "Pulsed optically pumped magnetometers: Addressing dead time and bandwidth for the unshielded magnetorelaxometry of magnetic nanoparticles". In: *Sensors* 21 (4 Feb. 2021), p. 1212. ISSN: 1424-8220. DOI: `10.3390/s21041212`.

[183] Eric Corsini et al. “Search for plant biomagnetism with a sensitive atomic magnetometer”. In: *Journal of Applied Physics* 109 (7 Apr. 2011), p. 074701. ISSN: 0021-8979. DOI: `10.1063/1.3560920`.

[184] Anne Fabricant et al. “Action potentials induce biomagnetic fields in carnivorous Venus flytrap plants”. In: *Scientific Reports* 11 (1 Jan. 2021), p. 1438. ISSN: 2045-2322. DOI: `10.1038/s41598-021-81114-w`.

[185] Jens U. Sutter et al. “Recording the heart beat of cattle using a gradiometer system of optically pumped magnetometers”. In: *Computers and Electronics in Agriculture* 177 (Oct. 2020), p. 105651. ISSN: 01681699. DOI: `10.1016/j.compag.2020.105651`.

[186] John W. Blanchard, Dmitry Budker, and Andreas Trabesinger. “Lower than low: Perspectives on zero- to ultralow-field nuclear magnetic resonance”. In: *Journal of Magnetic Resonance* 323 (Feb. 2021), p. 106886. ISSN: 10907807. DOI: `10.1016/j.jmr.2020.106886`.

[187] Danila A. Barskiy et al. “Zero-field nuclear magnetic resonance of chemically exchanging systems”. In: *Nature Communications* 10 (1 July 2019), p. 3002. ISSN: 2041-1723. DOI: `10.1038/s41467-019-10787-9`. URL: `https://www.nature.com/articles/s41467-019-10787-9`.

[188] Piotr Put et al. “Zero- to ultralow-field NMR spectroscopy of small biomolecules”. In: *Analytical Chemistry* 93 (6 Feb. 2021), pp. 3226–3232. ISSN: 0003-2700. DOI: `10.1021/acs.analchem.0c04738`.

[189] I. M. Savukov and M. V. Romalis. “NMR detection with an atomic magnetometer”. In: *Physical Review Letters* 94 (12 Mar. 2005), p. 123001. ISSN: 0031-9007. DOI: `10.1103/PhysRevLett.94.123001`.

[190] Shoujun Xu et al. “Magnetic resonance imaging with an optical atomic magnetometer”. In: *Proceedings of the National Academy of Sciences* 103 (34 Aug. 2006), pp. 12668–12671. ISSN: 0027-8424. DOI: `10.1073/pnas.0605396103`.

[191] Min Jiang et al. “Magnetic gradiometer for the detection of zero- to ultralow-field nuclear magnetic resonance”. In: *Physical Review Applied* 11 (2 Feb. 2019), p. 024005. ISSN: 2331-7019. DOI: `10.1103/PhysRevApplied.11.024005`.

[192] S. Begus et al. “Optical detection of low frequency NQR signals: A step forward from conventional NQR”. In: *Journal of Physics D: Applied Physics* 50 (9 Mar. 2017), p. 095601. ISSN: 0022-3727. DOI: `10.1088/1361-6463/aa4f23`.

[193] Giuseppe Bevilacqua et al. “Sub-millimetric ultra-low-field MRI detected *in situ* by a dressed atomic magnetometer”. In: *Applied Physics Letters* 115 (17 Oct. 2019), p. 174102. ISSN: 0003-6951. DOI: `10.1063/1.5123653`.

[194] Rui Zhang et al. “Stand-off magnetometry with directional emission from sodium vapors”. In: *Physical Review Letters* 127 (17 Oct. 2021), p. 173605. ISSN: 0031-9007. DOI: `10.1103/PhysRevLett.127.173605`.

[195] James S. Bennett et al. “Precision magnetometers for aerospace applications: A review”. In: *Sensors* 21 (16 Aug. 2021), p. 5568. ISSN: 1424-8220. DOI: `10.3390/s21165568`.

[196] Felipe Pedreros Bustos et al. “Polarization-driven spin precession of mesospheric sodium atoms”. In: *Optics Letters* 43 (23 Dec. 2018), p. 5825. ISSN: 0146-9592. DOI: `10.1364/OL.43.005825`.

[197] Luca Marmugi and Ferruccio Renzoni. "Electromagnetic induction imaging with atomic magnetometers: progress and perspectives". In: *Applied Sciences* 10 (18 Sept. 2020), p. 6370. ISSN: 2076-3417. DOI: 10.3390/app10186370.

[198] Kasper Jensen et al. "Detection of low-conductivity objects using eddy current measurements with an optical magnetometer". In: *Physical Review Research* 1 (3 Nov. 2019), p. 033087. ISSN: 2643-1564. DOI: 10.1103/PhysRevResearch.1.033087.

[199] Giuseppe Bevilacqua et al. "Electromagnetic induction imaging: Signal detection based on tuned-dressed optical magnetometry". In: *Optics Express* 29 (23 Nov. 2021), p. 37081. ISSN: 1094-4087. DOI: 10.1364/OE.437930.

[200] Benjamin Maddox, Yuval Cohen, and Ferruccio Renzoni. "Through-skin pilot-hole detection and localization with a mechanically translatable atomic magnetometer". In: *Applied Physics Letters* 120 (1 Jan. 2022), p. 014002. ISSN: 0003-6951. DOI: 10.1063/5.0081274.

[201] S. Afach et al. "Characterization of the global network of optical magnetometers to search for exotic physics (GNOME)". In: *Physics of the Dark Universe* 22 (Dec. 2018), pp. 162–180. ISSN: 22126864. DOI: 10.1016/j.dark.2018.10.002.

[202] Derek F. Jackson Kimball et al. "Constraints on long-range spin-gravity and monopole-dipole couplings of the proton". In: *Physical Review D* 96 (7 Oct. 2017), p. 075004. ISSN: 2470-0010. DOI: 10.1103/PhysRevD.96.075004.

[203] Wolfgang Klassen. "All-Optical Cs Magnetometry System for a Neutron Electric Dipole Moment Experiment". Mar. 2020. URL: https://mspace.lib.umanitoba.ca/handle/1993/34596.

[204] Samer Afach et al. "Search for topological defect dark matter with a global network of optical magnetometers". In: *Nature Physics* 17 (12 Dec. 2021), pp. 1396–1401. ISSN: 1745-2473. DOI: 10.1038/s41567-021-01393-y.

[205] A. Kuzmich et al. "Quantum nondemolition measurements of collective atomic spin". In: *Physical Review A* 60 (3 Sept. 1999), pp. 2346–2350. ISSN: 1050-2947. DOI: 10.1103/PhysRevA.60.2346.

[206] Paul Siddons et al. "A gigahertz-bandwidth atomic probe based on the slow-light Faraday effect". In: *Nature Photonics* 3 (4 Apr. 2009), pp. 225–229. ISSN: 1749-4885. DOI: 10.1038/nphoton.2009.27.

[207] Ming-Feng Wang, Nian-Quan Jiang, and Yi-Zhuang Zheng. "Optical continuous-variable quadratic phase gate via Faraday interaction". In: *Optics Express* 22 (8 Apr. 2014), p. 9182. ISSN: 1094-4087. DOI: 10.1364/OE.22.009182.

[208] Anne Fabricant. "Quantum-Limited Optical Magnetometry with Cesium Microcells". Center for Quantop Optics (QUANTOP), Niels Bohr Institute, University of Copenhagen, Aug. 2014.

[209] F. Baudenbacher et al. "Intracellular axial current in *Chara corallina* reflects the altered kinetics of ions in cytoplasm under the influence of light". In: *Biophysical Journal* 88 (1 Jan. 2005), pp. 690–697. ISSN: 00063495. DOI: 10.1529/biophysj.104.044974.

[210] Pragya Sharma, Nidhi Sharma, and Renu Deswal. "The molecular biology of the low-temperature response in plants". In: *BioEssays* 27 (10 Oct. 2005), pp. 1048–1059. ISSN: 0265-9247. DOI: 10.1002/bies.20307.

[211] Michael Evans. “Touch sensitivity in plants: Be aware or beware”. In: *Trends in Plant Science* 8 (7 July 2003), pp. 312–314. ISSN: 13601385. DOI: 10.1016/S1360-1385(03)00133-X.

[212] Rainer Hedrich and Erwin Neher. “Venus flytrap: How an excitable, carnivorous plant Works”. In: *Trends in Plant Science* 23 (3 Mar. 2018), pp. 220–234. ISSN: 13601385. DOI: 10.1016/j.tplants.2017.12.004.

[213] V. Jazbinsek et al. “Magnetic detection of injury-induced ionic currents in bean plants”. In: *European Biophysics Journal* 29 (7 Dec. 2000), pp. 515–522. ISSN: 0175-7571. DOI: 10.1007/s002490000105.

[214] Alexander G. Volkov. “Green plants: Electrochemical interfaces”. In: *Journal of Electroanalytical Chemistry* 483 (1-2 Mar. 2000), pp. 150–156. ISSN: 15726657. DOI: 10.1016/S0022-0728(99)00497-0.

[215] Sylvain Baillet. “Magnetoencephalography for brain electrophysiology and imaging”. In: *Nature Neuroscience* 20 (3 Mar. 2017), pp. 327–339. ISSN: 1097-6256. DOI: 10.1038/nn.4504.

[216] Charles P. Slichter. *Principles of Magnetic Resonance*. Vol. 1. Springer Berlin Heidelberg, 1990. ISBN: 978-3-642-08069-2. DOI: 10.1007/978-3-662-09441-9.

[217] Gary H. Glover. “Overview of functional magnetic resonance imaging”. In: *Neurosurgery Clinics of North America* 22 (2 Apr. 2011), pp. 133–139. ISSN: 10423680. DOI: 10.1016/j.nec.2010.11.001.

[218] Donald L. Schomer and Fernando H. Lopes da Silva, eds. *Niedermeyer’s Electroencephalography*. Vol. 1. Oxford University Press, Nov. 2017. ISBN: 9780190228484. DOI: 10.1093/med/9780190228484.001.0001.

[219] D. Cohen. “DC magnetic fields from the human body generally: A historical overview.” In: *Neurology & clinical neurophysiology: NCN* 2004 (Nov. 2004), p. 93. ISSN: 1526-8748. URL: http://www.ncbi.nlm.nih.gov/pubmed/16012676.

[220] Samuel J. Williamson et al., eds. *Biomagnetism*. Springer US, 1983. ISBN: 9781475717877. DOI: 10.1007/978-1-4757-1785-3.

[221] John F. Barry et al. “Optical magnetic detection of single-neuron action potentials using quantum defects in diamond”. In: *Proceedings of the National Academy of Sciences* 113 (49 Dec. 2016), pp. 14133–14138. ISSN: 0027-8424. DOI: 10.1073/pnas.1601513113.

[222] Z. Trontelj et al. “Magnetic detection of a single action potential in Chara corallina internodal cells”. In: *Biophysical Journal* 66 (5 May 1994), pp. 1694–1696. ISSN: 00063495. DOI: 10.1016/S0006-3495(94)80960-9.

[223] Alexander G. Volkov. *Plant Electrophysiology*. Ed. by Alexander G. Volkov. Springer Berlin Heidelberg, 2006, pp. 1–508. ISBN: 978-3-540-32717-2. DOI: 10.1007/978-3-540-37843-3.

[224] Alexander G. Volkov. “Signaling in electrical networks of the Venus flytrap (*Dionaea muscipula* Ellis)”. In: *Bioelectrochemistry* 125 (Feb. 2019), pp. 25–32. ISSN: 15675394. DOI: 10.1016/j.bioelechem.2018.09.001.

[225] Anda L. Iosip et al. “The Venus flytrap trigger hair–specific potassium channel KDM1 can reestablish the K$^+$ gradient required for hapto-electric signaling”. In: *PLOS Biology* 18 (12 Dec. 2020). Ed. by Mark Estelle, e3000964. ISSN: 1545-7885. DOI: 10.1371/journal.pbio.3000964.

[226] Yoël Forterre et al. "How the Venus flytrap snaps". In: *Nature* 433 (7024 Jan. 2005), pp. 421–425. ISSN: 0028-0836. DOI: 10.1038/nature03185.

[227] Renate Sachse et al. "Snapping mechanics of the Venus flytrap (*Dionaea muscipula*)". In: *Proceedings of the National Academy of Sciences* 117 (27 July 2020), pp. 16035–16042. ISSN: 0027-8424. DOI: 10.1073/pnas.2002707117. URL: https://pnas.org/doi/full/10.1073/pnas.2002707117.

[228] Hiraku Suda et al. "Calcium dynamics during trap closure visualized in transgenic Venus flytrap". In: *Nature Plants* 6 (10 Oct. 2020), pp. 1219–1224. ISSN: 2055-0278. DOI: 10.1038/s41477-020-00773-1.

[229] Sönke Scherzer et al. "Insect haptoelectrical stimulation of Venus flytrap triggers exocytosis in gland cells". In: *Proceedings of the National Academy of Sciences* 114 (18 May 2017), pp. 4822–4827. ISSN: 0027-8424. DOI: 10.1073/pnas.1701860114.

[230] Jennifer Böhm et al. "The Venus flytrap *Dionaea muscipula* counts prey-induced action potentials to induce sodium uptake". In: *Current Biology* 26 (3 Feb. 2016), pp. 286–295. ISSN: 09609822. DOI: 10.1016/j.cub.2015.11.057.

[231] William M. Palmer et al. "PEA-CLARITY: 3D molecular imaging of whole plant organs". In: *Scientific Reports* 5 (1 Sept. 2015), p. 13492. ISSN: 2045-2322. DOI: 10.1038/srep13492.

[232] J. Böhm et al. "Venus flytrap HKT1-type channel provides for prey sodium uptake into carnivorous plant without conflicting with electrical excitability". In: *Molecular Plant* 9 (3 Mar. 2016), pp. 428–436. ISSN: 16742052. DOI: 10.1016/j.molp.2015.09.017.

[233] F. Thiel et al. "Demagnetization of magnetically shielded rooms". In: *Review of Scientific Instruments* 78 (3 Mar. 2007), p. 35106. ISSN: 0034-6748. DOI: 10.1063/1.2713433.

[234] S. Scherzer et al. "Venus flytrap trigger hairs are micronewton mechano-sensors that can detect small insect prey". In: *Nature Plants* 5 (7 July 2019), pp. 670–675. ISSN: 2055-0278. DOI: 10.1038/s41477-019-0465-1.

[235] Chi Tam Nguyen et al. "Identification of cell populations necessary for leaf-to-leaf electrical signaling in a wounded plant". In: *Proceedings of the National Academy of Sciences* 115 (40 Oct. 2018), pp. 10178–10183. ISSN: 0027-8424. DOI: 10.1073/pnas.1807049115.

[236] T. Sibaoka. "Action potentials in plant organs". In: *Symp. Soc. Exp. Biol.* 20 (1966), pp. 49–74.

[237] Alexander G. Volkov et al. "Memristors in the Venus flytrap". In: *Plant Signaling & Behavior* 9 (8 Aug. 2014), e29204. ISSN: 1559-2324. DOI: 10.4161/psb.29204.

[238] R. L. Fagaly. "Superconducting quantum interference device instruments and applications". In: *Review of Scientific Instruments* 77 (10 Oct. 2006), p. 101101. ISSN: 0034-6748. DOI: 10.1063/1.2354545.

[239] A. Schnabel et al. "A sensor configuration for a 304 SQUID vector magnetometer". In: *Neurology & clinical neurophysiology: NCN* 2004 (Nov. 2004), p. 70. ISSN: 1526-8748. URL: http://www.ncbi.nlm.nih.gov/pubmed/16012698.

[240] Li-Anne Liew et al. "Microfabricated alkali atom vapor cells". In: *Applied Physics Letters* 84 (14 Apr. 2004), pp. 2694–2696. ISSN: 0003-6951. DOI: 10.1063/1.1691490.

[241] H. Schnyder and U. Baum. “Growth of the grain of wheat (*Triticum aestivum* L.). The relationship between water content and dry matter accumulation”. In: *European Journal of Agronomy* 1 (2 Jan. 1992), pp. 51–57. ISSN: 1161-0301. DOI: `10.1016/S1161-0301(14)80001-4`.

[242] Rodrigo G. Sala, Mark E. Westgate, and Fernando H. Andrade. “Source/sink ratio and the relationship between maximum water content, maximum volume, and final dry weight of maize kernels”. In: *Field Crops Research* 101 (1 Feb. 2007), pp. 19–25. ISSN: 0378-4290. DOI: `10.1016/j.fcr.2006.09.004`.

[243] S. Saura-Mas and F. Lloret. “Leaf and shoot water content and leaf dry matter content of Mediterranean woody species with different post-fire regenerative Strategies”. In: *Annals of Botany* 99 (3 Jan. 2007), pp. 545–554. ISSN: 0305-7364. DOI: `10.1093/aob/mcl284`.

[244] Weiwei Huang et al. “Increase in absolute leaf water content tends to keep pace with that of leaf dry mass-Evidence from bamboo plants”. In: *Symmetry* 12 (8 Aug. 2020), p. 1345. ISSN: 2073-8994. DOI: `10.3390/sym12081345`.

[245] C. D. Araujo et al. “Proton magnetic resonance techniques for characterization of water in wood: Application to white spruce”. In: *Wood Science and Technology* 26 (2 Jan. 1992), pp. 101–113. ISSN: 0043-7719. DOI: `10.1007/BF00194466`.

[246] P. Krishnan et al. “Changes in seed water status as characterized by NMR in developing soybean seed grown under moisture stress conditions”. In: *Biochemical and Biophysical Research Communications* 444 (4 Feb. 2014), pp. 485–490. ISSN: 0006-291X. DOI: `10.1016/j.bbrc.2014.01.091`.

[247] Kubra Unal et al. “Time domain (TD)-NMR relaxometry as a tool to investigate the cell integrity of tomato seeds exposed to osmotic stress (OS), ultrasonication (US) and high hydrostatic pressure (HHP)”. In: *Journal of Food Science and Technology* 57 (10 Oct. 2020), pp. 3739–3747. ISSN: 0022-1155. DOI: `10.1007/s13197-020-04406-5`. URL: `https://link.springer.com/10.1007/s13197-020-04406-5`.

[248] Fabian Jaeger, Elisabeth Grohmann, and Gabriele E. Schaumann. “1H NMR relaxometry in natural humous soil samples: Insights in microbial effects on relaxation time distributions”. In: *Plant and Soil* 280 (1-2 Feb. 2006), pp. 209–222. ISSN: 0032-079X. DOI: `10.1007/s11104-005-3035-4`.

[249] Maja Musse, Mireille Cambert, and François Mariette. “NMR study of water distribution inside tomato cells: Effects of water stress”. In: *Applied Magnetic Resonance* 38 (4 Aug. 2010), pp. 455–469. ISSN: 0937-9347. DOI: `10.1007/s00723-010-0139-7`.

[250] Md Imran H. Khan et al. “Investigation of bound and free water in plant-based food material using NMR T2 relaxometry”. In: *Innovative Food Science & Emerging Technologies* 38 (Dec. 2016), pp. 252–261. ISSN: 1466-8564. DOI: `10.1016/j.ifset.2016.10.015`.

[251] Elif Gokcen Ates et al. “Field-dependent NMR relaxometry for food science: Applications and perspectives”. In: *Trends in Food Science & Technology* 110 (Apr. 2021), pp. 513–524. ISSN: 0924-2244. DOI: `10.1016/j.tifs.2021.02.026`.

[252] Henk Van As and John van Duynhoven. “MRI of plants and foods”. In: *Journal of Magnetic Resonance* 229 (Apr. 2013), pp. 25–34. ISSN: 1090-7807. DOI: `10.1016/j.jmr.2012.12.019`.

[253] Maja Musse et al. “Structural changes in senescing oilseed rape leaves at tissue and subcellular levels monitored by nuclear magnetic resonance relaxometry through water status”. In: *Plant Physiology* 163 (1 Sept. 2013), pp. 392–406. ISSN: 0032-0889. DOI: 10.1104/pp.113.223123.

[254] Maja Musse et al. “A mobile NMR lab for leaf phenotyping in the field”. In: *Plant Methods* 13 (1 Dec. 2017), p. 53. ISSN: 1746-4811. DOI: 10.1186/s13007-017-0203-5.

[255] Clément Sorin et al. “Leaf development monitoring and early detection of water deficiency by low field nuclear magnetic resonance relaxation in *Nicotiana tabacum* Plants”. In: *Applied Sciences* 8 (6 June 2018), p. 943. ISSN: 2076-3417. DOI: 10.3390/app8060943.

[256] D. C. McCain. “Nuclear magnetic resonance study of spin relaxation and magnetic field gradients in maple leaves”. In: *Biophysical Journal* 69 (3 Sept. 1995), pp. 1111–1116. ISSN: 0006-3495. DOI: 10.1016/S0006-3495(95)79985-4.

[257] Anne E. Berns et al. “Applicability of solid state fast field cycling NMR relaxometry in understanding relaxation properties of leaves and leaf-litters”. In: *Organic Geochemistry* 42 (8 Sept. 2011), pp. 978–984. ISSN: 0146-6380. DOI: 10.1016/j.orggeochem.2011.04.006.

[258] Donatella Capitani et al. “In situ investigation of leaf water status by portable unilateral nuclear magnetic resonance”. In: *Plant Physiology* 149 (4 Apr. 2009), pp. 1638–1647. ISSN: 1532-2548. DOI: 10.1104/pp.108.128884.

[259] Carel W. Windt et al. “A mobile NMR sensor and relaxometric method to non-destructively monitor water and dry matter content in plants”. In: *Frontiers in Plant Science* 12 (Feb. 2021), p. 18. ISSN: 1664-462X. DOI: 10.3389/fpls.2021.617768.

[260] Piyush Jain et al. “A minimally disruptive method for measuring water potential in planta using hydrogel nanoreporters”. In: *Proceedings of the National Academy of Sciences* 118 (23 June 2021). ISSN: 0027-8424. DOI: 10.1073/pnas.2008276118.

[261] Akiyoshi Nagata, Katsumi Kose, and Yasuhiko Terada. “Development of an outdoor MRI system for measuring flow in a living tree”. In: *Journal of Magnetic Resonance* 265 (Apr. 2016), pp. 129–138. ISSN: 1090-7807. DOI: 10.1016/j.jmr.2016.02.004.

[262] Michael W. Malone et al. “In vivo observation of tree drought response with low-field NMR and Neutron Imaging”. In: *Frontiers in Plant Science* 7 (MAY2016 May 2016), p. 184674. ISSN: 1664-462X. DOI: 10.3389/fpls.2016.00564.

[263] I.M. Savukov, S.J. Seltzer, and M.V. Romalis. “Detection of NMR signals with a radio-frequency atomic magnetometer”. In: *Journal of Magnetic Resonance* 185 (2 Apr. 2007), pp. 214–220. ISSN: 1090-7807. DOI: 10.1016/j.jmr.2006.12.012.

[264] Michael C. D. Tayler, Jordan Ward-Williams, and Lynn F. Gladden. “NMR relaxation in porous materials at zero and ultralow magnetic fields”. In: *Journal of Magnetic Resonance* 297 (Dec. 2018), pp. 1–8. ISSN: 1090-7807. DOI: 10.1016/j.jmr.2018.09.014.

[265] S. Hartwig et al. “A superconducting quantum interference device measurement system for ultra low-field nuclear magnetic resonance”. In: *Applied Magnetic Resonance* 44 (1-2 Feb. 2013), pp. 9–22. ISSN: 0937-9347. DOI: 10.1007/s00723-012-0387-9.

[266] John W. Blanchard and Dmitry Budker. “Zero- to Ultralow-Field NMR”. In: *eMagRes* 5 (3 Sept. 2016), pp. 1395–1410. ISSN: 20556101. DOI: 10.1002/9780470034590.emrstm1369.

[267] Michelle Espy, Andrei Matlashov, and Petr Volegov. “SQUID-detected ultra-low field MRI”. In: *Journal of Magnetic Resonance* 229 (Apr. 2013), pp. 127–141. ISSN: 1090-7807. DOI: 10.1016/j.jmr.2013.02.009.

[268] Anne M. Fabricant et al. "Quadrature-detected zero- to ultralow-field nuclear magnetic resonance". In: *[in preparation]* (2024).

[269] Malcolm H. Levitt. "The signs of frequencies and phases in NMR". In: *Journal of Magnetic Resonance* 126 (2 June 1997), pp. 164–182. ISSN: 1090-7807. DOI: `10.1006/jmre.1997.1161`.

[270] James Keeler. *Understanding NMR Spectroscopy*. 2nd ed. John Wiley & Sons, Ltd, 2010. ISBN: 9780470746080.

[271] C. F. Brewer and L. Bhattacharyya. "Specificity of concanavalin A binding to asparagine-linked glycopeptides. A nuclear magnetic relaxation dispersion study." In: *Journal of Biological Chemistry* 261 (16 June 1986), pp. 7306–7310. ISSN: 0021-9258. DOI: `10.1016/S0021-9258(17)38391-6`.

[272] Eberhard Rommel et al. "Proton spin relaxation dispersion studies of phospholipid membranes". In: *The Journal of Physical Chemistry* 92 (10 May 1988), pp. 2981–2987. ISSN: 0022-3654. DOI: `10.1021/j100321a053`.

[273] Bertil Halle and Vladimir P. Denisov. "Magnetic relaxation dispersion studies of biomolecular solutions". In: *Methods in Enzymology* 338 (Jan. 2002), pp. 178–201. ISSN: 0076-6879. DOI: `10.1016/S0076-6879(02)38220-X`.

[274] Anne Fabricant, Irina Novikova, and Georg Bison. "How to build a magnetometer with thermal atomic vapor: A tutorial". In: *New Journal of Physics* 25 (2 Feb. 2023), p. 025001. ISSN: 1367-2630. DOI: `10.1088/1367-2630/acb840`.

[275] Seyma Alcicek et al. "Zero- to low-field relaxometry of chemical and biological fluids". In: *Communications Chemistry* 6 (1 Aug. 2023), p. 165. ISSN: 2399-3669. DOI: `10.1038/s42004-023-00965-8`.

[276] A. Abragam. *Principles of Nuclear Magnetism (The International Series of Monographs on Physics)*. Clarendon Press, 1983. ISBN: 9780198520146. URL: `https://global.oup.com/academic/product/the-principles-of-nuclear-magnetism-9780198520146`.

[277] Danila A. Barskiy and Andrey Pravdivtsev. "Magnetization and Polarization of Coupled Nuclear Spin Ensembles". In: *arXiv* (Aug. 2023). DOI: `10.48550/arXiv.2308.15837`. URL: `http://arxiv.org/abs/2308.15837`.

[278] Isaac Vega-Muñoz et al. "Breaking Bad News: Dynamic molecular mechanisms of wound response in plants". In: *Frontiers in Plant Science* 11 (Dec. 2020), p. 610445. ISSN: 1664-462X. DOI: `10.3389/fpls.2020.610445`. URL: `https://www.frontiersin.org/articles/10.3389/fpls.2020.610445/full`.

[279] Matthew Adam Thomas and Robin Lewis Cooper. "Building bridges: mycelium–mediated plant–plant electrophysiological communication". In: *Plant Signaling & Behavior* 17 (1 Dec. 2022). ISSN: 1559-2324. DOI: `10.1080/15592324.2022.2129291`. URL: `https://www.tandfonline.com/doi/full/10.1080/15592324.2022.2129291`.

[280] N. A. R. Gow and B. M. Morris. "The electric fungus". In: *Botanical Journal of Scotland* 47 (2 Jan. 1995), pp. 263–277. ISSN: 1359-4869. DOI: `10.1080/03746609508684833`. URL: `http://www.tandfonline.com/doi/full/10.1080/03746609508684833`.

[281] S. Olsson and B. S. Hansson. "Action potential-like activity found in fungal mycelia is sensitive to stimulation". In: *Naturwissenschaften* 82 (1 Jan. 1995), pp. 30–31. ISSN: 0028-1042. DOI: `10.1007/BF01167867`. URL: `http://link.springer.com/10.1007/BF01167867`.

[282] Suzanne W. Simard et al. “Net transfer of carbon between ectomycorrhizal tree species in the field”. In: *Nature* 388 (6642 Aug. 1997), pp. 579–582. ISSN: 0028-0836. DOI: 10.1038/41557. URL: https://www.nature.com/articles/41557.

[283] Peter Wohlleben. *Das geheime Leben der Bäume (The Hidden Life of Trees): Was sie fühlen, wie sie kommunizieren - die Entdeckung einer verborgenen Welt.* Ludwig (Random House), May 2015, p. 223. ISBN: 9783453280670. URL: https://www.penguin.de/buecher/peter-wohlleben-das-geheime-leben-der-baeume/buch/9783453280670.

[284] Merlin Sheldrake. *Entangled Life: How Fungi Make Our Worlds, Change Our Minds and Shape Our Futures.* Vintage (Penguin Random House), Sept. 2021, p. 358. ISBN: 9781784708276. URL: https://www.penguin.co.uk/books/437330/entangled-life-by-merlin-sheldrake/9781784708276.

[285] Anne M. Fabricant et al. “Ultralow-field nuclear magnetic resonance for direct nondestructive observation of electrolyte composition in batteries”. In: *ChemRxiv* (Aug. 2024). DOI: 10.26434/CHEMRXIV-2024-32XJ9. URL: https://chemrxiv.org/engage/chemrxiv/article-details/66b9c537c9c6a5c07afbb4ee.

[286] Kirill V. Kovtunov et al. “Hyperpolarized NMR spectroscopy: *d*-DNP, PHIP, and SABRE techniques”. In: *Chemistry – An Asian Journal* 13 (15 Aug. 2018), pp. 1857–1871. ISSN: 1861-4728. DOI: 10.1002/asia.201800551. URL: https://onlinelibrary.wiley.com/doi/10.1002/asia.201800551.